University of Cagliari

PHD COURSE

ELECTRONIC AND COMPUTER ENGINEERING

CLASS XXVIII (ING-IND/32)

MANAGEMENT STRATEGIES OF ELECTRIC VEHICLES AND CONCENTRATING PHOTOVOLTAIC SYSTEMS FOR MICROGRIDS

Author: **Claudia Musio**

PhD Course Coordinator Prof. Fabio Roli

Advisor Prof. Alfonso Damiano

2014 – 2015

Ph.D. in Electronic and Computer Engineering
Dept. of Electrical and Electronic Engineering
University of Cagliari

Management strategies of electric vehicles and Concentrating Photovoltaic systems for microgrids

Claudia Musio

Advisor: prof. Alfonso Damiano

Curriculum: ING-IND/32 Convertitori, macchine e azionamenti elettrici

CLAUDIA MUSIO gratefully acknowledges Sardinia Regional Government for the financial support of her PhD scholarship (P.O.R. Sardegna F.S.E. Operational Programme of the Autonomous Region of Sardinia, European Social Fund 2007-2013 - Axis IV Human Resources, Objective l.3, Line of Activity l.3.1.)

Abstract

The present PhD dissertation is focused on the development of management strategies of electric vehicles and concentrating photovoltaic systems in microgrids (MGs). Firstly the MG concept and then the state-of-the-art analysis of the most important components (that are photovoltaic and energy storage systems and electric vehicles) are presented. Then, the first part of the thesis is focused on the concentrating photovoltaic (CPV) systems, the most promising new technology for improving the efficiency of PV systems. In particular, two prototypes characterization and the role of CPV systems in MGs are introduced. In fact, the knowledge of the CPV issues highlighted during the characterization process allows the development of a suitable EMS, in order to guarantee the quality, the reliability and the controllability of the MG and consequently of the main electrical power system, especially in presence of a large number of renewable energy sources (RESs). The second part of the dissertation deals with the analysis of two battery electric vehicles (BEVs) models. Nowadays, the exploitation of BEVs has to be placed in a future contest in which the vehicle batteries will perform different tasks in addition to driving purpose, such as the vehicle to grid (V2G) paradigm. Thus, an accurate model that reproduces the battery behavior under real dynamic driving conditions is mandatory, as well as its validation. Moreover, the EV modelling allows to make the EV feedback information reliable for managing correctly and profitably an EV fleet inside a MG. Consequently, in the last part, two management strategies (MSs) are presented. The former operates in a MG composed by office and laboratory loads, a CPV plant and a traditional flat-plate PV one and a BEV fleet. The MS proposed aims to maximize the energy self-consumption by respecting both the driver needs and the MG

requirements. The second MS manages the same MG by employing a stationary storage system instead of a BEV fleet. In this case, the MS purpose is to guarantee a flat-programmable power production profile at the DC node of the MG, even in case of severe weather conditions.

Keywords: Microgrid, Photovoltaic, CPV systems, Energy management system, Battery, Electric vehicles

Contents

Alla mia famiglia, per avermi insegnato la forza, l'onestà e il coraggio.

A Maura, per essermi stata accanto, sei e sarai sempre lo specchio della mia anima.

A Gabriele, per avermi sempre incoraggiata, dato forza e sostegno. Ti amo.

A chi non c'è più. È grazie al vostro sacrificio se oggi arrivo a questo traguardo.

Introduction

The present PhD dissertation is focused on development of new management strategies of electric vehicles and concentrating photovoltaic systems in microgrids (MGs). Chapter 1 deals with a microgrid concept introduction, and then with a state-of-the-art analysis of some of the most important components of a MG, that are photovoltaic and energy storage systems and electric vehicles. Chapter 2 talks about the concentrating photovoltaic (CPV) systems, the most promising new technology for improving the efficiency of PV systems. In particular, the state-of-the-art and the physical parameters of the CPV technology, two prototypes characterization and finally the role of CPV systems in MGs are introduced. In fact, the knowledge of the issues related to the CPV technology highlighted during the characterization process allows the development of a suitable EMS, in order to guarantee the quality, the reliability and the controllability of the MG and consequently of the main electrical power system, especially in presence of a large number of renewable energy sources (RESs). In Chapter 3 two battery electric vehicles (BEVs) models are presented. Nowadays, the environmental and energy policies have recognized at the mobility sector a primary role in the climate policies and have promoted its technological evolution, speeding up the transition from oil mobility to sustainable one, characterized mainly by the introduction of drive-train electrification into vehicle propulsion systems. Moreover, the exploitation of BEVs has to be placed in a future contest in which the vehicle batteries will perform different tasks and services in addition to driving purpose according, for example, to the vehicle to grid (V2G) paradigm. Thus, the EV simulation phase assumes a fundamental role in order to avoid time and cost expenditure during design and realization process and, moreover, to make the EV feedback information reliable for managing correctly and profitably an EV

fleet inside a MG. Consequently, an accurate model that reproduces the battery behavior under real dynamic driving conditions which is characterized by rapid speed variations is mandatory, as well as its validation in order to confirm the estimation results. In Chapter 4 two management strategies (MSs) are presented. The former operates in a MG composed by office and laboratory loads, a CPV plant and a traditional flat-plate PV one and a BEV fleet. The MS proposed aims to maximize the energy self-consumption by respecting both the driver needs and the MG requirements. In particular, a V2G hysteresis control algorithm has been developed in order to reduce the impact of continuous charging current modulation on the electric vehicle battery. The second MS manages the same MG by employing a stationary storage system instead of a BEV fleet. In this case, the MS purpose is to guarantee a flat-programmable power production profile at the DC node of the MG, even in case of severe weather conditions. For this aim, the MS developed is based on a suitable combination of a one-day-ahead scheduling procedure and a real-time control algorithm.

We cannot solve our problems with the same thinking we used when we created them.

Albert Einstein

1

The MicroGrid concept

PResently, the critical world energy situation, i.e. the reduction of avaliable natural resources (oil, gas and carbon mainly), the variable costs of fossil fuels and the requirement to guarantee the stability and security of the electric power system due to the high presence of renewable energy sources (RESs), has led international governments to focus their policies on the development of microgrid (MG) concept. In fact, thanks to MGs that can be considered as smart grid components, a higher exploitation of RESs will be allowed by using new communication and managing techniques [1]. Throught the MG concept varies on the basis of the country, the two most important definitions have been done by the European Technology Platform of Smart Grids and by the U.S. Department of Energy. The former defines a MG as "*a platform that facilitates the integration of distributed generators (DGs), energy storage systems (ESSs) and loads to ensure that the power grid can supply sustainable, price-competitive and reliable electricity*" [1]. Fig. 1.0.1 shows the three main groups of elements which compose a MG, that are for example: DGs composed by RESs (photovoltaic and wind systems and fuel cells) and microturbine, distributed energy

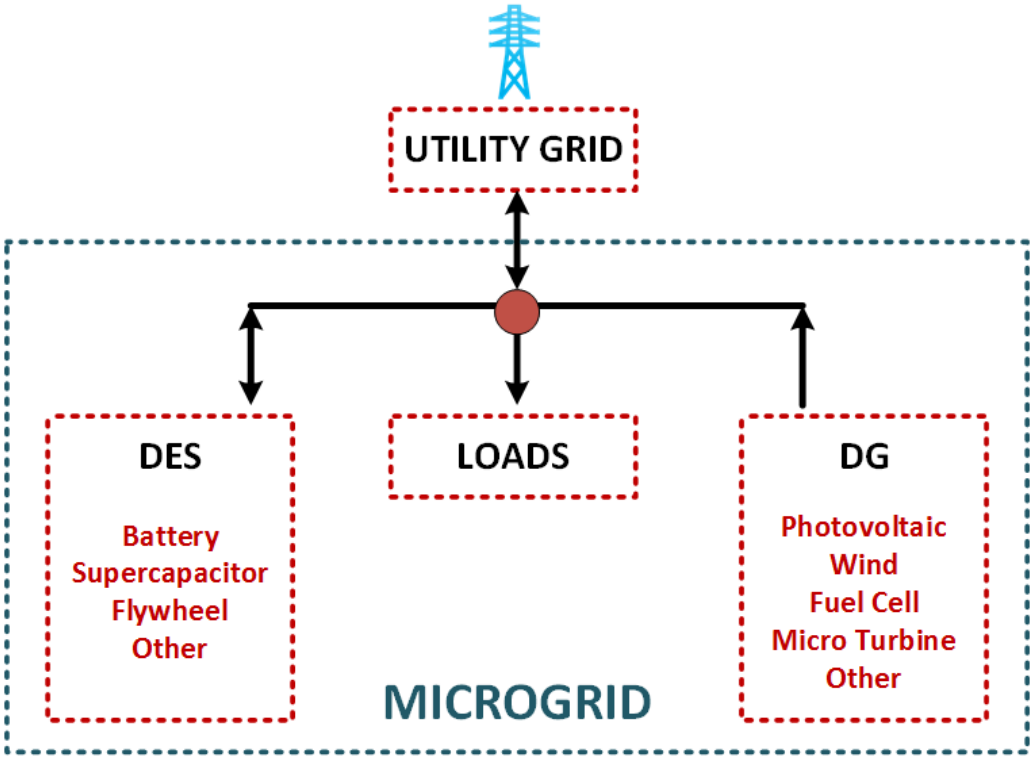

Figure 1.0.1: Typical example of a MG.

storage (DESs), such as battery systems, supercapacitors, flywheels, and loads [1]. The U.S. Department of Energy highlights that a MG is "*a group of interconnected loads and distributed energy sources (DERs) with clearly defined electrical boundaries that acts as a single controllable entity with respect to the grid and can connect and disconnect from the grid to enable it to operate in both grid-connected or island modes*" [2]. Thus, as reported above, on the basis of the american definition, a MG is defined if three conditions have been verified, that are: well defined electrical boundaries, an energy management system and loads, and an installed generation capacity higher than the peak critical load. Thus, if necessary, the MG can operate on islanded mode. In fact, regarding the islanded mode, the MG concept finds application in such areas where the trasmission and distribution system is congested or where there is a limited access to the main grid (research basis for example) [1]. Moreover, the advanges introduced by the MG concept can be analyzed from

different points of view, that are the consumers and the grid ones [3]. Regarding the consumers side, a MG is able principally to provide both thermal and electricity needs and then to guarantee several benefits, such as the reduction of emissions and of the energy cost, a better power quality by means of supporting voltage in case of dips [3]. By considering the grid point of view, a MG is substantially a controlled entity into the main power grid. It is characterized by the possibility to operate both as a single aggregated load or generator and, moreover, to get a renumeration if operates as a source of power or ancillary services in order to support the main grid [3]. In conclusion, a MG can be considered as an aggregation concept, that partecipates both in the supply-side and in the demand-side of the distribution grid [3]. Consequently, a MG is able to introduce benefits in technical, economic, social and environmental points of view and, in addition, can increase the partecipation of end-consumers thanks to the possibility to get a renumeration throughtout the local electricity market, for example. [3], [1]. Regarding the previous concepts, it is worth noting that a MG must be characterized by a management system that allows the optimization of the energy flows inside it. Moreover, as reported in [3], the presence of a control and management system identifies a MG instead of a passive grid penetrated by energy sources. In fact, it is precisely the introduction of an energy management system that allows to overcome the problems connected with a large presence of DGs, in particular photovoltaic and wind plants, and moreover to accomplish an active load management in relation to the grid [1], [3]. Thus, an Energy Management System (EMS) is mandatory to control the different components inside a MG. In particular, as reported in [4], an EMS is made up of a supervisor device that optimize the power flows between the MG components. The optimization can be subdivided into three step [4]. In the first, a forecast of the main MG input variables, such as weather conditions (irradiance), load consumption, power production and state of charge (SOC) of the battery, is defined. Moreover, also the forecast of the energy prices of the main grid is considered. In the second step, the physical constrains of the MG and especially of the ESS are taken into account. Finally, the control device generate the control signals in order to accomplish the optimization process [5],[6]. On the basis of this example, it is worth noting that an appropriate EMS is mandatory for the correct management and planning of a MG, especially in presence of a large

distribution of RESs. In particular, the combination of RESs with ESSs or EVs is fundamental to correctly compensate the strong unpredictability of RESs. Thus, a MG properly controlled improves the exploitation of renewable energy sources and gets all the benefits reported previously. Finally, an EMS is characterized precisely by the capacity to make smart decisions in order to reconciliate the needs of the all subjects involved and maximize the MG profit [3], [1]. Starting by the EMS concept, a management strategy (MS) can be defined as the strategy implemented in the energy management system devoted to different aims, such as the minimization of the power exchange with the main grid (that is the maximizing of self-consumption in case of RESs presence), the maximization of the power exchange with the main grid with the purpose to improve the trading profit if there is a remuneration possibility into the local electricity market, or to guarantee flat-programmable power profiles to the main grid [3].

1.1 MG components analysis

Since now, traditional DGs were connected typically to distribution networks at medium or high voltage levels. Moreover, the grid structure was based on the paradigm that consumers load were passive and the power flows only from distribution substations to customers [1], [3]. The gradual introduction at a low voltage level of microgeneration technologies, such as wind turbines, photovoltaic plants, micro-turbines and fuel cells, have led to a change in the grid philosophy [3]. In fact, microgenerators can exchange their power with the main grid, by transforming completely the grid structure as it has been since now stated. In particular, a more large presence of microgeneration systems, especially RESs characterized by a strong unpredictability, has conducting to consider no longer the low voltage distribution network as a passive attachment of the trasmission network [3]. Moreover, without an appropriate management, microgenerators impact ever more strongly on the power balance and the grid frequency, by reducing the grid stability [3]. Consequently, a suitable control architecture is mandatory to guarantee both the exploitation of microgenerators and the grid reliability. The MG concept fullfills this requirement and, at the same time, introduces the series of benefits reported in the introduction.

As previously defined, a MG can be composed by distributed energy sources, such as battery stationary systems and electric vehicles, loads, renewable energy sources, such as photovoltaic plants, and an energy management system. In the next subsections, the most important components of a MG will be presented by focusing particularlly on those have been taken into account in my PhD research, that are photovoltaic and energy storage systems and electric vehicles.

1.1.1 Photovoltaic Systems: State-of-the-art

As stated in the introduction, the development of the PV technology is fundamental in order to overcome the emission issues related to the employment of conventional energy sources, such as fossil fuels [7]. Contrariwise of them, a PV plant converts directly the solar irradiation in electricity without generating polluting emissions and without other mechanical equipments [8], [7]. Moreover, PV systems are silent and they can be installed by considering a wider variety of solutions, such as in stand-alone or grid-connected mode, or fixed-mounted or supported by a tracker system. The generated current by a typical solar cell depends on the intensity of the irradiation and on the basis of the active area. Regarding the voltage, a common silicon solar cell, whose composed a traditional PV module, generates about 0.5 V. Consequently, solar cells can be connected in series (the output voltage increases) or in parallel (the output current grows) in order to obtain the suitable sizing of the PV system [8], [7]. A group of solar cells makes up a module, and modules connected togheter (in series or in parallel) constitute a PV system, whose output production is related to the connections of the modules. Altought the above advantages, the PV technology has been characterized since now by some important issues, that are in particular the high cost of manifacturing and the high energy pay back time (EPBT). Nevertheless, the improvements in the cell manifacturing and in the overall PV system efficiency have led to a reduction of the modules prices, as reported in Fig 1.1.1. In fact, in relation of the European contest, the price for a PV rooftop system has changed from 5€/W_p in 2006 to 1.3€/W_p in 2015 [9]. Regarding the

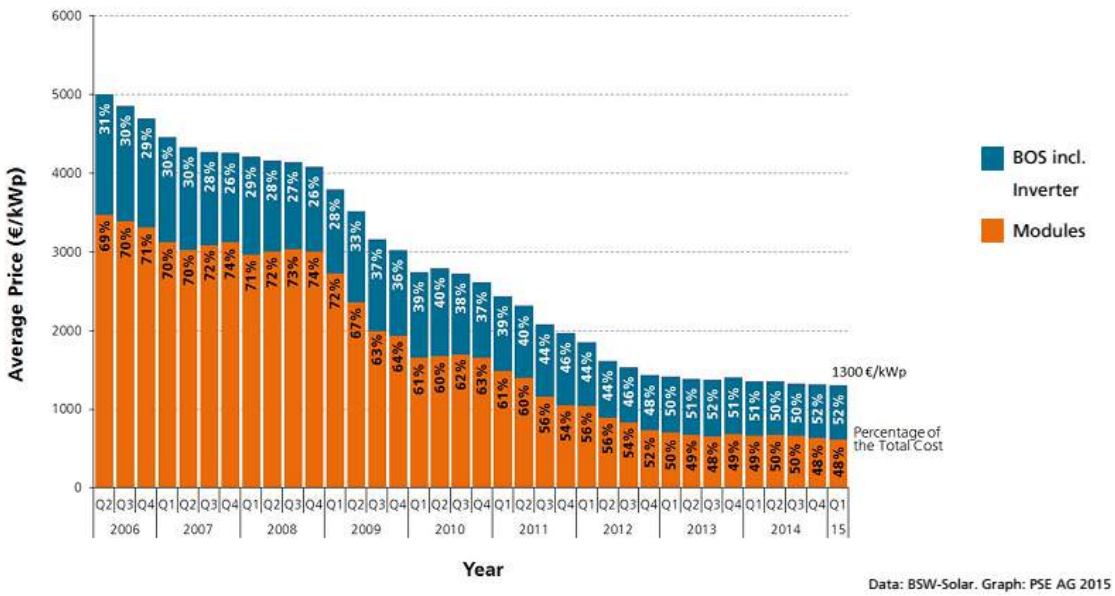

Figure 1.1.1: Average price for PV rooftop systems in Germany by Fraunhofer ISE [9].

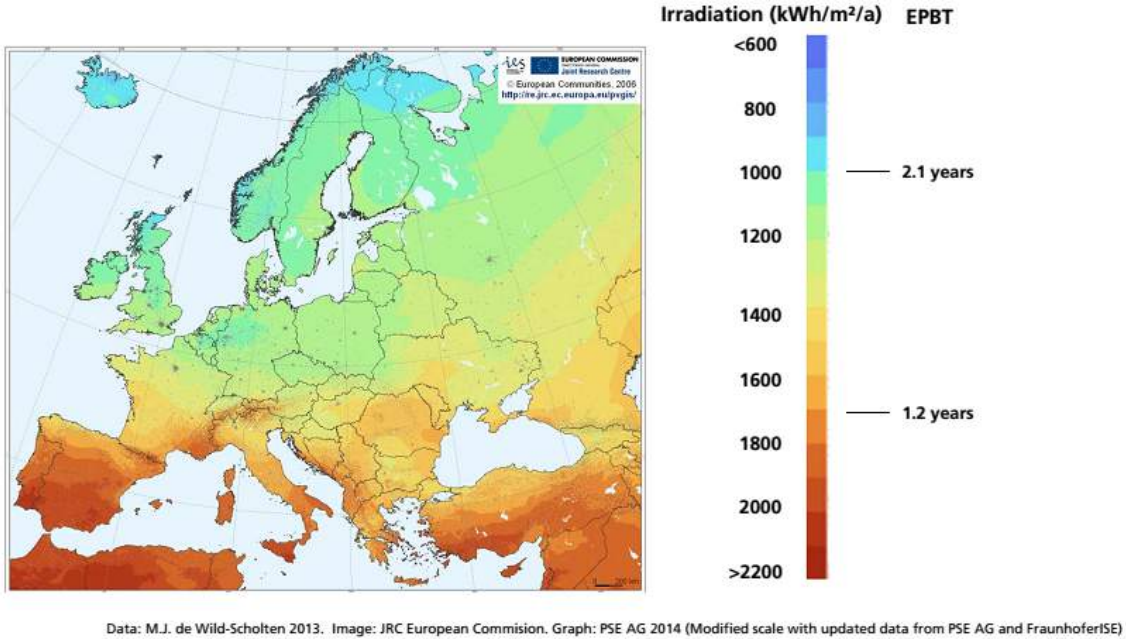

Figure 1.1.2: EPBT of multicristalline silicon PV system on the basis of the geographical position by Fraunhofer ISE [9].

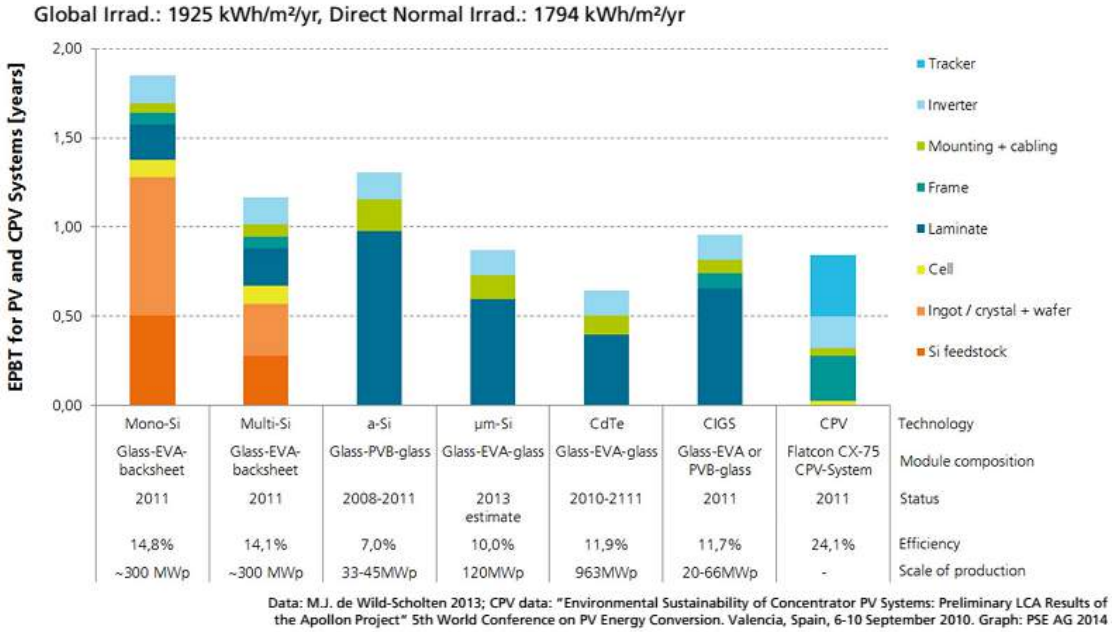

Figure 1.1.3: EPBT of PV rooftop systems in Catania (Italy) by Fraunhofer ISE [9].

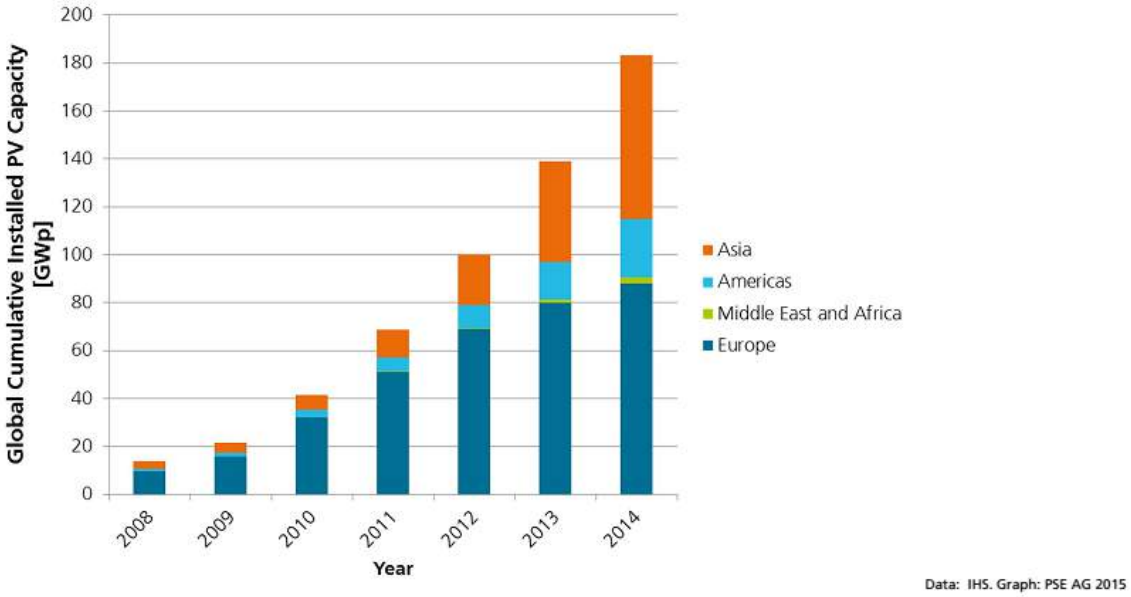

Figure 1.1.4: Global Cumulative PV Installation by Fraunhofer ISE [9].

EPBT, it depends on the irradiation levels, i.e. on the geographical location. Fig. 1.1.2 reports the EPBT related of multicristalline silicon PV system by considering the parameter presented above. As one can observe, in Northen Europe the EPBT is between 2-2.5 years, while in the south of Spain, Sicily or Sardinia, its value is equal about to 1 year. Obviously, the requested time to balance the initial cost of the system depends also on the technology, as shown in Fig 1.1.3 [9]. The decrease of the PV manifacturing cost, particularly in relation to cristalline silicon cells, is due also to the entrance of the China into the PV market [10]. In fact, in 2014, China producers lead the PV market with a share of 69%. Moreover, global annual production of China and Taiwan have passed from a value below 5 GW_p in 2009 to over 25 GW_p in 2015 [9]. Nevertheless the Asia leading position in the PV market, Europe confirms the hegemony on the global installations, with a share of 48% versus the 17% of the Asia competitors. Despite of this data, reported in Fig. 1.1.4, Europe contribution has decreased from 2013, where the share was 58%, and it is due to the exploitation of the asiatic installations (pass from 13% in 2013 to 17% in 2014). Thus, in 2014, the global PV power installed has been equal to 183 GW_p.

As shown in Fig. 1.1.3, the PV technologies can be subdivided in three main groups, that are: mono-silicon, thin film and multi-junction. The former is the oldest and the most reliable among the other technologies. The laboratory efficiency related to a mono-silicon solar cell is about 25% [11]. The thin film technology is characterized by the use of different semiconductors in addition to silicon, such as indium (I), cadmium (Cd), copper (Cu), tellurium (Te), etc. Moreover, the manifacturing process is based on a different concept. In fact, thin film solar cells are not wafer-based but are deposited on flexible substratum in thin layers. This technology has achieved now an efficiency equal to 14% [11]. Multi-junction solar cells represent the higher efficiency technology, thanks to the employment of multiple (commonly three) layers of semiconductors. In fact, these cells are manifactured by compound of III-IV materials, such as gallium arsenide (GaAs), indium, aluminium (Al), phosphorus (P) and germanium (Ge). Thus, by considering two or more junctions, a more light energy is exploited thanks to the different wavelenghts of light absorbed by each material. The efficiency of this technology depends on the concentration value and on the number of the junctions. In fact, because of multi-junction solar

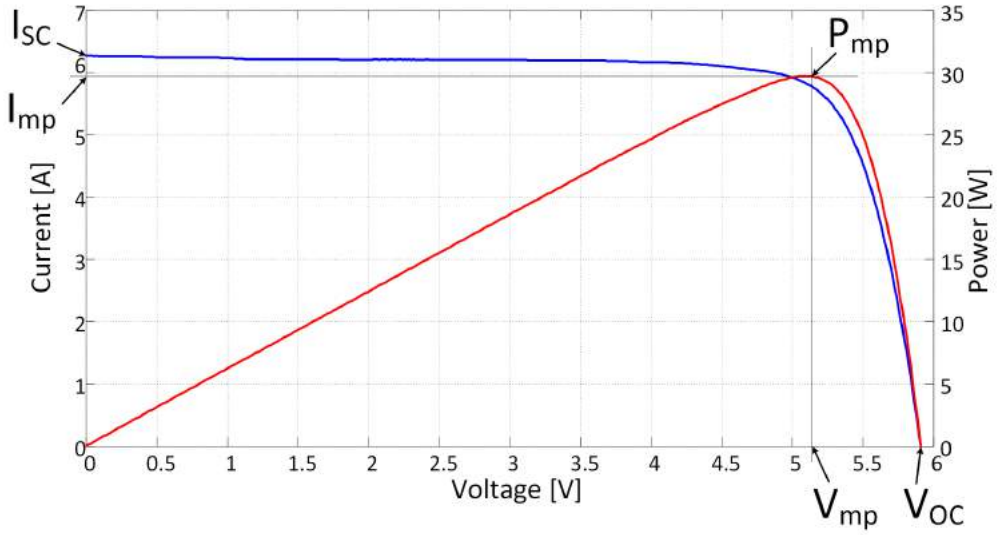

Figure 1.1.5: I-V and P-V characteristics.

cells are expensive, they are combined with concentrating optics and tracker system in order to reduce significantly the active area. On this optic, a multi-junction solar cell is considered a component of concentrating photovoltaic systems (CPV), that will be presented in the next Chapter, as a significant example of RES strongly unpredictable. Regarding the performance, Soitec has recently developed a CPV module characterized by an efficiency equal to 38.9% under Concentrator Standard Test Conditions (CSTC), and generally the commercial CPV modules have efficiency between 25-29%, unlike commercial silicon modules that reach efficiency about 16% [12].

The performance of a solar cell can be defined by taking into account its current-voltage (I-V) and power-voltage (P-V) characteristics, as shown in Fig. 1.1.5. These curves refer to a given irradiance value and change on the basis of the irradiance level and on the cell temperature, as reported in [7], [13]. Refering to Fig. 1.1.5, five parameters are highlighted:

1. I_{sc}: the current value in correspondence of a short circuit condition;

2. V_{oc}: the voltage value in correspondence of an open circuit condition;

3. I_{mp}: the current value in correspondence of which the output power is maximum (P_{mp});

4. V_{mp}: the voltage value in correspondence of which the output power is maximum (P_{mp}).

These parameters characterized a solar device for a given irradiance and for the standard operating temperature (25°C) and they are reported in the data sheet as reference value for the performance of the device [7]. Regarding to a mono-silicon solar cell, as the cell temperature rises, I_{sc} grows with a temperature coefficient equal to 0.1 mA/°C, while V_{oc} decreases with a temperature coefficient equal to -2.3 mV/°C [13]. Thus P_{mp} reduces by a factor of -0.5%/°C as well as the efficiency η, given by [13]:

$$\eta = \frac{P_{\text{out}}}{P_{\text{in}}} \tag{1.1}$$

where P_{in} is defined in [13]:

$$P_{\text{in}} = S * A_{\text{c}} \tag{1.2}$$

A_{c} and S being the active cell area and the irradiance level, respectively. The performance of the solar device is represented by another parameter, that is the Fill Factor (FF):

$$FF = \frac{I_{\text{mp}} * V_{\text{mp}}}{I_{\text{sc}} * V_{\text{oc}}} \tag{1.3}$$

It is worth noting that the FF, depending on the shape of the I-V characteristic, is a fundamental indicator if the solar device is working on suitable operating conditions. As will be reported in Chapter 2, the analysis of the FF gives important indications on the performance of the device under test and on the effectiveness of the improvements applicated on its structure in order to improve the efficiency. In Chapter 2, the characterization of two CPV devices will be presented. CPV systems represent the PV technology of the future with the higher efficiency among all the others ones. On this optic, my work has been focused on the CPV characterization,

especially regarding the employment of CPV systems in MGs. In fact, since CPV systems are characterized by a strong unpredictability due to the heavily sensitivy on the weather conditions, it is fundamental to know its behaviour in order to develop suitable management strategies in MGs with the aim to better exploit the energy produced.

1.1.2 Energy Storage Systems: State-of-the-art

As previously introduced, Energy Storage Systems (ESSs) represent a key component in the micro grid concepts. In fact, ESSs introduce several benefits to the power grid because of they operate not only as power sources but also as grid supporters. In particular, they can accomplish load levelling, peak shaving and improve the stability of the electrical system [14]. Moreover, ESSs allow the reduction of air pollution thanks to the decrease of hydrocarbon emissions related to the transmission and distribution of the electrical energy as well as they improve the reliability and power quality [14]. In this section the three most important technologies for grid support will be analyzed, that are battery storage systems (BSSs), supercapacitors storage systems (SSSs) and flywheel storage systems (FSSs) [14].

1.1.2.1 Battery Storage Systems

This technology (BSS) is based on the elettrochemical storage of the electrical energy. Altought BSSs have been introduced ealier compared to the other energy storage systems, they are considered presently the most cost-efficient technology [14]. BSSs can be subdivided into six tipologies:

1. *Lead-acid batteries* - In 1859, Gaston Plantè developed the lead-acid technology. The advantages of lead-acid batteries are mainly the cheapness and the depth knowledge acquired since now, but they are also characterized by a very low energy density and heavy weight [15], [14]. Nevertheless, presently many studies have been carried out to improve the lead-acid batteries performance, i.e. the employment of different materials for the electrodes, such as copper, in order to reduce the weight [14]. The power applications can vary from 1 kW (UPS) to 10 MW (transport and distribution systems). Lead-acid batteries are

often employed as support for residential and industrial photovoltaic systems [14];

2. *Nikel-based batteries* - Nikel-cadmium (Ni-Cd) batteries have been realized in 1899 by Waldermar Jungner, while nikel-metal hydride (Ni-MH) have been developed in 1989. Ni-Cd technology is characterized by a low energy density and extreme toxicity. For this reason, it has been replaced by Ni-MH. However, also Ni-MH presents a number of lacks, that are a high self-discharge rate, the rupture risk related to the charging process at high charge rate and, finally, a possible capacity reduction in the discharging process [15], [14]. Due to their low energy density, Ni-Cd applications were limited up to 0.5 MW, whereas Ni-MH is used for power applications up to 1 MW. In particular, Ni-Cd can be used for spinning reserve and stabilization [14];

3. *Zebra batteries* - This technology has been realized by the Zeolite Battery Research Africa Project (ZEBRA) in 1985. Nevertheless the high energy and power density, since these batteries operate at temperatures between 245 and 350°C, the thermal management is a critical issue. ZEBRA applications are between 100 kW up to 10 MW and they are appropriate for renewable energy sources support [15];

4. *Lithium-based batteries* - This technology, invented in 1970 by Michael Whittingham, presents many advantegous features such as high energy and power density, lightness, flexible charge and low self-discharge rate. The main lack is related to the internal resistance heating: for this reason, overcurrent and overvoltage protections are mandatory [14]. The lithium-based technology can be subdivided mainly into three groups: lithium-ion (Li-ion), lithium-ion polymer (LiPo) and lithium-iron phospate ($LiFePO_4$). LiPo technology has been developed as an evolution of lithium-ion one by presenting a greater life cycle and a lighter weight but it is penalized by an instability in case of overload and in general by a minor safety [16], [15]. Even though $LiFePO_4$ batteries are characterized by better safety, greater life cycle and higher power density compared to the other technologies, they have a poor energy density [15]. Lithium-ion batteries are employed in applications between 1 kW and 1 MW, in particular

for frequency regulation and RES support [14];

5. *Sodium-Sulfur batteries* - This technology (NaS) was developed in early 1970s. Similarly to ZEBRA, the operating temperature is in the range of 300-350°C. This characteristic, combined with the employment of dangerous elements such as the metallic sodium, have conducted to the introduction of sand in order to reduce the fire risk. NaS batteries operate in power applications from 0.8 to more than 10 MW. Thus, they are appropriate for wind farms applications as well as for demand peak reduction [14];

6. *Flow batteries* - This technology (FB) was developed in the 1970s, but the vanadium-redox (VRB) tipology was introduced only in 1980 by Maria Skyllas-Kazacos. Contrariwise the above technologies, VRBs electrolyte is not stored in the cell but in two tanks outside. The electrolyte in the tanks is the same and consequently the storage cost is reduced. Moreover, the electrolyte doesn't degrade over time and the VRBs life can reach even ten years [14]. Other types of flow batteries are the iron-chromium (FeCr), zinc-bromine ($ZnBr_2$) and zinc-air. FBs are used in power applications from 10 kW to more than 10 MW.

1.1.2.2 Supercapacitors Storage Systems

The electrochemical double-layer capacitors (EDLCs) was developed since 1950, but they were introduced in the market only in 1978 as "*supercapacitors*"[14]. EDLCs present several advantages compared to BSSs, that are mainly a lower internal resistance, a longer cycle life, reliability, no toxicity and, finally, the capacity to supply energy at higher power rating and a shorter discharge time [14]. For these reasons, EDLCs are employed principally in power quality applications [14]. Nevertheless, since the shorter discharge time, EDLCs are usually associated with BSSs for smart grid applications [14].

1.1.2.3 Flywheel Storage Systems

This technology (FSS) has been introduced in the 1950s thanks the adoption in Switzerland and Austria of the gyrobuses whose energy was stored in a flywheel [14]. The operating principle is the following: the FSS absorbs the energy by means of

the kinetic energy of a rotational mass and, when connected with a load, it supplies this energy by discharging [14]. Obviusly, FSSs are enclosured in a special packaging in order to guarantee the safety of the system in case of rupture [14]. The energy capacity is between 0.5 and 10 kWh but in the future FSSs of 25 kWh will be developed [14]. FSSs application is mainly in microgrid as well as for frequency regulation services, as reported in [14].

1.1.3 Electric Vehicles: State-of-the-art

Nowadays, the technological leadership in the automotive market is represented by internal combustion engine vehicles (ICEVs). However, their massive diffusion has led to air pollution growth especially in the cities, contributing at the same time to the global increase of greenhouse gas emission [17]. Since at least one quarter of greenhouse gas emission is accountable to the mobility sector, the environmental and energy policies have recognized at the automotive sector a primary role in the climate policies and have promoted its technological evolution, speeding up the transition from oil mobility to a sustainable one [15]. In particular, the international and local governments have set more severe gas emission limits in the automotive sector stimulating the introduction of cleaner fuels and especially of drive-train electrification into vehicle propulsion systems [15], [18]. Electric vehicles (EVs) don't produce tailpipe emissions, even if they are not zero-emission vehicles since the electricity used to recharge the battery has not been produced only by RESs [15]. The "*wells-to-wheels*"parameter refers to the emissions accounted to the entire life of the vehicle by considering, in addition to the direct emissions, also the ones related to the production of the energy needed to charge the vehicle [15]. Nevertheless, EVs are characterized by the lowest *wells-to-wheels* emissions compared to ICEVs [15]. Thus, EVs represent a key component for the reduction of the greenhouse emissions and moreover for the implementation of future power systems thanks to the higher efficiency of the powertrain employed and the possibility to realize a by-directional flow of energy with the power grid by implementing the V2G concept [19], [20], [18], [21], [22]. This is strictly connected to the possibility of managing the vehicle battery as a *dynamic distributed storage system* [21], [22]. Obviously, the employment of EVs in V2G paradigm will require the development of integrated control techniques able

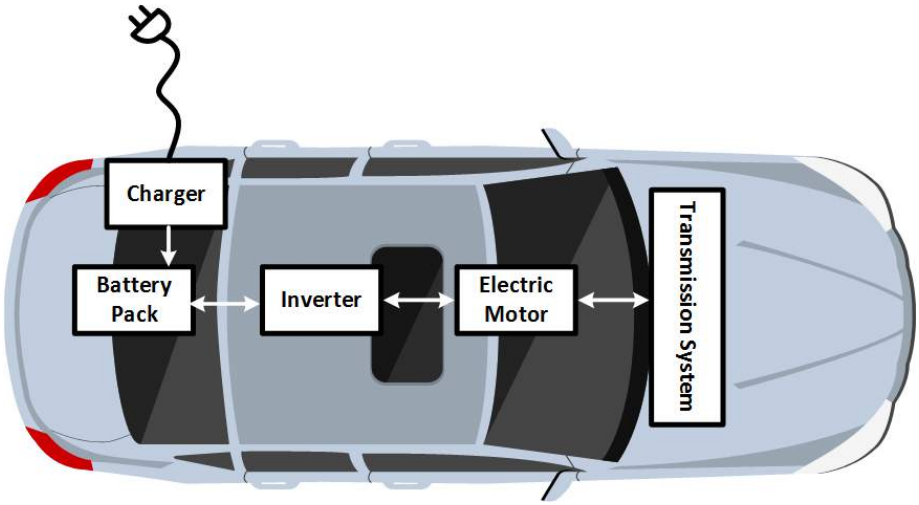

Figure 1.1.6: Typical BEV configuration.

to manage both the charging infrastructure and the power grid needs without impair the vehicle driving range. On the basis of these considerations, as it will be presented in Chapter 3, the EV simulation phase assumes a fundamental role in order to avoid time and cost expenditure during design and realization process and, moreover, to make the EV feedback information reliable for managing correctly and profitably an EV fleet inside a MG.

EVs are subdivided into three groups: Hybrid Electric Vehicles (HEVs), Plug-in Hybrid Electric Vehicles (PHEVs) and Battery Electric Vehicles (BEVs). The former is constituted by a combination of an electric motor and an internal combustion engine (ICE). Moreover, HEVs can not be charged throught the power grid and the battery energy is provided by the ICE or by means of the regenerative braking [15]. PHEV battery is larger than the HEV one and the charging process is realized throught an infrastructure connected with the distribution grid [15]. As reported in Fig. 1.1.6, the BEV propulsion depends only on the electric motor. Consequently, the driving range of the vehicle is related to the battery capacity which must be enough to guarantee a suitable driving range. For example, the Nissan Leaf is powered by a lithium-ion battery of 24 kWh and consequently the driving range is equal to 160 km with a single charge [15]. Because of their structure, BEVs have initial costs higher than PHEVs caused principally by the larger energy storage system.

Nevertheless, thanks to recent developments in the electrochemical sector and to the novel approach in the BEV design, in the next future a significant price decrease of this class of vehicle is expected [23].

Regarding the battery, only some of those presented in Section 1.1.2.1 are suitable for vehicle applications. Lead-acid battery have been the first one employed in the automotive sector. Despite the cheapness and the depth knowledge acquired since now, they are also characterized by a very low energy density and heavy weight [15], [14]. Thus, lead-acid batteries have been replaced by nikel-based ones, whose energy density are higher than the former. However, also nikel-based batteries present a number of lacks, as reported in Section 1.1.2.1 [15], [14]. At the same time, Zebra batteries have been taken into account to be employed in the automotive sector thanks to their high energy and power density. Nevertheless, since their high operating temperature, the thermal management is an important issue that had lead to substitute this technology with the lithium-based one, the present dominant technology in the electric vehicle sector [15]. In fact, the most important BEVs in the automotive market are powered by lithium-ion batteries, such as Nissan Leaf, Mitsubushi i-MiEV, Testa Model S, BMW i3 and Smart Electric Drive [15]. This technology present many advantegous features compared to the other ones: high energy and power density, lightness, flexible charge and low self-discharge rate. The main lack is related to the internal resistance and, for this reason, lithium-ion batteries are equipped by overcurrent and overvoltage protections. As stated in Section 1.1.2.1, the lithium-based technology can be subdivided mainly into three groups: lithium-ion (Li-ion), lithium-ion polymer (LiPo) and lithium-iron phospate ($LiFePO_4$). LiPo technology has been developed as an evolution of lithium-ion one by presenting a greater life cycle and a lighter weight but it is penalized by an instability in case of overload and in general by a minor safety [16], [15]. Even though $LiFePO_4$ batteries are characterized by better safety, greater life cycle and higher power density compared to the other technologies, they have a poor energy density [15]. Thus, on the basis of the characteristics reported above and in Section 1.1.2.1, it is worth noting that each battery technology has different applications in relation to many factors. In particular, regarding the automitive sector, the most important parameters to take into account are the vehicle class (sports or economic cars for example), the

driver needs (urban or extra-urban paths) and the battery cost.

Nevertheless the numerous advantages previously reported, the BEVs connection with the power grid introduces a number of problems, that are mainly harmonics, system losses, stability issues and increase in the power demand [15]. In particular, as discussed by [15], BEVs produce on the load profile of the power grid an important impact if the charging process is not controlled by a suitable management. In fact, if the driver is allowed to charge the vehicle at any time, the effects of the charging process on the load profile are concentrated principally in the peak hours that correspond to the arrival at work and the return at home periods [15]. On the other hand, [15] reports studies whose state that an uncontrollable charge of a BEV fleet of one million do not introduce considerable increases in the peak load. The solutions to this unwanted phenomenon are mainly two: the introduction of *time-of-use* (TOU) tariffs, in order to encourage the users to charge the vehicle at different hours than the peak ones, and a suitable energy management strategy that allows the vehicle charging by respecting both the power grid requirements and the driver needs [15]. Moreover, as previously discussed, the BEVs represent a key component for the implementation of the future power systems concept of smart grid, thanks to the possibility to realize a by-directional flow of energy with the main grid by implementing the V2G paradigm. As defined in [15], smart grid can be considered as an intelligent power grid that improve the stability, the efficiency and the reliability of the power supply thanks to a smart control of the energy flows of each interconnected components. In this optic, V2G represents a key technology for smart grid and micro grid concepts because it allows the increase of the exploitation of RESs and, moreover, because of it accomplishes several benefits to the power grid, that are principally: ancillary services, peak load shaving and load levelling, reactive power support, harmonic filtering [15]. Since now, on the basis of the existing EV charging structures, V2G has been possible only as uni-directional technology [15]. In this way, the energy flow goes only from the power grid to the vehicle without impair the battery capacity. Moreover, by adopting convenient TOU tariffs and a suitable MS that provides the charging at off-peak hours, a reduction of power losses and cost saving will be reached [15]. In the next future, the introduction of bi-directional chargers will allow a bi-directional communication (of data and energy) between the

power grid and the EVs. V2G technology can be subdivided in [15], [18]:

1. *Vehicle-to-home (V2H)*: the contest refers to a *home automation network* (composed by an EV, loads and a PV system for example) where the EV storages the PV power production and provides this energy when the RES production is low;

2. *Vehicle-to-vehicle (V2V)*: the contest is a parking lot (of commercial or working buildings) where an aggregator manages the energy flows between the vehicles;

3. *Vehicle-to-grid (V2G)*: in this case the energy exchange is between the vehicle and the power grid. Thus, the EV is charged or discharged on the basis of the management strategy. In V2G, EVs operates also for grid support, such as for example load levelling or peak shaving.

Among all the benefits introduced by the V2G paradigm, one of the most important is the support in the exploitation of RESs. In fact, the RESs presence in the power grid has been mandatory in order to reach a reduction of the pollution and to create a cleaner electrical system [15]. Nevertheless, RES systems are strongly unpredictable due to their dependence on weather conditions. Thus, this intermittency introduces power fluctuations in the main grid by reducing the stability. In order to avoid this phenomenon, RESs energy can be managed by means of stationary storage systems (ESSs) that absorb the RES surplus production and, when it needs, provide this energy to the power grid. However, depending on the RES size and on the contest, the adoption of ESSs in combination with RESs could be an expensive solution [15]. Consequently, the introduction of the V2G paradigm can represent a fundamental innovation for the power grid. Thanks to the bi-directional exchange of energy, EVs can be considered as *distributed energy storage* whose employment leads to stabilize the fluctuations introduced by RESs and to improve their exploitation. In addition, the V2G paradigm can lead to other benefits, such as the remuneration possibility thanks to the partecipation to ancillary services. Thus, the end-consumers will be encouraged to make their EVs available for grid support if a profit is possible. In conclusion, the combination with RESs and EVs can produce a number of benefits, in particular with the aim to get a smarter and cleaner power grid.

Finally, as previously stated, a suitable management strategy in a EMS is fundamental to guarantee the stability and the reliability of the MG. Regarding the case presented in Chapter 4, a management strategy that aims to improve the MG energy self-consumption thanks the suitable management of the EVs charging/discharging process on the basis of the RESs production is presented.

I have heard articulate speech produced by sunlight
I have heard a ray of the sun laugh and cough and sing!
I have been able to hear a shadow, and I have even perceived
by ear the passage of a cloud across the sun's disk.

Alexander Graham Bell

2

Concentrating Photovoltaic Systems

One of the most promising new technologies for improving the efficiency of PV systems is represented by the concentrator photovoltaic one (CPV). Nowadays, a traditional silicon flat-plate module produced by SunPower has reached a maximum efficiency equal to 25%. By adopting a silicon heterostructure, Panasonic has produced in 2015 a module characterized by an efficiency of 25.6%, as reported in Fig. 2.0.2 [11]. It is worth noting that there is an efficiency physical limit equal to 31% by considering a single p-n junction solar cell, as defined by Shockley-Queisser in 1961 [24]. This is due to the fact that a single junction is enable to generate power by absorbing from a specific wavelenght of light, while the rest of the energy is lost because of recombination, unabsorbed photons and thermalization phenomena. The introduction of the multi-junction solar cells has push efficiency higher than the limit presented above. In fact, if silicon cells could reach a maximum efficiency of 31%, multi-junction solar cells have a theoretically maximum efficiency equal to 86% [24]. These cells are manifactured by compound of III-IV semiconductors, such as GaAs, In, Al, P and Ge. Thus, by considering two or more junctions, a more light energy

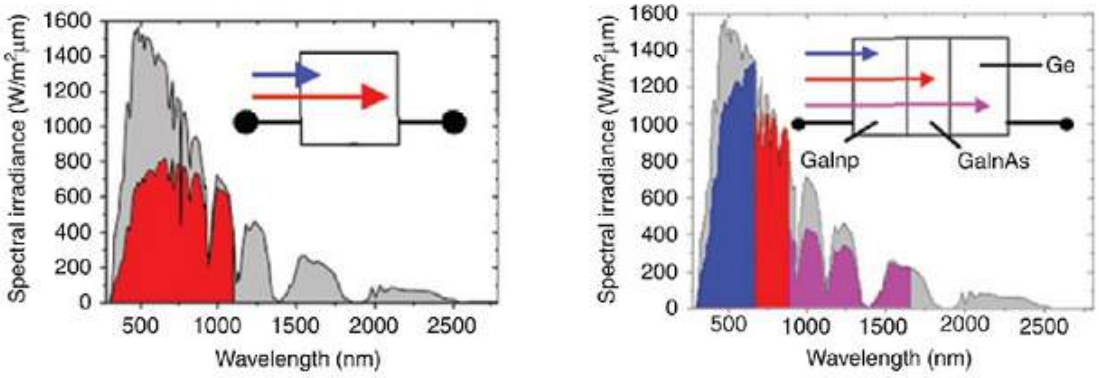

Figure 2.0.1: Comparison between a single and a three-junction solar cell by Antonio Luque from Institute of Solar Energy - UPM Madrid [24].

is exploited thanks to the different wavelenghts of light absorbed by each material. Moreover, one of the most used materials in multi-junction solar cells, GaAs, is characterized by a thermal coefficient about half of the silicon one that allow a better thermal performance [24]. The comparison between a silicon and a three-junction solar cell is reported in Fig. 2.0.1.

Nevertheless the higher efficiency, the III-IV materials are much more expensive than the silicon used in traditional flat-plate modules. Consequently, the reduction of the active area is mandatory in order to exploit the multi-junction solar cells advantages presented above. The adoption of cheap optic systems has permitted to concentrate the light into the solar cell whose active area is reduced on the basis of the level of the concentration. The CPV systems can rise untill 2,000 suns, where 1 sun refers to an intensity of light incident (called irradiance) onto a solar cell equal to 1000 W/m^2 [25]. Irradiance is also defined as the power received per unit of area normal to the sunlight [25]. The concentration could be subdivided in three levels, such as high, medium and low. In this way, generally a solar cell sizes even 1 mm^2. Moreover, the employment of a solar tracker is mandatory in concentrating systems, in order to always focus the light in a single spot into the solar cell. Unlike low concentrating systems that employ single axis or linear trackers, the high concentrating ones need a double axis tracker. As it will explained in the next sections, higher the concentration level higher the tracker system accuracy.

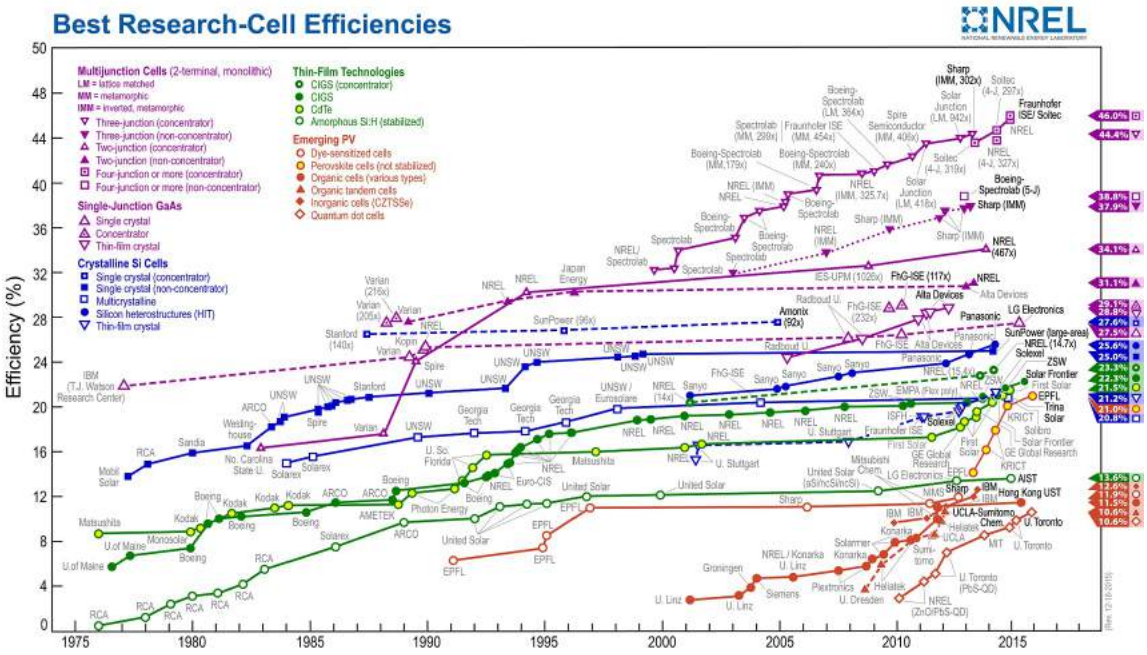

Figure 2.0.2: Best Research cell efficiency by National Renewable Energy Laboratory (NREL)[11].

Nevertheless, due to the complexity of the system, the CPV technology is not yet competitive in the PV market. The critical factors that limit the CPV growth are the following: high initial and maintenance costs, performance dependence on variation in environmental parameters (such as direct normal irradiance, solar spectrum, ambient temperature and wind speed), tracking errors and optical misalignment [26]–[27]. In the next future, CPV costs are expected to decrease by employing cheaper materials, more efficient optics and by the effect of economies of scales. Therefore, outdoor characterization is fundamental to point out the critical aspects of the tested CPV systems in real operating conditions and, consequently, to determine the improvements necessary to increase the system reliability. Moreover, the characterization process is also fundamental if the CPV plant operates in MG. In fact, the knowledge of the issues related to the CPV technology highlighted during the characterization process allows the development of suitable management strategies, in order to guarantee the quality, the reliability and the controllability of the MG and consequently of the main electrical power system, expecially in presence of a large number of RESs.

In the next sections the state-of-the-art and the physical parameters of the CPV technology, the two prototype characterizations and finally the role of CPV systems in MGs will be introduced.

2.1 State-of-the-art

As reported in the introduction, CPV systems can be classified on the basis of the level of the concentration and on the optics employed. Moreover, a CPV system must be constituted also by a tracking structure, whose typology (single or double axis) depends on the level of the concentration. As reported in Fig. 2.0.2, the current efficiency record of 46% has been reached by Fraunhofer ISE by testing in laboratory a four-junction solar cell. In the next future, solar cells composed by five, six or more junctions will be manifactured, reaching efficiency higher than 50%. In relation to the PV market, Soitec has recently developed a CPV module characterized by an efficiency equal to 38.9% under Concentrator Standard Test Conditions (CSTC), and generally the commercial CPV modules have efficiency between 25-29%, unlike commercial silicon modules that reach efficiency about 16% [12]. Since 2016, when the first CPV plant over 1 MW has been installed in Spain, the number of commercial CPV systems is increased annually [12]. In Fig. 2.0.2 the three most relevant CPV power plants exceeding 20 MW are reported [12]. By observing the geographical distribution of the installed CPV power plants, it is worth noting that the best suitable installation site is characterized by DNI values over 2000 kWh/m^{2}y. In fact, the main countries in which CPV systems have been exploited are United States (in particular California), China, Australia, South Africa, Spain and Italy. Nowadays, the CPV market is expected to have a volume about 25 MW_p, while in 2014 it was equal to 70 MW_p. Fig. 2.1.2 shows the yearly installed CPV capacity up to 2014 [12].

Figure 2.1.1: From top to bottom: 30 MW plant in Alamosa (Colorado) by Amoniz; 44 MW in Touwsrivier (South Africa) by Soitec; 140 MW in Golmud (China) by Suncore. By Fraunhofer ISE [12].

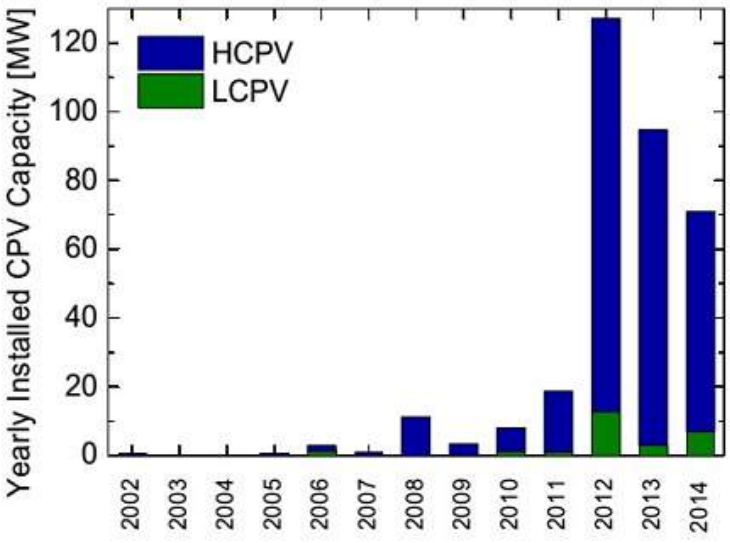

Figure 2.1.2: Yearly installed CPV capacity by Fraunhofer ISE [12].

2.2 Physical Principles of CPV systems

Before to introduce the characterization process of the two considered prototypes, it is mandatory to present the physical principles of a CPV system. The main parameter to take into account is the effective concentration level, C, that is the ratio of the average concentrated irradiance onto the solar cell divided by the direct irradiance (DNI) on the optic system (before concentration step). The mathematical espression is shown in (2.1) [25]:

$$C = \frac{I_{\mathrm{sc}}(C)}{I_{\mathrm{sc}}(1sun)} \tag{2.1}$$

Consequently, the optical efficiency is defined by (2.2):

$$\eta_{\mathrm{op}} = \frac{C}{X} \tag{2.2}$$

where X is the concentrator factor and is reported in (2.3):

$$X = \frac{A_{\mathrm{i}}}{A_{\mathrm{r}}} \tag{2.3}$$

where A_i and A_r are the optical system area and the active area, respectively [25]. Finally, a CPV system is defined also by considering the Concentration Acceptance Product (CAP):

$$CAP = ((X)^{1/2} * sen\alpha) \tag{2.4}$$

α being the acceptance angle, i.e. the angle above which the output power of a CPV system decreases below 90% of its nominal value. Since CAP value is constant, more X increases more α reduces [25]. Thus, an high concentrator system requires a small acceptance angle, whose value should be one order of magnitude smaller than the pointing error of the tracking system. Consequently, it is worth nothing that for high level of concentration a dual axis tracker is mandatory [28].

2.3 Prototype Characterization

The CPV technology complexity related to several parameters, such as dependence on environmental factors, tracking errors and optical misalignment, requests an accurate characterization in order to point out the operating critical aspects of the considered system. In particular, a deeper knowledge of the real behavior of a CPV module and of the influence of weather parameters on its energy performance is highlighted by the outdoor characterization. Nevertheless, this process is very complex and affected by environmental variations. On the contrary, indoor tests, which allow to carry out repeatable measurements under controlled environmental conditions, are fundamental in the rating process of CPV modules [29].

Following all these considerations, a detailed and accurate optical and electrical characterization is a fundamental tool in the development and design optimization of a CPV device and demonstrate its benefits in the identification of the system design problems and in the evaluation of the effects of the implemented solutions.

2.4 Refractive Optic

Based on the geometry of the optical system, a CPV device can be divided in refractive (such as Fresnel lenses) and reflective (such as parabolic mirror) optics based system [30]. Currently, the main part of the CPV modules in the market employs refractive optics because of their cheapness and minor complexity. In fact, Fresnel lenses are usually made with low cost PMMA lenses characterized by a typical thickness of 4-5 mm. However, the Fresnel lenses introduce chromatic aberration phenomena which contribute to the degradation of the overall system performance [31]. Moreover, the distribution of concentrated light is a critical issue and can cause an incorrect heating, leading to hot spot effects that increase the series resistance and the solar cells degradation. To overcome this problem, a secondary optical element represented by a homogenizer is usually implemented [32]. In this section the characterization of a CPV device is introduced. The tested module is composed by a refractive optic system and four triple-junction solar cells. Thus, the tests performed on the first CPV prototype have been presented and discussed, revealing the main defects of the developed device. To overcome the identified problems and to improve the system efficiency, an upgraded version of the prototype has been developed and characterized showing significantly higher performance [33].

2.4.1 Prototype Description: First Version

In this subsection the general design and assembly of both prototypes versions are presented. The prototypes comprise four CPV receivers, each one composed of the following elements: a (InGaP/GaAs/Ge) concentrator triple junction (CTJ) solar cell, a PMMA Fresnel lens as a primary optical element (POE) and a reflective homogenizer as a secondary optical element (SOE). The CTJ cell is a square with an area of 100 mm^2. Every POE has dimensions of 200 x 200 mm^2, a thickness of 3 mm and a focal length of 250 mm. The POE gives a geometrical concentration factor of 400x on the CTJ cell surface. SOEs are made of reflective aluminum pipes, folded in order to form a truncated pyramid with square basis. The use of homogenizers was aimed at improving the uniformity of the concentrated solar light reaching the CTJ cell. Four CPV receivers are placed inside the housing frame, made of four lateral

Figure 2.4.1: CPV module prototype.

aluminum panels, each one 405 mm x 270 mm large, glued on a flat aluminum rear panel, of which dimensions are 400 x 400 mm^2, as reported in Fig.2.4.1. To provide an excellent assembly of the whole module, the Zemax ray tracing software has been used to simulate the optimal positions and dimensions of cells and homogenizers, as well as the best distances between Fresnel lenses and the photovoltaic cells. Moreover, the complete 3D design and assembly of the system have been developed, as reported in Fig. 2.4.2. The analysis on Zemax ray tracing software and the characteristic of the CTJ solar cell have allowed the estimation of the module efficiency of the first prototype equal to about 15%.

2.4.2 Outdoor Characterization

Both prototypes have been tested in Sardegna Ricerche Laboratory, situated in the south of Sardinia, Italy (39°14'52.933"N; 8°58'17.306"E). The site irradiance conditions have been examined in order to determine Direct Normal Irradiance (DNI) and Global Normal Irradiance (GNI) values [34]. Obtained results show that the site is characterized by high DNI and DNI/GNI values, which makes it an excel-

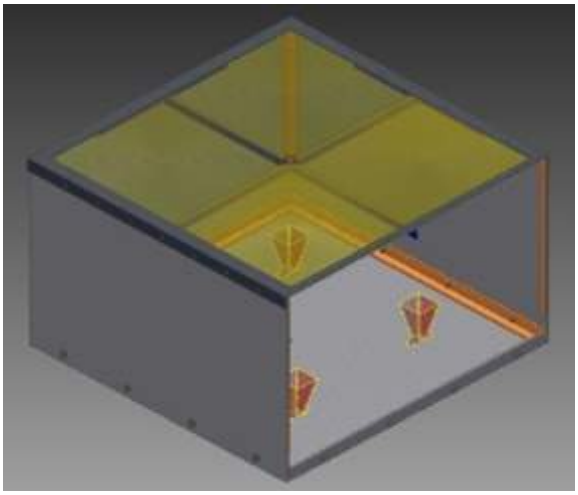

Figure 2.4.2: 3D design of the CPV module.

lent location to perform the outdoor tests on CPV modules according to IEC 62670 standard [35]. The adopted measurement and test system, shown in Fig.2.4.4, consists mainly of a Keithley 2651A high power source-meter, used both as I-V curve tracer and as MPPT unit. The tests have been controlled by a laptop PC, running software written in the LabVIEW programming language. I-V and P-V curves have been acquired by programming the Keithley source meter to automatically generate variable voltage steps and collect current and voltage quantities at predefined intervals. The measured data allowed to determine the characteristic module parameters: short-circuit current (I_{sc}), open-circuit voltage (V_{OC}), maximum power (P_m), maximum power current (I_{mp}), maximum power voltage (V_{mp}) and Fill Factor (FF). The outdoor facility of Fig. 2.4.4 also includes a meteorological station, equipped with an anemometer and an ambient temperature sensor, while a pyrheliometer to measure DNI and a pyranometer for GNI have been mounted on the solar tracker. The CPV cells temperatures have been measured by using NTC thermistors, placed inside the prototypes, in the direct proximity of the photoactive area. All values have been stored and the user can control the data in every moment looking at the graphical user interfaces (GUIs), as shown in Fig. 2.4.3. Thanks to this configuration, the electrical and environmental parameters could be acquired simultaneously. In fact, the simultaneous acquisition of electrical and environmental data is of particular impor-

Figure 2.4.3: Acquisition systems in the Sardegna Ricerche outdoor facility.

tance for the correct assessment of the real performance of devices under tests [36]. During the outdoor tests, prototypes have been placed on a biaxial solar tracker in order to focus correctly the sunlight onto the cell surface. The accuracy of tracking has been assessed with the AKKUtrack instrument and is of 0.01° in tilt and 0.15° in azimuth, fulfilling the requirements prescribed in IEC 62108 standard [37]. A closed-loop sun position control is achieved by a four-quadrant sensor coupled with a Heliotrack dual-axis tracking controller and mounted on the solar tracker [30], [38].

2.4.3 Electrical Characterization

The results of the outdoor test reported below refer to a test performed at DNI of 880 W/m^2. Fig. 2.4.5 shows the I-V and P-V characteristics, while the outdoor characterization results have been reported in Table 2.4.1. The module efficiency (λ_{mod}) and the *FF* have been determined according to (2.5) and (2.6) [39]:

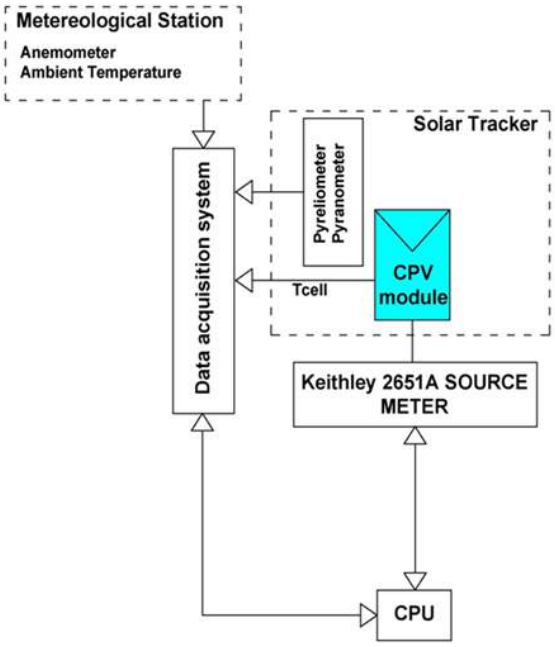

Figure 2.4.4: Scheme of the experimental setup.

$$\lambda_{\text{mod}} = \frac{P_m}{DNI * A_{\text{LENS}}} \tag{2.5}$$

$$FF = \frac{P_m}{I_{\text{sc}} * V_{\text{oc}}} \tag{2.6}$$

where (A_{LENS}) is the lens area. As can be noticed from Table 2.4.1, the prototype efficiency is much lower than expected and the causes of such energy losses and poor performance need to be deeply investigated to support the design of an improved prototype version. From the analysis of Fig. 2.4.5, it is clear that the module current-bias characteristic is affected by distortions in both horizontal and vertical parts. These are the effects of different power losses, related to the following resistive elements: semiconductor layers, tunnel junctions, emitter, front contact and metal gridlines, wires, soldering of wires and shunt resistance. These resistive elements could be lumped in two main circuital components: the series and the shunt resistance. The maximum voltage depends on both resistances by a non-linear

Table 2.4.1: Characterization results of the first CPV module prototype

Parameter	Symbol	Value	Unit
Short circuit current	I_{sc}	2.61	A
Open circuit voltage	V_{OC}	10.14	V
Maximum power	P_m	14.39	W
Fill Factor	FF	0.54	-
Module efficiency	η_{mod}	10.2	%

function, while the FF is mainly influenced by series parameters [40]. As reported above, the series resistance is composed by two types of contributions: the first are influenced by the solar cell architecture and could be reduced by applying changes in the construction phase, while the last depends on the assembly accuracy [40]. Moreover, the series resistance can greatly increase because of hot spot phenomena and spatial non-uniformity of the irradiation, both caused by the adopted optical system [39]. The quantification of these parameters is hence essential to understand how they affect the CPV prototype performance and to improve the whole system efficiency. With the purpose of achieving this result, the evaluation of the prototype series and shunt resistances have been performed, taking into account the equivalent circuit proposed in [39]. Several methods are available in literature to evaluate series and shunt resistances [41]-[42]. In this work, the method proposed in [42] has been used. By considering the solar cell dark curve, it evaluates only the contribution of the wires and soldering resistances, since the other components occur only when the cell is illuminated. The characterization data have been elaborated in Matlab environment. A series resistance value of 400 mΩ and a shunt resistance equal to 6.45 Ω have been found consequently. These results numerically demonstrate that both series and shunt resistance values are far from the ideal ones. In particular, the high value of the series resistance is primarily due to the solders between the electrical cell contacts and the wires while the low shunt resistance mainly depends on the characteristics of the solar cell materials and optics.

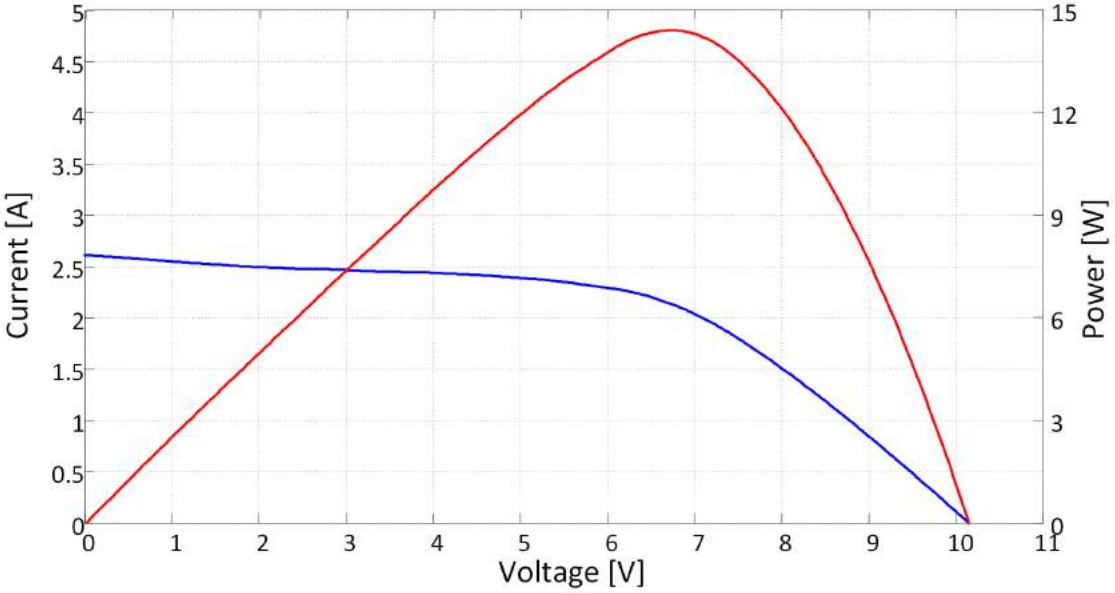

Figure 2.4.5: I-V (blue line) and P-V (red line) curves of the CPV prototype.

2.4.4 Optical Characterization

An important concern in the optical design of point-focus CPV systems is the non-uniformity of the irradiance distribution on the cell plane, produced by the optics. The effects on the solar cell performances, derived from an inhomogeneous illumination profile, are distributed throughout the device, with the metal grid, emitter and front contacts resistances constituting the main sources of losses [43], [44]. In particular, the non-uniformity of the concentrated solar light causes high illuminated areas and hot spot phenomena which result in an increase in the effective series resistance. This in turn translates into a drop in both FF and efficiency, affecting the overall solar cell performance, as explained in the foregoing subsection. All these issues are to be tackled during the CPV system design and prototype assessment processes in order to obtain a better spatial uniformity of the concentrated light and consequently optimize its performances. Following these considerations, the irradiance spatial distribution of the proposed CPV device should be carefully determined and analyzed. In the scientific literature, the effects of inhomogeneous illumination distribution on the CPV solar cell have been commonly evaluated by simulations based on distributed circuit models [45]. However, simulations provide reliable results only

if accurate data for the solar cell distributed model are available and the irradiance profiles over the cell are known. Illumination patterns are usually simulated starting from optic systems models which can hardly reproduce with high accuracy the actual profiles produced by manufactured optics [43]. Therefore, to determine the true irradiance distribution produced by the optics used in the first prototype, an ad-hoc characterization procedure has been employed. The experimental set-up used to capture the irradiance profiles at the exit of the CPV optical system is shown in Fig. 2.4.6. The solar simulator Abet Technologies Sun 2000 11048 has been used as light source. The simulator spot image on the receiver plane has been analyzed in a previous work [46], showing the presence of areas characterized by different irradiance levels, which cause hot spot phenomena over the solar cell. In order to understand how the optical elements modify spatially the light distribution, the irradiance profile has been captured by a CCD camera. The method uses a Lambertian diffuser placed at the focus of the Fresnel lens. The diffuser receives the concentrated light over the front side and transmits it on the back side, producing an image of the irradiance distribution of the incident light [47]. The spot image is then captured by the CCD camera located behind it and finally processed using Matlab software.

Fig. 2.4.7 shows the irradiation distribution on the Fresnel lens focal plane which has the same features of the light profile of the solar simulator spot image [46]. As can be observed in Fig. 2.4.7, this flux distribution determines areas illuminated at an irradiance level 250 times higher than the less irradiated ones, leading to an increase in the effective series resistance and, therefore, to a drop in the *FF*. At the same time, non-illuminated areas work as dark diodes, contributing only with recombination current but not with photo-generation [48]. The introduction of a secondary optical element, namely the reflective homogenizer, has the purpose to improve the uniformity of the irradiance distribution over the triple-junction solar cell, as well as to enhance the acceptance angle and increase the concentration factor [43], [49]. As can be noticed from Fig. 2.4.8 and 2.4.9 the homogenizer used in the CPV prototype has not accomplished the flux homogenization task. The geometrical characterization and the flux mapping have showed a poor spatial irradiation uniformity with several hot spots concentrated on the top-right region of the cell

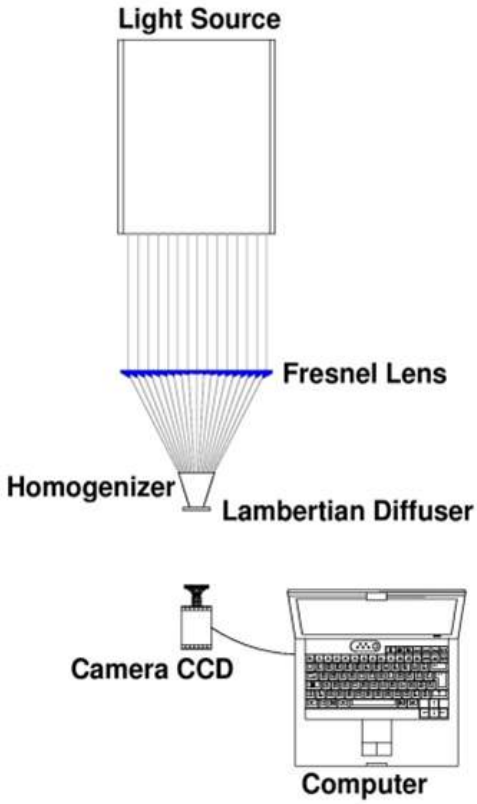

Figure 2.4.6: Experimental set-up for the determination of the irradiance distribution.

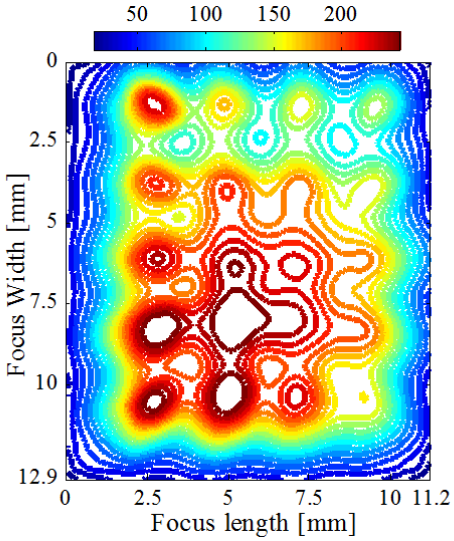

Figure 2.4.7: Irradiation profile on the focal area of the Fresnel lens.

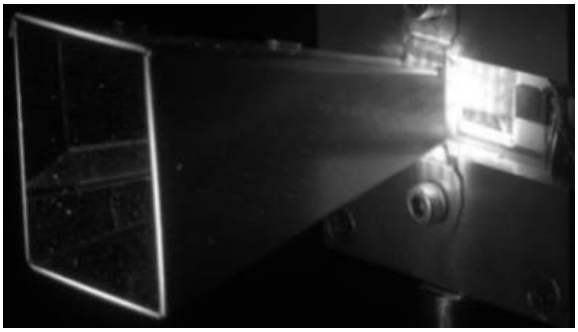

Figure 2.4.8: Spot image of the light distribution on the cell plane after interposition of the reflective homogenizer.

area. This difference in the geometrical symmetry between the spatial irradiation distribution introduced by the Fresnel lens and then modified by the homogenizer is probably due to internal reflection phenomena on its surface. The presence of localized high intensity peaks after the interposition of the homogenizer is one of the main reasons of the module performance degradation. This suggests the adoption of a new homogenizer configuration in order to improve the overall system efficiency.

2.4.5 Thermal Characterization

The electrical conversion efficiency of a solar cell greatly depends on its operating temperature that can rise considerably under light concentration. In fact, the conversion efficiency of solar cells decreases with increasing temperature. Such a phenomenon results from the significant reduction of open-circuit voltage caused by an increase in the cell temperature, which affects also the maximum delivered DC power and consequently the overall system performance [50]. These effects are enhanced when optical concentration is employed, suggesting the need of a complete monitoring of temperature levels which CPV solar cells reach during on-sun operations. Different tests has been carried out on the CPV prototype in order to determine the temperature profiles of CTJ cells in real operating conditions and to investigate to what extend their thermal dynamics influence the module performances. The results here reported refer to measurements carried out on a time window longer than three hours at a mean *DNI* of 890 W/m^2. The experimental data show an extremely fast

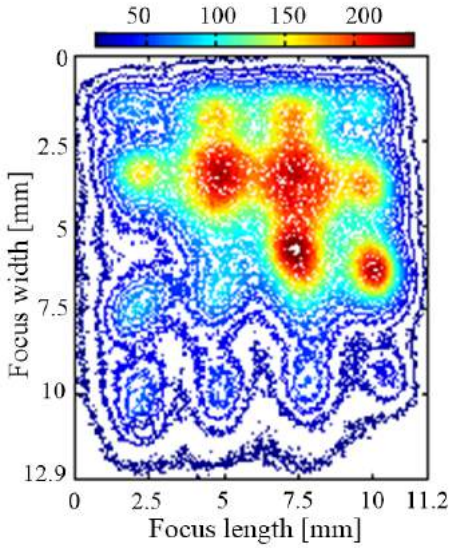

Figure 2.4.9: Irradiation profile of the light distribution on the cell plane after interposition of the reflective homogenizer.

rise in the cells temperature from about 40°C to 80°C in one minute, rising to 100°C in less than ten minutes, at an ambient temperature of 30-35°C. Such a temporal evolution of the temperature, which is reported in Fig. 2.4.10 for the sake of completeness, has entailed a drastic drop in the module performance. For instance, at the end of the test, the efficiency had decreased by 10.4% respect to the initial value. These outcomes clearly point out the importance of correctly managing the operating temperature of a CPV module [51]. In order to minimize the CPV prototype temperature levels, the module thermal heat sink has been improved by using thermal conductive paste layers. In Fig.2.4.10 the better heat dissipation obtained with this second configuration can be observed. After about six minutes, the cell temperature was equal to 67°C, i.e. 30°C lower than the temperature reached in the first case. Measurements performed on the module, operating at ambient temperature of 33°C and *DNI* of 875 W/m^2, confirmed the good thermal behavior of the new heat sink configuration.

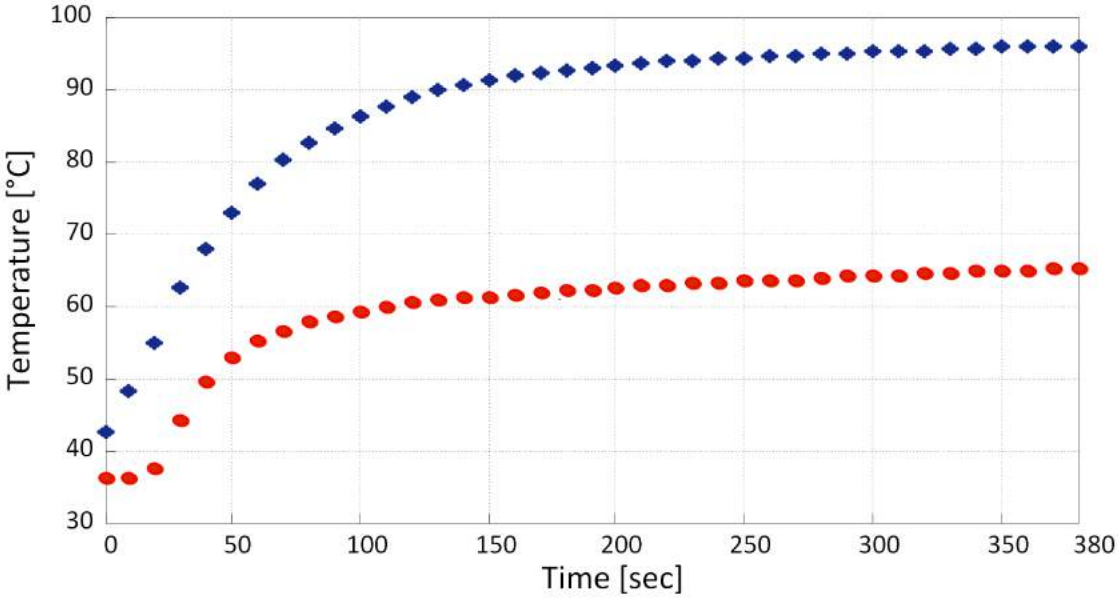

Figure 2.4.10: Receiver temperature (blue line, first version; red line, secondo version) vs time.

2.4.6 Improvements

The second version of the prototype has been thought and realized in order to overcome the problems encountered in the first version. This section points out the differences between the two prototypes and presents the measurements performed on the second one. The characterization performed on the first prototype showed that the recorded efficiency losses were mainly correlated to the high non uniformity of irradiation on the active area. To improve the uniformity, the homogenizer has been positioned much closer to the solar cell. This operation was aimed at reducing the outgoing of irradiation from the border between homogenizer and the cell. Another main improvement introduced in the second prototype is related to the choice of the concentrator triple junction solar cell. A triple junction solar cell provided by EMCORE, with an active area of 10 mm x 10 mm and optimized for highest performance at 1000 suns, has been used. The nominal efficiency in standard condition (25°C, AM1.5, 1000 W/m^2) is 37%. A further critical issue was represented by high

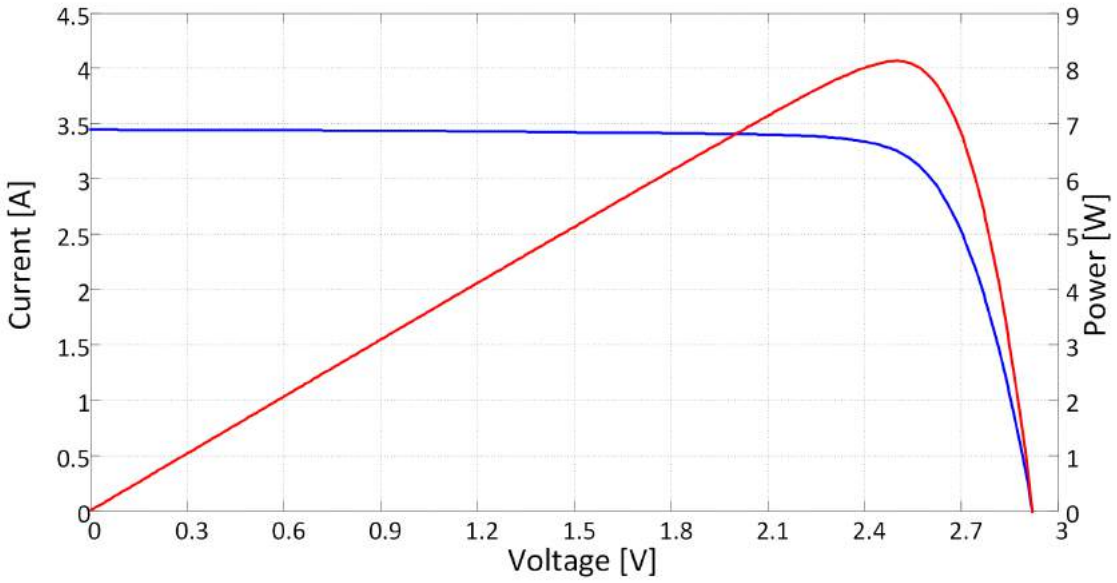

Figure 2.4.11: I-V (blue line) and Power curve (red line) of a single receiver of the CPV module.

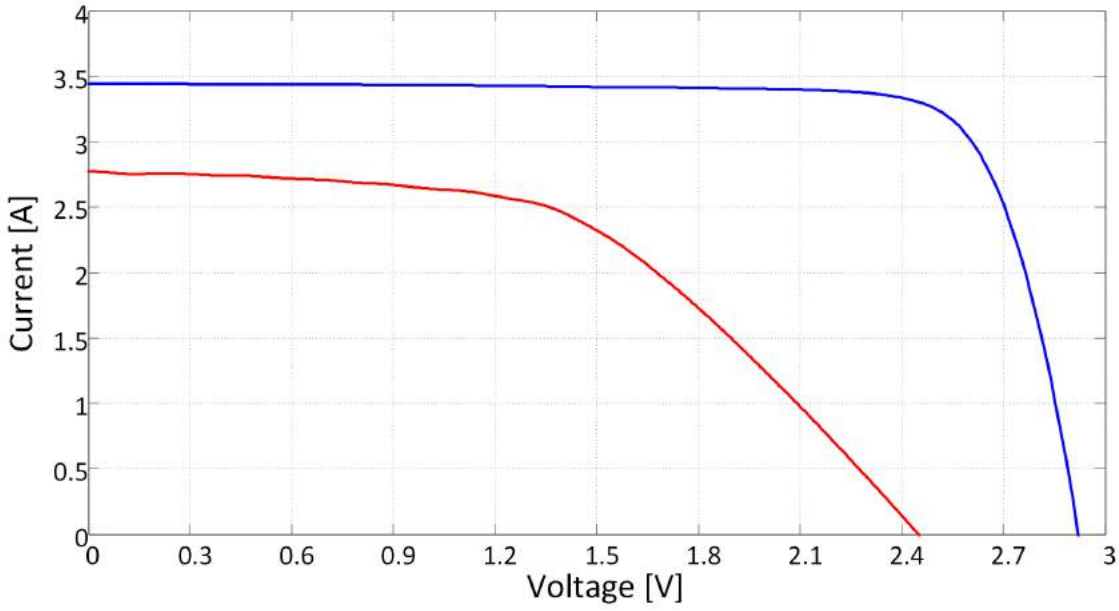

Figure 2.4.12: I-V characteristics of the single CPV cells in the new (blue) and the previous (red) module versions.

Table 2.4.2: Characterization results of the CPV prototypes

Parameter	Unit	1ST	2ST
DNI	W/m^2	870	910
I_{sc}	A	2.77	3.45
V_{OC}	V	2.45	2.92
P_m	W	3.48	8.13
FF	-	0.51	0.81
η_{mod}	%	10	22.4

cell temperatures, which in the first prototype affected negatively the performances. In order to optimize heat dissipation, a highly thermally conductive material has been applied between the back surface of each cell and the rear panel. Moreover, to reduce the high value of shunt and series resistances, which contribute to lower the values of efficiency and *FF*, a special attention has been given to the realization of the electrical connections. All other components have remained unchanged with respect to the first prototype.

2.4.7 Final Version

In this section the characterization performed on the second prototype is presented. Both single receivers and the whole module have been electrically characterized. The I-V and P-V characteristics of a single CPV receiver are reported in Fig. 2.4.11. The I-V curve presents a *FF* of 0.80 and the efficiency is 22.4%. In Fig. 2.4.12, the I-V characteristics of single concentrator receivers of both prototypes are reported. The electrical parameters are summarized in Table 2.4.2. The characterization results show that the efficiency of the single CPV receiver is more than doubled respect to that of the first prototype and that the FF increased from 0.51 up to 0.80. Moreover, from the observation of the profiles, a remarkable increase in the I-V curve slope can be observed. The slope of the I-V curves is strictly related to the value of series

Table 2.4.3: Electrical parameters registered for single CPV receivers

Parameter	Unit	1	2	3	4
DNI	W/m^2	910	910	905	910
I_{sc}	A	3.45	3.26	3.32	3.31
V_{OC}	V	2.92	2.90	2.92	2.90
P_m	W	8.13	7.72	8.08	7.98
FF	-	0.81	0.82	0.83	0.83
η_{mod}	%	22.4	21.2	22.3	21.9

resistance: the lower the series resistance the higher the slope of the curve. Following these considerations, the profile of the I-V characteristic, with its nearly vertical slope, demonstrates that the problems correlated to the inaccurate solders, responsible for the high series resistance of the first prototype, have been almost solved. In Table 2.4.3, the characterization results of each receiver are summarized together with *DNI* values. For all CPV receivers similar electrical parameters have been recorded, which proves a good alignment among them, as well as a correct position between POEs and SOEs. Special attention has been given to the cell temperature that has been monitored during all the measurements. Cells temperature showed to be almost stable during all measurements and, moreover, never exceeded the value of 45°C. This demonstrates that the heat dissipation has been further improved respect to the first prototype, where in the best case an increase of temperature from 30°C up to 67°C has been observed over a time window of six minutes, as shown in Fig. 2.4.10. The improvement on heat dissipation is confirmed by the temperature profile measured on a single receiver and reported in Fig. 2.4.14. As can be observed from the figure, the cell temperature raised by only 10°C in ten minutes. After having tested the single receivers, the behavior of the whole module has been analyzed. In particular, different possible combinations of parallel and serial connections between CPV cells have been tested to identify the best configuration giving the maximum power output. Both simple serial connection of the four receivers and different com-

Table 2.4.4: Electrical and ambient parameters registered for serial connection and best configuration in the second prototype

Parameter	Unit	(1//4)-(2//3)	1-2-3-4
DNI	W/m^2	890	900
$T_{external}$	^0C	25.7	27.9
I_{sc}	A	6.27	3.42
V_{OC}	V	5.91	9.74
P_m	W	29.72	23.7
FF	-	0.8	0.71
η_{mod}	%	21	16.4

binations of parallel and serial connections have been tested. The experimental data have shown that the most efficient configuration is a combination between parallel and serial connections of CPV receivers instead of a pure serial connection. The parallel connection has been indicated with "//" and the serial one with "-". Following this norm, the simple serial connection is indicated by "1-2-3-4", while the most performing configuration has been given by "(1//4)-(2//3)". In the most performing configuration with a DNI value of 890 W/m^2 a P_m of 29.72 W has been recorded, while the calculated FF and efficiency have been 0.80 and 21.0%, respectively.

The results of the measurements for the best configuration are compared in Table 2.4.4 with the results for a simple serial connection of the four CPV receivers (1-2-3-4). By combining serial and parallel connections an increase of P_m, FF and efficiency of 25.40%, 12.65% and 27.7% respectively has been obtained when compared to the values measured in the simple serial connection. Higher performances can be ascribed to a better compensation of mismatch losses. Such compensation

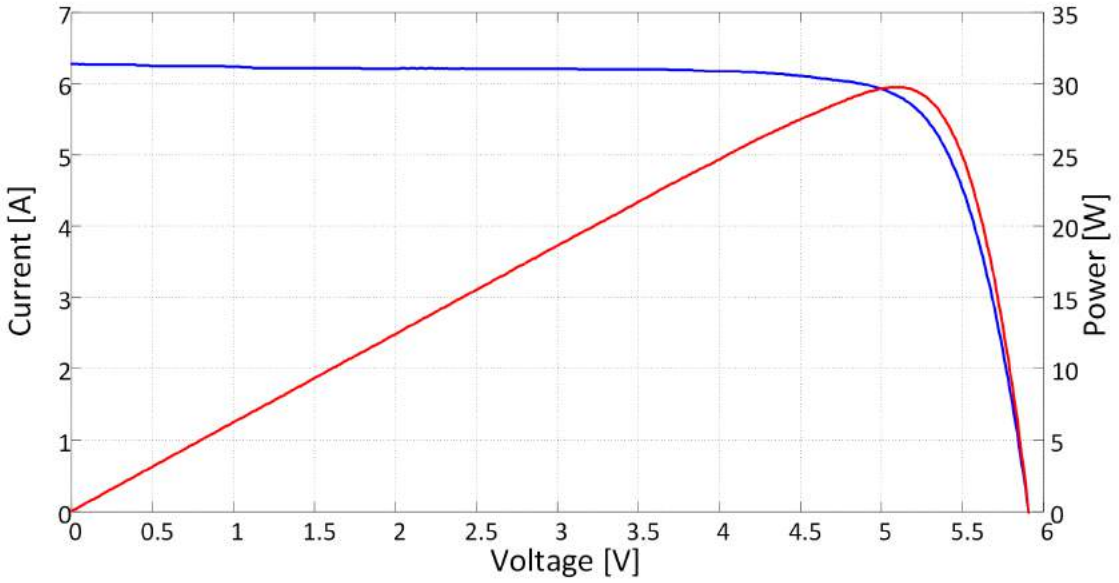

Figure 2.4.13: I-V (blue line) and P-V curves (red line) obtained for the most efficient CPV module configuration: (1//4)-(2//3).

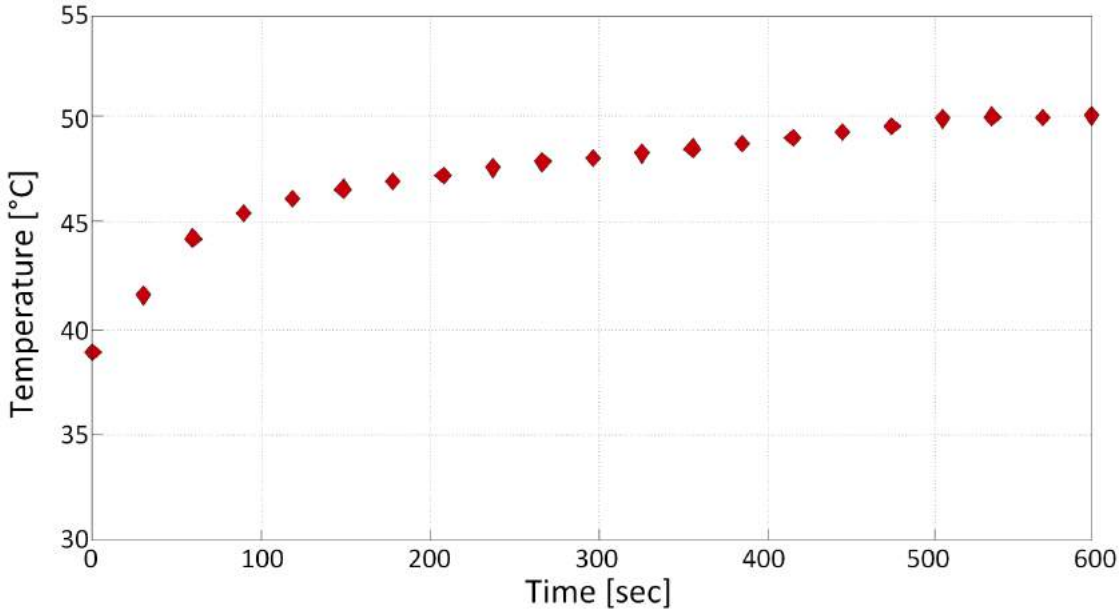

Figure 2.4.14: Single receiver temperature vs time.

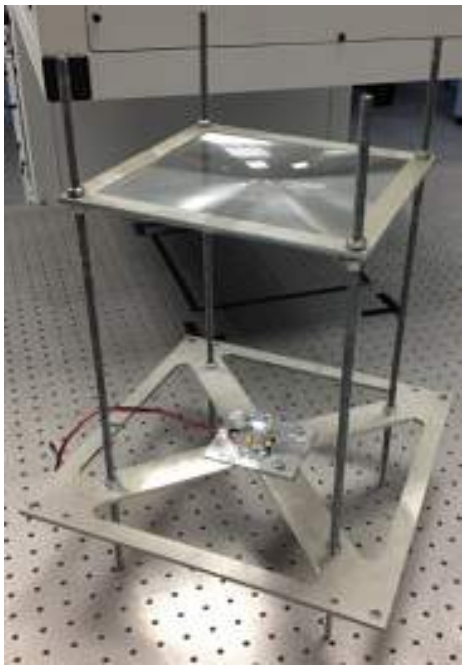

Figure 2.4.15: System used for thermographic acquisition.

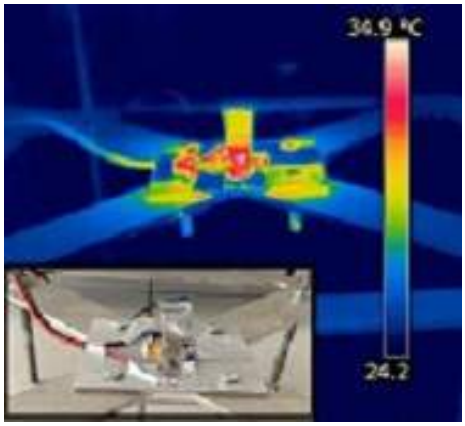

Figure 2.4.16: Thermographic image of the triple junction cell with homogenizer under the simulated solar light, concentrated with the Fresnel lens. In the inset the corresponding digital image is shown.

Table 2.4.5: Electrical parameters registered for the two prototypes

Parameter	Unit	(1-2-3-4)(1^{ST})	(1-2-3-4)(2^{ST})	(1//4)-(2//3)(2^{ST})
DNI	W/m^2	880	900	890
I_{sc}	A	2.61	3.42	6.27
V_{OC}	V	10.14	9.74	5.91
P_m	W	14.39	23.7	29.72
FF	-	0.54	0.71	0.8
η_{mod}	%	10.2	16.4	21

effect does not occur for the pure serial connection, where the current of the whole system cannot exceed the current value of the worst cell. The combination of parallel and serial connections minimizes the losses, giving a better final result. Fig.2.4.13 shows I-V and P-V curves obtained with the best configuration. In Table 2.4.5 the electrical parameters measured on the two prototypes are summarized in order to better highlight the achieved improvements. If for both prototypes the serial connections of the four CPV receivers are considered, an increase of 65% for the P_m, 32% for the FF and 61% for the efficiency have been recorded. These improvements are even better when the best configuration individuated for the second prototype is considered. In that case the FF increases by about 50% while P_m and efficiency are more than doubled. In order to deeper analyze the heating effects occurring inside the CPV module, the thermal behavior of the single CPV receiver has been analyzed by means of thermographic measurement. The analysis has been carried out with the FLIR T360 IR camera under the Abet Sun 2000 Solar Simulator. The structure used for thermographic analysis comprises a triple junction cell, a homogenizer and a Fresnel lens, as shown in Fig. 2.4.15. It allows to easily take the IR images of the photoactive area, since there is a direct access to the triple junction cell. The structure has been irradiated with the solar simulator for three minutes and after that infrared images of the photovoltaic receiver have been acquired in open circuit conditions. This procedure allowed to observe the temperature distribution in the

triple junction cell and to determine the areas with the highest temperature. In Fig. 2.4.16 the thermographic acquisition together with the corresponding digital image is reported. The image shows that one of the areas with highest temperatures is located on the bottom of the homogenizer close to the cell surface. This result confirms a good functioning of the concentration system together with the correct alignment between POE and SOE, since the highest radiation density is located in the zone of the photovoltaic cell.

2.5 Reflective Optic

The reflective optic based systems are characterized by higher complexity than the refractive ones. This can be ascribed to the double reflection which occurs in these systems, typically composed of a mirror as a primary optical element and a reflector as the secondary one. These systems are not affected by chromatic aberrations, but an excellent optical alignment is a mandatory requirement. In the framework of the collaboration between the University of Cagliari, Sardegna Ricerche and the University of Ferrara, a novel configuration of a Cassegrain-type CPV module prototype developed by the Physics Department of the University of Ferrara has been installed and tested at the Sardegna Ricerche Photovoltaic Laboratory. In this study an accurate outdoor characterization of a single receiver of the developed CPV prototype is proposed and described in detail and several results are presented for the main important electrical parameters [52].

2.5.1 Module Description

In this subsection a concentrating photovoltaic system that uses a modified architecture "Cassegrain-type" is presented. As reported in [53], it is characterized by a photovoltaic receiver back placed to the primary collector. In order to minimize any loss of efficiency due to an imperfect alignment with the primary collector, the concentrator optic is equipped with a secondary reflector characterized by a low radius of curvature. The total track of the system is approximately 10 cm, and the individual modules are designed so that they can be packed with each other in an efficient manner, in order to make the most of the collecting area of the module.

Figure 2.5.1: Triple-junction cell mounted on the IMS support [53].

Panel base dimensions for the system composed by a 2x2 receivers array, are 42x42 cm^2. The main collector is a molded part in polycarbonate realized by injection and subsequently protected by PVD metallization with enhanced aluminum, covered with a protective layer of silicon oxide. The secondary reflector is a convex mirror of optical glass BK-7, with a diameter of 50 mm and a thickness of 10 mm, with a coating of aluminum and silicon oxide. The system is optimized so that the acceptance angle is at least $\pm$ 0.5° for 90% of the nominal power [53]. The module is provided with 4 triple-junction cells (Ge/InGaAs/InGaP) with very high efficiency (>30%) welded with proprietary technology on substrates with high thermal conductivity (1.4 W/m*K). The support of the cells is realized in IMS (Insulated Metal Substrate). The cell with its support can be observed in Fig. 2.5.1. The four receivers are also equipped with rectangular pipe homogenizers made with Alanod MIRO high reflective 95. The system is enclosed in a structure made of PMMA and closed frontally by a tempered ultra-clear glass for photovoltaics. The schematic structure of a single receiver has been reported in Fig. 2.5.2 [53]. Based on nominal data of multijunction cells, it is possible to estimate the efficiency expected from the system in 20%, calculated at 850 W/m^2 of *DNI*. The rated power output for this value of irradiance is about 30 W. An eventual power loss may be caused by possible

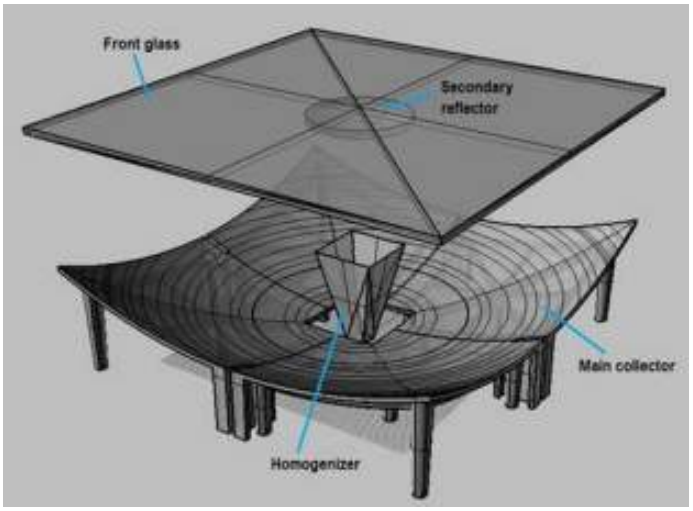

Figure 2.5.2: CPV receiver structure [53].

Figure 2.5.3: Proposed CPV module during outdoor characterization.

Table 2.5.1: Solar cell performance under a solar simulator and under the natural sunlight

	I_{sc}[A]	V_{OC}[V]	P_{mpp}[W]	η_{mod}[%]	GNI[W/M^2]
Solar cell under solar simulator	0.58	2.95	1.6	4.98	1000
					DNI[W/M^2]
Solar cell under natural sunlight	2.57	2.97	6.59	21.78	942.28

misalignment errors of a cell compared to the others. In the Fig. 2.5.3 the final CPV panel, mounted on a solar tracker, can be noticed.

2.5.2 Indoor and Outdoor Characterization

The outdoor characterization of a CPV device is an essential step in the evaluation of its performance under real operative conditions. Nevertheless outdoor measurements are very complex and affected by environmental variations. For these reasons, indoor tests, which allow to carry out repeatable measurements under controlled environmental conditions, are fundamental in the rating process of CPV modules [29]. Solar simulators, used for CPV and PV indoor tests, are classified in accordance with the IEC 60904-9 standard [54] which takes into account the following three aspects: spectral distribution match, irradiance non-uniformity on the test plane and temporal instability. In accordance with this standard, a simulator with the best performance is classified as an AAA simulator. It is worth noting that the methodology proposed in [54] has been defined considering only conventional crystalline and thin film modules. Consequently, an AAA solar simulator could not be suitable for the indoor characterization of CPV systems which require other important technical specifications in terms of optical and radiometric properties. Common solar simulators can be also classified on the basis of the operating state, i.e. continuous- and pulse-state. Although pulse-state solar simulators are commonly employed in the CPV indoor characterization, they cannot be used to reproduce the thermal

effects on the cell surface caused by a prolonged exposure at the natural sunlight. Considering the importance of this phenomenon on the performance of a CPV receiver, the possibility to use a continuous sun simulator for indoor characterization has been investigated. As a consequence, the indoor tests have been performed by means a continuous-state solar simulator, classified as ACA in accordance with [54]. However, the results presented in Table 2.5.1 show the unreliability of this indoor test. In fact, it is important to notice that further conditions than those defined in [54] should be taken into account to perform a correct and accurate indoor characterization of a CPV system. First of all, the light source should have an angular divergence close to that of the direct sunlight (about $\pm$ 0.266°) or at least close to the acceptance angle of the CPV module under test (usually between 0.5° and 1°) [55]. The angular divergence of the solar simulator involved in the presented indoor tests has been measured by Akkutrack, a high resolution instrument [56] and is equal to about 1.5°, which is very far from the angular divergence of the sun. A CCD camera has been then used to analyze the simulator spot image and to verify the solar simulator rating result in the spatial uniformity category. The outcomes have shown that the irradiance distribution on the test plane is characterized by a so high non-uniformity that produces heavy hot-spot phenomena on cell surface. These two critical factors introduce high energy losses and also increase the module degradation [34],[57]. In order to verify the energy losses associated to the angular divergence and spatial uniformity characteristics of the used solar simulator, a comparison between the electrical parameters of the tested CPV receiver acquired indoor and outdoor has been performed. The numerical results are summarized in Table 2.5.1, showing the poor performance of the CPV receiver under the aforementioned solar simulator. For these reasons, the indoor characterization of CPV devices, performed by the continuous-state solar simulator used for this study, cannot be considered reliable.

The outdoor characterization has been performed in Sardinia at the Sardegna Ricerche outdoor facility. The I-V curves have been measured by using a power source-meter (Keithley2651A) controlled by a software written in the LabView programming language, as reported in Section 2.4.2. Similarly, the environmental parameters, such as *GNI*, *DNI*, the ambient temperature, the wind speed and the relative humidity, have been acquired by a National Instruments acquisition plat-

Table 2.5.2: CPV prototype electrical parameters

	I_{sc}[A]	V_{OC}[V]	P_{mpp}[W]	η_{mod}[%]	FF[-]	DNI[W/M^2]
11:06am	1.93	2.97	4.99	21.56	0.847	706.03
11:06am	2.62	2.957	6.62	21.77	0.852	947.2
11:06am	2.75	2.957	6.94	22.29	0.852	969.36

form by means of appropriate sensors and automatically elaborated and stored. In Fig. 2.4.3 the graphical user interfaces (GUIs) is shown. Thanks to this configuration, the electrical and environmental parameters could be acquired simultaneously. Moreover, a high-precision dual-axis tracker has been employed, as reported in Section 2.4.2. The solar tracker used to test the CPV receiver is the same employed in the first prototype characterization (Section 2.4.2) [53]. The receiver cell temperature has been measured by a PT100 probe that has been placed on the back of the module, as near as possible to the solar cell. In accordance with [58], the back side receiver temperature can be considered 8°C smaller than the cell one. Thus, in order to define the performance of the CPV receiver, a complete outdoor characterization has been performed on 22st March 2013. The results reported in Fig. 2.5.4 refer to different values of DNI and cell temperature. It is worth noting that V_{OC} decreases slightly as cell temperature raises, while I_{sc} increases from 1.93 to 2.75 A, in correspondence to a DNI gain of 260 W/m^2. Although the cell temperature also increases (by about 6.5°C) in the same measurement interval, it is evident that I_{sc} trend is much more influenced by the DNI growth. The electrical parameters are reported in Table 2.5.2. In accordance with [53] and as previously reported, the CPV receiver efficiency has been determined by (2.7):

$$\lambda_{\text{cell}} = \frac{P_m}{DNI * A_{\text{LENS}}} \tag{2.7}$$

in which P_m is the maximum output power and DNI is the irradiance on the primary optic surface (A_{LENS}). The evolution of the efficiency versus the DNI is shown in Fig. 2.5.5. It can be seen that the efficiency trend is linear, meaning that

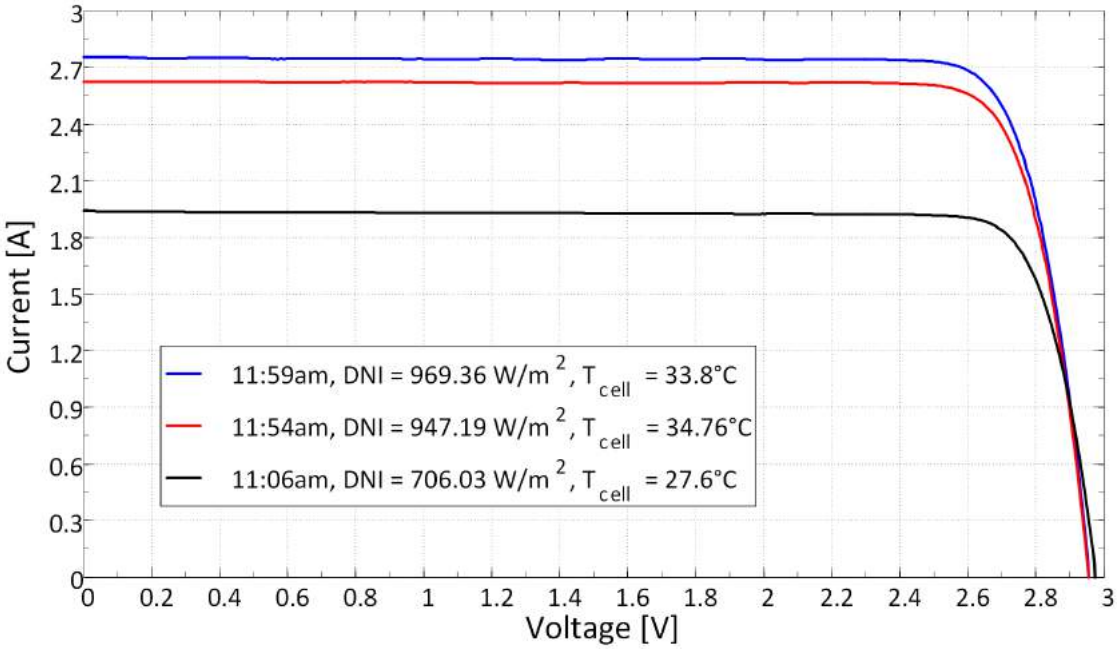

Figure 2.5.4: I-V characteristics under different values of irradiance and cell temperature.

the irradiance has not yet reach the value for which the efficiency starts to reduce, as pointed out in [39]-[50]. It is important to notice that the receiver efficiency is also affected by the temperature. In fact, as the cell temperature increases, λ_{cell} decreases, as shown in Fig. 2.5.6. However, the cell temperature affects the efficiency less than the *DNI*. Fig. 2.5.7 depicts the linear relationship between the output power and the *DNI*. Moreover the wind speed influence on efficiency has been also evaluated, as reported in Fig. 2.5.8, where no clear relationship between the efficiency and the wind speed can be observed. This result confirms the conclusions reported in [53].

Afterwards, the CPV receiver performance has been evaluated both in a sunny day and in a cloudy day. In the first case, the output power is almost constant with

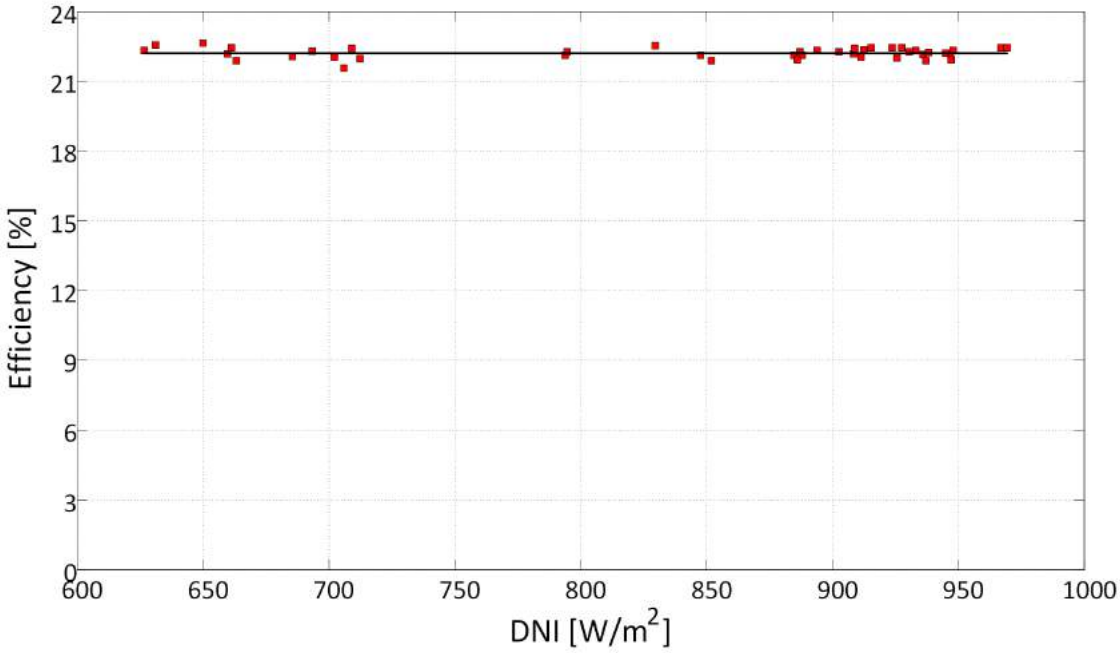

Figure 2.5.5: DNI influence on CPV receiver performance.

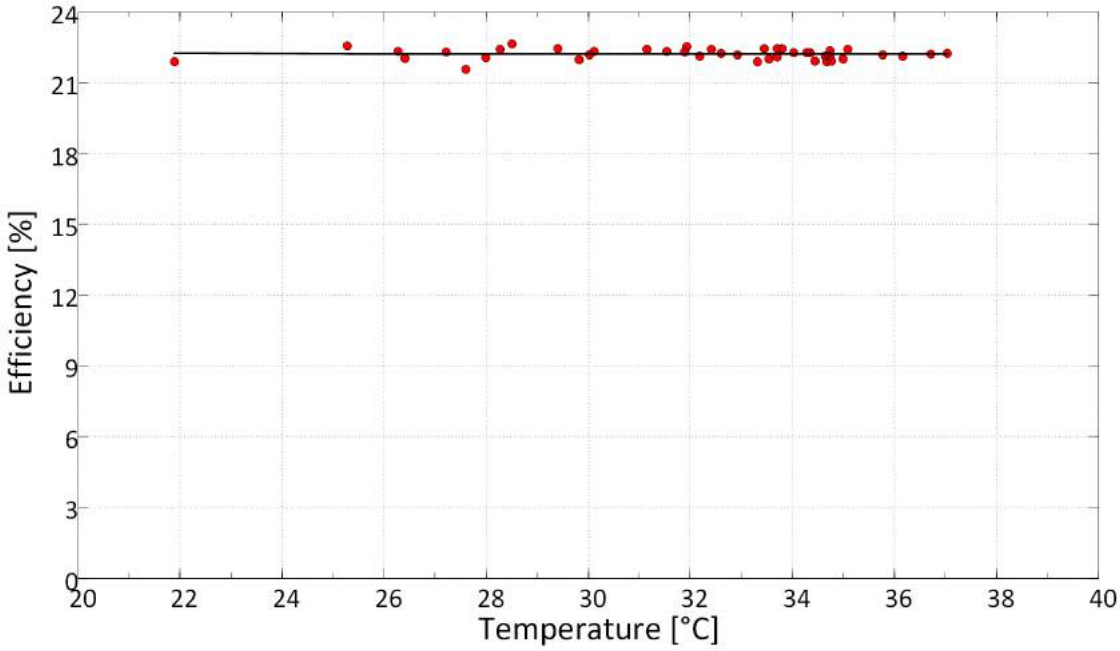

Figure 2.5.6: Cell temperature influence on CPV receiver performance.

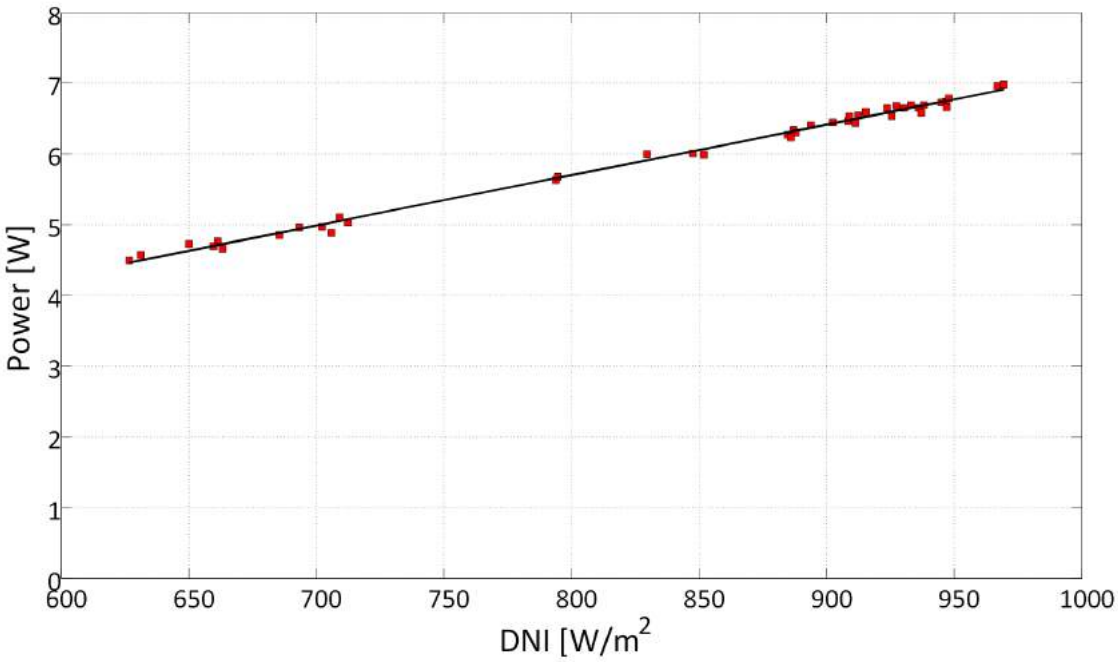

Figure 2.5.7: DNI influence on CPV receiver max output power.

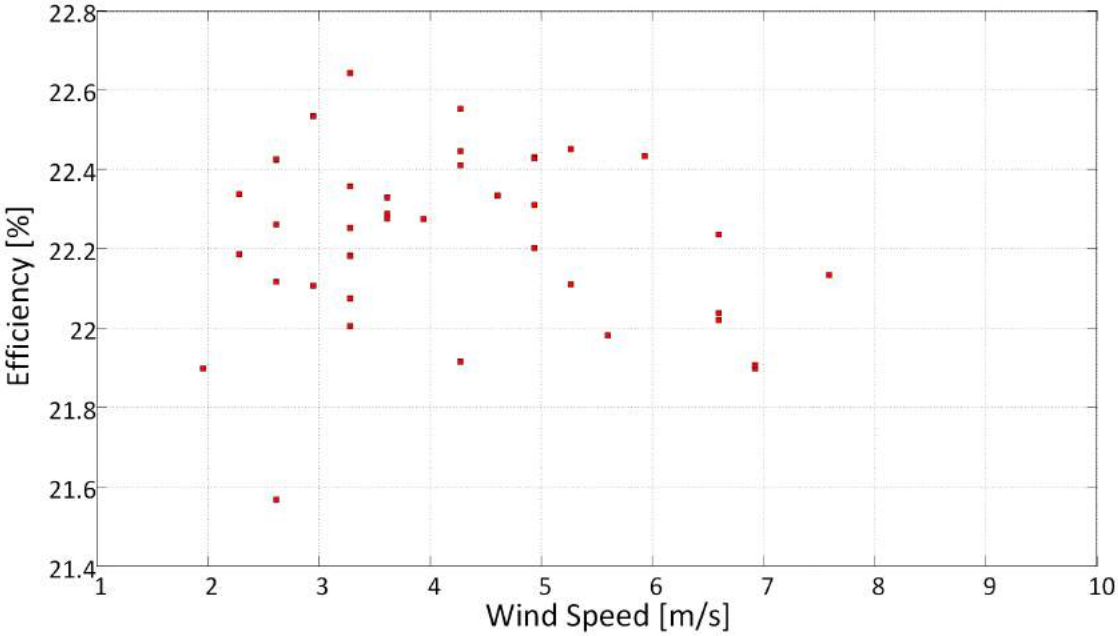

Figure 2.5.8: Wind speed and CPV receiver efficiency.

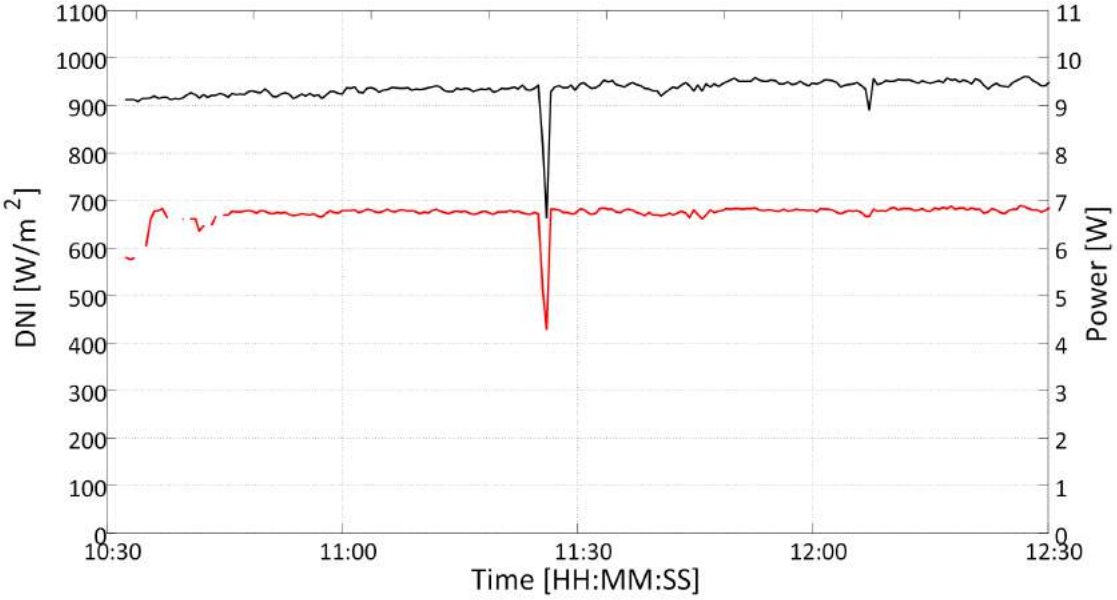

Figure 2.5.9: DNI and max output power on a sunny day.

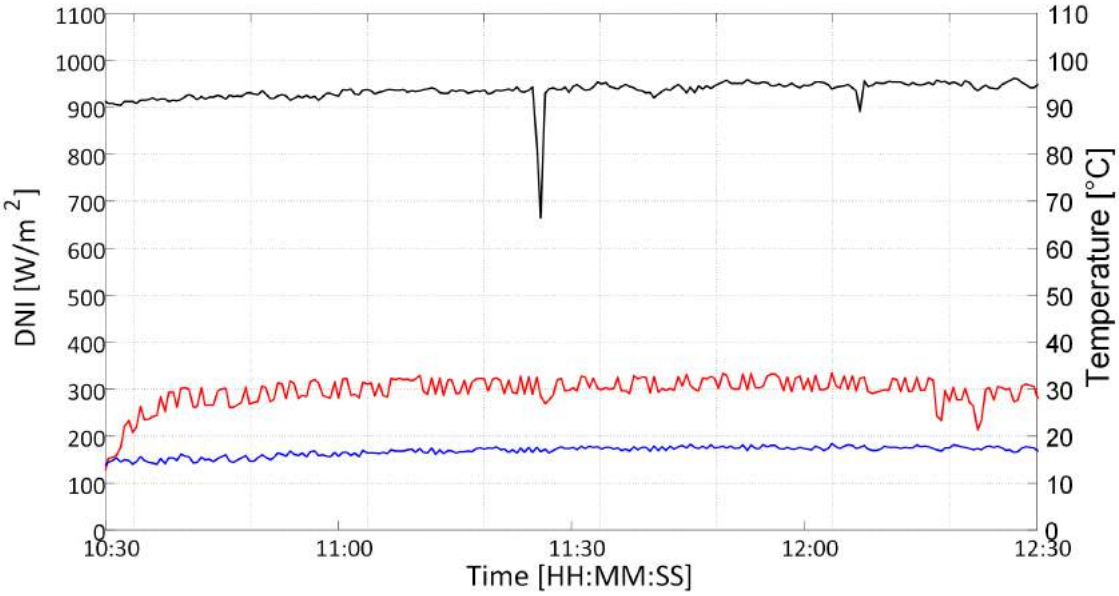

Figure 2.5.10: DNI, cell and ambient temperature and trend on a sunny day.

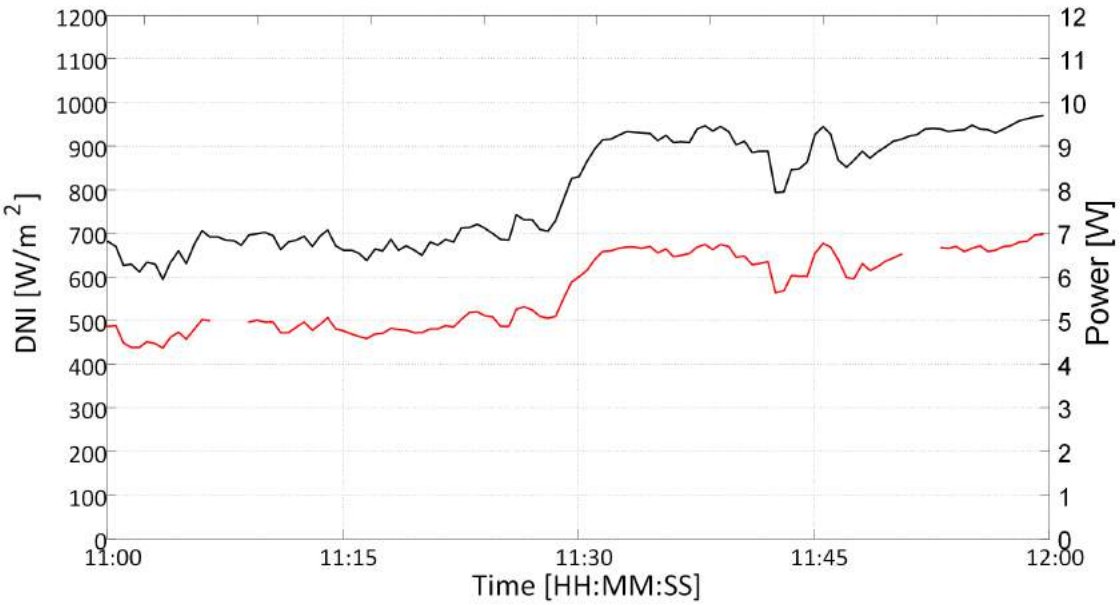

Figure 2.5.11: DNI and max output power on a cloudy day.

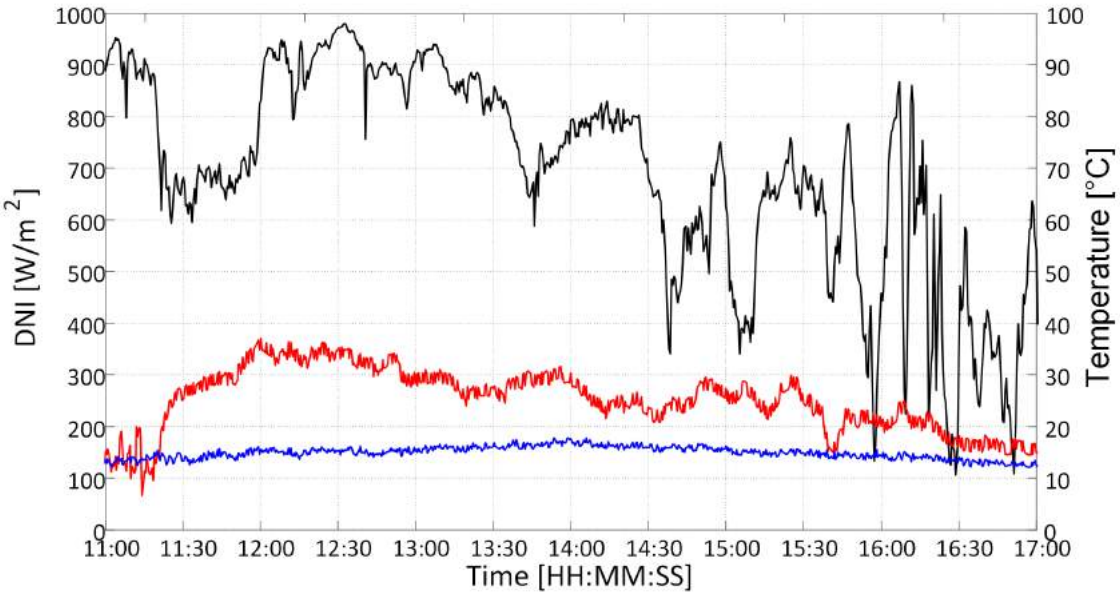

Figure 2.5.12: DNI, cell temperature and wind speed trend on a cloudy day.

a time evolution similar to that of *DNI*, as depicted in Fig. 2.5.9. Furthermore, during the measurement interval, the difference between the cell and the ambient temperature remains almost constant (14°–18°C) as reported in Fig. 2.5.10. In the second case, shown in Fig. 2.5.11 and 2.5.12, the weather variability has caused an irregular trend for all the considered parameters. In particular, the output power and the cell temperature rapidly raise and decrease depending on DNI variations. This variable operating condition significantly stresses the solar cell, more than the case of a sunny day.

2.5.3 Issues in conversion to standard conditions

Once the I-V characteristics have been measured and acquired, they should be reported under CSTC. When this study has been developed, an international procedure that defines standard test conditions for CPV systems was not available. In fact, the CPV standard, i.e. the IEC 62108 [37], only specified the essential mechanical, electrical and thermal requirements for CPV systems. The IEC TC 82 was developing a new standard, published at the end of 2013 as IEC 62670-1 [35]. This standard defines CSTC as: DNI =1000 W/m^2, $T_{cell} = 25$°C and *AM1.5d*. Nevertheless, before the publication of the IEC 62670, the Italian standard CEI 82-25 [31] had defined in 2011 the following CSTC, $DNI = 850$ W/m^2, $T_{cell} = 25$°C, *AM1.5d*, for determining the nominal power of a CPV module. In accordance with the procedure of the IEC 60891 standard [59], the I-V characteristics of the tested CPV receiver have been reported under these conditions, in order to accurately compare the receiver performances under different DNI conditions. The equations used to correct the I-V data set are the following:

$$I_2 = I_1 + I_{sc} * (\frac{G_2}{G_1} - 1) + \alpha * (T_2 - T_1) \tag{2.8}$$

$$V_2 = V_1 - R_s * (I_2 - I_1) - K * I_2 * (T_2 - T_1) + \beta * (T_2 - T_1) \tag{2.9}$$

where I_1, V_1, I_2 and V_2 represent a point of the measured and corrected I-V characteristics, respectively; α and β are the current and voltage temperature coefficients; G_1 is the measured irradiance and G_2 is the standard irradiance (in this

case 850 W/m^2). Finally, R_s is the internal series resistance of the module and k is the curve correction factor. By applying the methodology proposed in [59], the curve correction factor k has been determined to be equal to 0. Consequently, the correction equations assume the following simplified forms:

$$I_2 = I_1 + I_{\mathrm{sc}} * (\frac{G_2}{G_1} - 1) + \alpha * (T_2 - T_1) \tag{2.10}$$

$$V_2 = V_1 - R_{\mathrm{s}} * (I_2 - I_1) + \beta * (T_2 - T_1) \tag{2.11}$$

The series resistance is a parameter that could greatly affect cell performance, as reported in [60]. Consequently, its value has been determined using the procedure proposed in the IEC 60891. In accordance with this standard, several I-V curves under different values of irradiance with a constant cell temperature have been acquired. The voltage and current values have been adjusted using (2.10) and (2.11) and assuming R_s=0. Subsequently, the R_s has been modified by steps of 10 mΩ, until an almost perfect matching of I-V curves have been achieved in correspondence of a series resistance of about 50 mΩ. The current and voltage temperature coefficients have been also determined from [59]. The IEC 60891 standard requires to acquire at least four I-V curves at different cell temperatures. As a result, the employment of this procedure leads to CPV receiver current and voltage temperature coefficients of 7.3 mA/^{0}C and -0.2 mV/^{0}C, respectively. In Table 2.5.3, the measured and adjusted (according to the CSTC of the CEI 82-25) electrical parameters of three I-V characteristics have been reported. Afterwards, the current and power adjusted values have been compared to ones measured (P_m of 6.015 W and I_{sc} of 2.364 A) under environmental conditions close to the CSTC (DNI of 847.68 W/m^2, ambient temperature of 15.66°C, wind speed of 2.95 m/s). These current and power values have been considered as the reference parameters in the definition of current and power deviations (D_{Isc} and D_{Pm}), evaluated as follows:

$$D_{\mathrm{Isc}} = \frac{I_{\mathrm{sccor}} - I_{\mathrm{scref}}}{I_{\mathrm{scref}}} \tag{2.12}$$

$$D_{\mathrm{Pm}} = \frac{P_{\mathrm{mcor}} - P_{\mathrm{mref}}}{P_{\mathrm{mref}}} \tag{2.13}$$

Table 2.5.3: Corrected electrical parameters of CPV receiver

	I_{sc} [A]	D_{ISC} [%]	V_{OC} [V]	P_m [W]	D_{PM} [%]
$I-V$ $charact.on$ $11:01am$ $(T_{\mathrm{cell}} = 26.43^0C, DNI = 627.86W/m^2)$	1.69		2.97	4.38	
$I-V$ $charact.on$ $11:25am$ $(T_{\mathrm{cell}} = 25^0C, DNI = 850W/m^2)$	2.28	-3.5	2.95	5.89	-2.1
$I-V$ $charact.on$ $11:25am$ $(T_{\mathrm{cell}} = 50^0C, DNI = 850W/m^2)$	2.46	4.1	2.94	6.32	5.5
$I-V$ $charact.on$ $11:41am$ $(T_{\mathrm{cell}} = 34.4^0C, DNI = 887.4W/m^2)$	2.51		2.95	6.34	
$I-V$ $charact.on$ $11:41am$ $(T_{\mathrm{cell}} = 25^0C, DNI = 850W/m^2)$	2.33	-1.4	2.95	5.91	-1.7
$I-V$ $charact.on$ $11:41am$ $(T_{\mathrm{cell}} = 50^0C, DNI = 850W/m^2)$	2.51	6.1	2.95	6.35	5.5
$I-V$ $charact.on$ $11:54am$ $(T_{\mathrm{cell}} = 33.54^0C, DNI = 937.38W/m^2)$	2.59		2.95	6.58	
$I-V$ $charact.on$ $11:54am$ $(T_{\mathrm{cell}} = 25^0C, DNI = 850W/m^2)$	2.29	-3.1	2.95	5.82	-3.2
$I-V$ $charact.on$ $11:54am$ $(T_{\mathrm{cell}} = 50^0C, DNI = 850W/m^2)$	2.47	4.4	2.95	6.27	4.2

where I_{sccor} is the adjusted current value and I_{scref} is the value measured under conditions close to the CSTC. Similarly, P_{mcor} and P_{mref} are the adjusted and measured maximum output power values, respectively. The results show that as more the test conditions are far from CSTC, in particular regarding DNI, as more there is a significant deviation on corrected current and maximum power values, as pointed out by D_{Isc} and D_{Pm} quantities reported in Table 2.5.3. In order to analyze the effect of the cell temperature on D_{Isc} and D_{Pm} deviations, a comparison between the adjusted values calculated at 25°C and at a more realistic cell temperature of 50°C has been developed. The results are reported in Table 2.5.3. In particular,

Table 2.5.4: ASTM 2527 - Standard Test Conditions

Parameters	Standard Test Conditions	Rejection Conditions
Ambient Temperature	$20°C$	-
DNI	$850W/m^2$	$-DNI < 750W/m^2$ – changes more than 10% from the maximum value to the minimum value recorded during any 10 min interval
Wind speed	$4\ \frac{m}{s}$	– v $> 8\ \frac{m}{s}$ – if v exceeds 15 $\frac{m}{s}$, reject alla data during the succeeding 10 min interval

the highest deviations of the reported current and power values (for a *DNI* value close to the one of the CSTC) have been obtained considering the highest reporting cell temperature. The reported values at 25°C well fit the measured values only if the environmental conditions are close to that defined in the CSTC and show a significant mismatching for higher and lower *DNI*. Therefore, being the cell temperature a parameter strictly connected to the mechanical and optical properties of the CPV receiver (such as the optic concentrator structure, the used solar cell, the concentration factor and the module cooling system), the introduction of the solar cell temperature in the CPV qualification and test methods makes the definition of the rated CPV performance very difficult. The determination of the CPV receiver absolute power at standard conditions has been carried out in accordance with the ASTM E2527 standard [61]. The environmental conditions and the data restrictions reported in [61] are summarized in Table 2.5.4. The output power is defined by (2.14), as reported in [61].

$$P = E * (a_1 + a_2 * E + a_3 * T_{\text{amb}} + a_4 * \upsilon) \tag{2.14}$$

In (2.14) the relationship between the output power and the environmental parameters, such as *DNI* (E), ambient temperature (T_{amb}) and wind speed (υ), can be observed. The coefficients a_1, a_2, a_3 and a_4 have been calculated through a linear regression of the measured parameters E, T_{amb} and υ. Then, the absolute output power at standard reporting conditions has been determined by (2.15):

$$P = E_0 * (a_1 + a_2 * E_0 + a_3 * T_0 + a_4 * \upsilon_0) \tag{2.15}$$

The experimental results show a P_0 equal to 6.028 W. This value has been used in (2.13) to evaluate the power deviation from the reference power of 6.015 W. The result shows a power deviation equal to 0.21%, while the lowest deviation obtained by applying the IEC 60891 is 1.7%. Therefore, by adopting the ASTM standard, a very high accuracy can be reached in reporting the CPV receiver power under the standard conditions. This better result could be explained by the fact that the ASTM standard takes into account the ambient temperature instead of the cell one. In this way, it is possible to evaluate only the relationship between the environmental parameters and the output power, without considering the peculiar structure of the CPV system (presence of passive/active cooling, refractive/reflexive optics, etc.).

2.6 The role of CPV systems in MGs

The progressive growth of air pollution and climate change effects have led to the adoption of increasingly strict environmental and energy policies worldwide. Moreover, many international governments push to differentiate their primary energy supply by significantly supporting the exploitation of Renewable Energy Sources (RESs). In particular, PV systems are characterized in the last years by a large employment around the world. Altought the PV plants cleaness and sustainability, they are also poorly predictable, due to their relevant dependence on the environmental

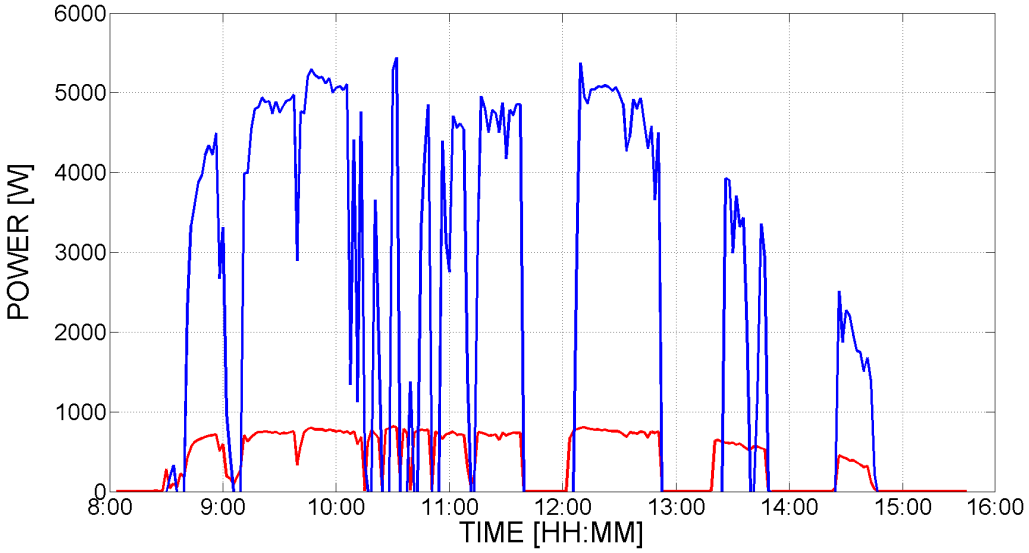

Figure 2.6.1: An example of power variations (red line) from CPV plant.

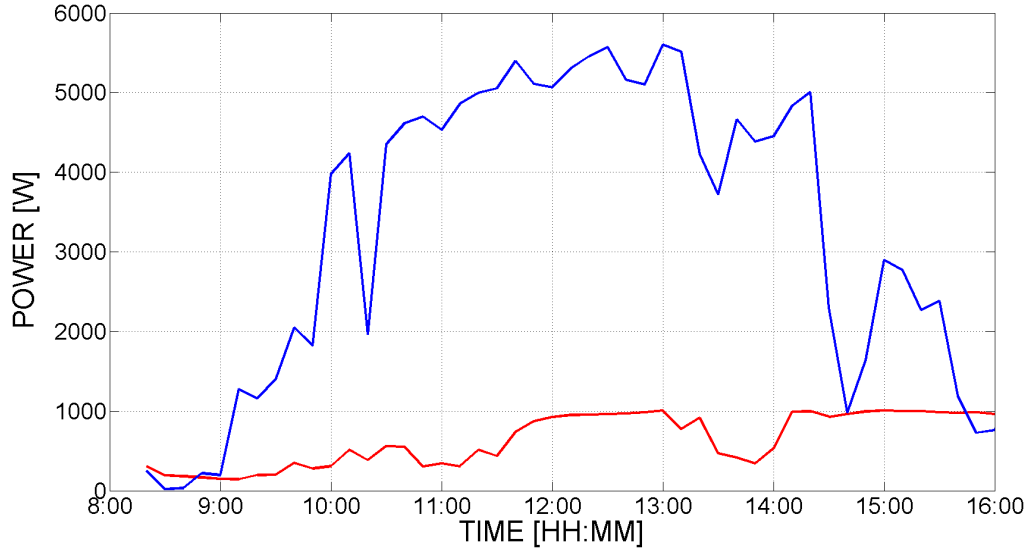

Figure 2.6.2: An example of power variations (red line) from traditional PV plant.

parameters, such as irradiance, temperature and wind speed [62]-[4]. Nevertheless, if PV traditional plants depend on the Global Normal Irradiance (GNI) and consequently their power production doesn't decrease to zero even if GNI reduces during a cloudy day (Fig. 2.6.2), the CPV ones depend on the direct component of the GNI, that is the DNI (Direct Normal Irradiance). Thus, during a cloudy day, the power production of a CPV plant is equal to zero when DNI decrease to the same value, as reported in Fig. 2.6.1. It is worth noting that the energy management of a CPV plant inside a MG is more difficult than of a traditional flat-plate PV one. The above characterization processes are fundamental to predict the CPV systems power production both in sunny and in cloudy days. In particular, the knowledge of the issues related to the CPV technology allows to develop a suitable management strategies, in order to guarantee the reliability and the controllability of the MG. On the basis of these considerations, the RESs and particularly CPV plants represent a challenge for the management of a MG because of their poor predictablity and the requirement of power inverters [62]. In order to overcome the power production limits of CPV plants, they are combined inside the MG with energy storage systems (ESSs) that allow to store the CPV surplus energy during sunny days and to supply the MG when the CPV production is poor due to adverse environmental conditions. By implementing the above solution, the MG can operate both as indipendent unit and as a support unit in order to guarantee the main grid stability [63], [64].

In 15 years, more electricity will be sold for electric vehicles than for light. (1910)

Thomas Alva Edison

3

The Electric Vehicles

At the present time, the technological leadership in the automotive market is represented by internal combustion engine vehicles (ICEV). However, their massive diffusion has led to air pollution growth especially in the cities, contributing at the same time to the global increase of greenhouse gas emission [17]. The environmental and energy policies have recognized at the mobility sector a primary role in the climate policies and have promoted its technological evolution, speeding up the transition from oil mobility to sustainable one. In particular, the international and local governments have set more severe gas emission limits in the automotive sector stimulating the introduction of drive-train electrification into vehicle propulsion systems. Indeed the plug-in hybrid electric vehicles (PHEV) are acquiring increasingly attention thanks to the industrial feasibility of reaching, at competitive cost, for passenger car the EU 2020 CO_2 emission standards [65]. This is opening new perspective and scenarios for the development of Electric Vehicle (EV). In fact, at the present time, the Battery Electric Vehicle (BEV) has initial costs higher than ICEV and PHEV caused principally by the energy storage system. However thanks to recent develop-

ments in the electrochemical sector and to the novel approach in the BEV design, in the next future a significant price decrease of this class of vehicle is expected [23]. Moreover, BEVs, thanks to: (i) their overall efficiency (60-70%); (ii) the use of renewable energy sources and (iii) the development of smart grid paradigms, represent a key component for the implementation of future power systems [66]. This is strictly connected to the employment of the electric propulsion system and due to the possibility of managing the battery vehicle as a distributed electrochemical storage system, as reported in Chapter 1 [21], [22]. Hence, the exploitation of BEVs has to be placed in a future contest in which the vehicle batteries will perform different tasks and services according, for example, to the vehicle to grid (V2G) paradigm, [19], [20], [18], [21], [22]. This requires the development of integrated control techniques able to manage both the charging infrastructure and the electric vehicle batteries satisfying firstly the mobility need. On the basis of these considerations, the EV simulation phase assumes a fundamental role in order to avoid time and cost expenditure during design and realization process and, moreover, to make the EV feedback information reliable for managing correctly and profitably an EV fleet inside a MG. Thus, an accurate model that reproduces the battery behavior under real dynamic driving conditions which is characterized by rapid speed variations is mandatory, as well as its validation in order to confirm the estimation results [65], [67], [68]. Once the model has been validated, the predictive and accurate evaluation of the final battery State Of Charge (SOC) of an EV, jointly with the information regarding the route and final destination, can support the management of the charging infrastructure. This can be developed by means of the actual "smart phone" which is characterised by high computational performance able to develop off-line predictive estimation of the final SOC, permitting, at the same time, the communication of all information required and associated to the geographic position, speed and the route thus suggesting the most suitable charging station.

In the next sections two BEV models will be presented. Both are characterized by the same powertrain tipology, wheareas the battery type considered is different. With regard to the first model, a comparison between two transmission systems (single and double gear) has been developed, in order to evaluate the most suitable configuration in terms of efficiency and SOC of the battery [69]. Concerning the

second model, a dynamic battery equivalent circuit has been defined on the basis of experimental data and then implemented in the simulation algorithm with the aim to reproduce the real behaviour of a Smart Electric Drive. Finally, the simulation data have been compared with the real ones and a good accuracy is highlighted [70].

3.1 First Model

In this section, a general approach to model an EV in Matlab environment is proposed in order to evaluate the overall vehicle performance, such as the battery consumption, the driving range, the motor parameters, etc. The performance of the proposed model has been validated referring to technical literature. Then, the analysis of the effects on the overall efficiency and vehicle performance of the transmission subsystem especially focusing on the number and values of gears has been conducted. The EV model has been developed referring to the mechanical and the electric energy balance equations. Firstly, the dynamics forces applied to the vehicle have been considered in order to determine the tractive force and power requirements. Secondly, the powertrain model has been introduced. It consists of four fundamental components: the transmission subsystem, the electric motor, the DC/AC inverter used to supply the electric motor and the DC/DC converter used as front-end between the battery and the electric drive. Finally, a dynamic model of the battery pack is proposed.

3.1.1 Vehicle Dynamics

In order to define the vehicle dynamics, the mechanical balance equations have to be introduced. In particular, with regard to general moving condition, a vehicle must counteract the following resistive forces: the rolling resistance force F_{rr}, related to the friction of the wheel on the road, the aerodynamic force F_{ad}, opposed by air, the grading force F_g, related to the presence of slopes in the driving cycle [71]. Thus, the total resistance force F_r is defined as:

$$F_{\mathrm{r}} = F_{\mathrm{rr}} + F_{\mathrm{ad}} + F_{\mathrm{g}} \tag{3.1}$$

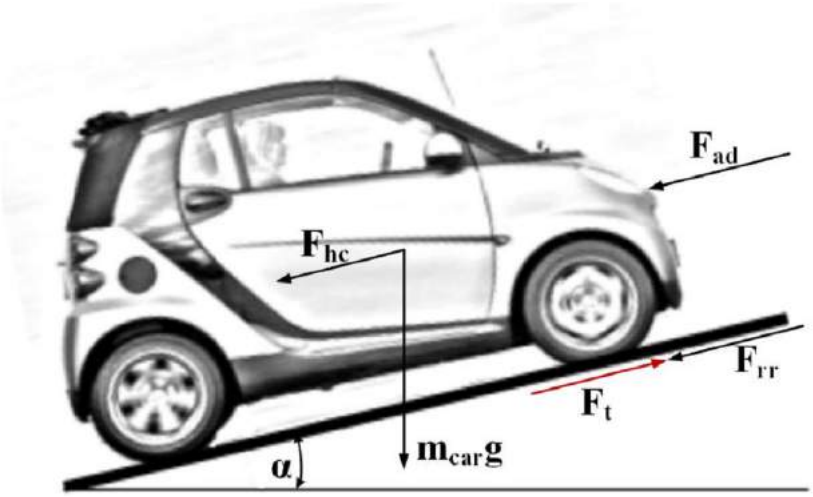

Figure 3.1.1: Forces applied on the vehicle.

$$F_{\mathrm{rr}} = m_{\mathrm{car}} * g * \mu_{\mathrm{rr}} * cos(\alpha) \tag{3.2}$$

$$F_{\mathrm{ad}} = \frac{1}{2} * \rho_{\mathrm{air}} * C_{\mathrm{D}} * A_{\mathrm{f}} * (v_{\mathrm{car}} - v_{\mathrm{wind}})^2 \tag{3.3}$$

$$F_{\mathrm{g}} = m_{\mathrm{car}} * g * sin(\alpha) \tag{3.4}$$

During a given driving cycle, the engine has to apply a tractive force F_t that can be determined as follows:

$$F_{\mathrm{t}} = F_{\mathrm{r}} + m_{\mathrm{car}} * \delta * \frac{dv_{\mathrm{car}}}{dt} \tag{3.5}$$

where δ is the equivalent parameter that takes into account the inertias of the rotating components of the vehicle [71].

Table 3.1.1: Parameters of Vehicle Dynamics

Parameter	Symbol	Value	Unit
Vehicle mass	M	970	Kg
Gravitational acceleration	g	9.887	$\frac{m}{s^2}$
Rolling resistance coefficient	μ_{rr}	0.013	-
Grade climbing	α	0	$\circ$
Air density	ρ_{air}	1.225	$\frac{kg}{m^3}$
Aerodynamic drag coefficient	C_D	0.35	-
Vehicle frontal area	A_f	2.1	m^2
Radius tire	r_d	0.28	m

Table 3.1.2: Parameters of PowerTrain

Parameter	Symbol	Value	Unit
Continuous motor power	P_{nom}	40	kW
Maximum motor power	P_{max}	80	kW
Rated motor efficiency	$\eta_{\mathrm{m_{nom}}}$	0.9	-
Nominal Torque	T_{nom}	133	Nm
Maximum motor angular speed	N_{m}	11000	rpm
Maximum vehicle speed	v_{max}	125	$\frac{km}{h}$
Recovery energy	κ	20	%
DC/DC converter efficiency	η_{conv}	0.97	-
Transmission system efficiency	η_{trasm}	0.95	-

Table 3.1.3: Parameters of Battery Pack

Parameter	Symbol	Value	Unit
Nominal capacity	C_{nom}	44	Ah
Battery pack nominal voltage	V_{nom}	344	V

3.1.2 Powertrain

The powertrain model consists of four main subsystems. Starting from the wheels, the first component to be modelled is the transmission subsystem. Commonly, the BEVs uses a single gear transmission system or a direct driver one. Consequently, a single gear transmission, characterized by a transmission ratio G of 9.3 and a transmission efficiency η_{trasm} equal to 95% have been firstly considered. The low speed transmission system output is directly connected to the electric motor shaft which applies the moving torque to the drive shaft, increased by the gear ratio. Nowadays, permanent magnet synchronous motor (PMSM) is the best performing electric machine among those used in EV applications for their light weight and reliable control [72]. For these reasons, a PMSM drive has been assumed as electric powertrain for the development of the proposed simulation algorithm. The DC/AC inverter, which supplies the PMSM, and the DC/DC converter, which manages the energy exchange between the battery and the DC/AC inverter, are modeled as an unique block. In fact considering that the purpose of the modeling is to simulate the driving cycle of a BEV by an energy point of view and that the dynamics of current controllers are much faster than the mechanical one, the current dynamics is assumed instantaneous and hence the electric block is described by a means of blocks. As previously said, the electric motor is connected to the wheels thanks to the transmission system. For a given driving cycle, according to the road loads and to the transmission system efficiency, the PMSM transmits the motor torque T_m to the shaft. Consequently, the torque and the power at the tires are defined by [71]:

$$T_{\text{wheels}} = F_{\text{r}} * r_{\text{t}} = T_{\text{m}} * G * \eta_{\text{trasm}} \tag{3.6}$$

$$P_{\text{wheels}} = F_{\text{T}} * v_{\text{car}} \tag{3.7}$$

where T_{wheels} and T_m are the wheel and the motor torque. The PMSM torque and mechanical power can be evaluated as:

$$T_{\text{m}} = \frac{T_{\text{wheels}}}{G * \eta_{\text{trasm}}} \tag{3.8}$$

$$P_{\text{m}} = T_{\text{m}} * \omega_{\text{m}} \tag{3.9}$$

ω_m being the motor speed. As one can see in equations (3.8) and (3.9) the choice of the gear ratio G defines the rated torque and consequently the requested power to the electric motor. In particular, the energy management and driving performances of the entire EV system can be improved evaluating accurately both the gear ratio value and the number of gears, as shown in the next subsections [73]. On the basis of the PMSM power request, the battery supplies the following power:

$$P_{\text{b}} = T_{\text{m}} * \omega_{\text{m}} * \eta_{\text{m}} * \eta_{\text{conv}} \tag{3.10}$$

where η_{conv} and η_m represent the DC/AC converters block efficiency and the motor efficiency, respectively [71]. The motor efficiency is defined in the model by taking into account the power losses evaluation in [74]. Thus, a look-up table that reports the electric motor efficiency map in relation to the rotor speed has been implemented. When the vehicle speed decreases, the PMSM operates as a generator and delivers to the battery the recovered braking power:

$$P_{\text{b}} = \frac{\kappa * T_{\text{m}} * \omega_{\text{m}}}{\eta_{\text{m}} * \eta_{\text{conv}}} \tag{3.11}$$

κ being the recovery energy percentage. It is worth noting that the energy performance of BEV can be improved resorting to regenerative braking, that allows a partial energy recovery. In order to avoid a specific evaluation based on the DC/DC converter regenerative braking characteristics and for a general analysis of the sys-

tem, a 20% regenerative braking has been considered.

3.1.3 Battery

Currently, the most common battery installed on EV is that belonging to the lithium ion class. The Lithium Iron Phosphate ($LiFePO_4$, LFE) and the Lithium Polymer (LiPo) are the two main electrochemical cell types installed on EV. Although, LiPo batteries have better characteristics than the LFE ones in term of energy and power density, the LFE are the most used in EV design, thanks to their higher lifecycle time and safety [75]. For these reasons, a LFE battery pack has been considered in the model. The battery pack is the most critical component of the EV system because its performance influences the travel range, the vehicle performance and the final cost of the vehicle. For this reason, many studies have been focused on the modelling of the lithium ion battery in order to represent the physical behavior and to evaluate the energy performance during all operating conditions [76], [77]. The battery models proposed in the scientific literature can be grouped into three classes: electrochemical models, mathematical models and electrical circuit models [78], [79]. The first one well represents the physical and chemical phenomena of the battery, but requires information not provided by the manufacturers and it is more complex than the other two [80]. Mathematical models are inadequate to be implemented on circuit simulation software due to their inaccuracy and the difficulties to relate model parameters to battery characteristics [78]. Finally, the electrical battery models are the most used in the simulation of power system [79], [80], [81]. In particular, the simplest configuration is based on a constant voltage generator in series with an internal resistance R_0, but it doesn't correctly reproduce the dynamics of the battery: the introduction of n-RC parallel networks improves the accuracy of the model but increases the complexity [76], [77]. Consequently, the trade-off between accuracy and simplicity is represented by an equivalent circuit with one RC block (Fig. 3.1.2). The chosen equivalent circuit is referred to the single battery cell and the related parameters are obtained from (3.12-3.14):

$$I_{\text{cell}} = \frac{I_{\text{batt}}}{N_{\text{p}}} \tag{3.12}$$

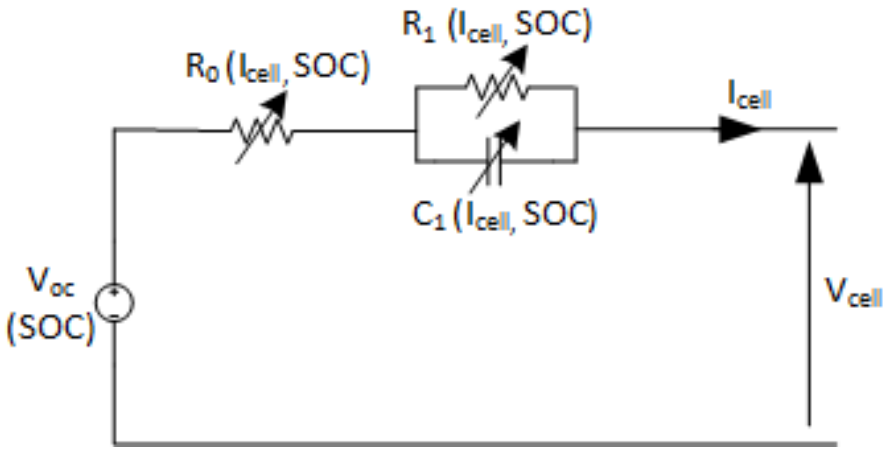

Figure 3.1.2: The battery electrical equivalent circuit implemented.

$$V_{\text{cell}} = V_{\text{oc}} - I_{\text{cell}} * R_0 - V_{\text{c}} \tag{3.13}$$

$$V_{\text{batt}} = V_{\text{cell}} * N_{\text{s}} \tag{3.14}$$

where I_{cell} and V_{cell} represent the current and the voltage of the single battery cell, whereas V_c and N_s are the RC block voltage and the number of series cells, respectively. In the chosen battery model configuration, dynamic parameters have been considered in order to better represent its behavior, especially for EV application. Consequently, R_0, R_1 and C_1 will depend on SOC and on the sign of the current (charging/discharging process). In the same way, according to data literature [82], [83], V_{OC} has been modelled as a variable voltage generator because it strictly depends on the SOC, as reported in (3.15):

$$V_{\text{OC}} = a_1 * SOC_4 + a_2 * SOC_3 + a_3 * SOC_2 + a_4 * SOC + a_5 \tag{3.15}$$

where the coefficients a_1, a_2, a_3, a_4 and a_5 have been determined by means of a fitting function on Matlab environment. Thus, considering the results of the ratio between the power requested by the motor and V_{batt}, I_{batt} has been defined as follows:

$$I_{\text{batt}} = \frac{P_{\text{batt}}}{V_{\text{batt}}} \tag{3.16}$$

The evolution of the battery consumption after a given driving cycle (3.17) is obtained by considering the SOC time evolution:

$$SOC_{\text{n}} = SOC_{\text{n-1}} + \frac{\int_0{}^{\text{T}}(I_{\text{batt}} * dt)}{3600 * C_{\text{nom}} * N_{\text{p}}} \tag{3.17}$$

I_{batt} being the battery pack current and P_{batt}, V_{batt}, dT, C_{nom} and N_p the battery power requested by the motor, the voltage of the battery pack, the time-step of the simulation, the nominal capacity and the number of cell connected in parallel, respectively.

3.1.4 Comparison of transmission systems: single and double gear

As previously reported, the proposed EV model has been implemented on Matlab environment. The electric vehicle parameters related to the dynamics, the vehicle structure, the powertrain and the battery are reported in Table 3.1.1, 3.1.2 and 3.1.3, respectively. For the sake of completeness, the New European Driving Cycle (NEDC), reported in Fig. 3.1.3, has taken into account in the simulations. It consists of two main parts: four repeated urban driving cycles and one extra-urban driving cycle.

On the basis of the EV's battery SOC time evolution (Fig. 3.1.4) and referring to the base configuration of a single gear transmission system, the maximum EV driving range is estimated to be equal to 161 km, by considering the NEDC. Clearly this value could decrease when the road conditions change or when the auxiliary subsystems are activated. In particular, regards to the road characteristics, it is important to define the capacity of the vehicle to climb a slope. Thus, the maximum reachable grade climbing α is obtained by [73]:

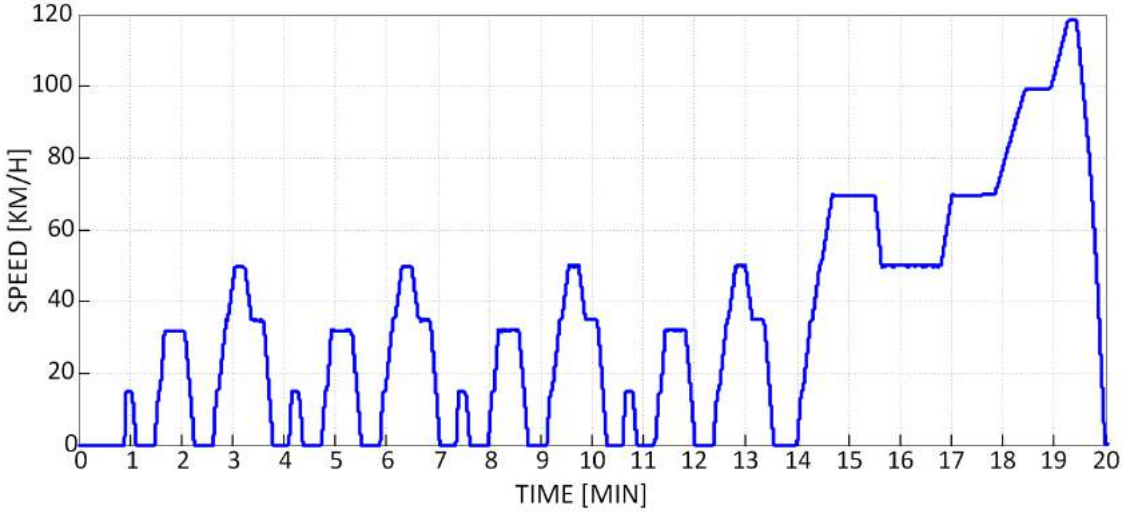

Figure 3.1.3: The New European Driving Cycle (NEDC).

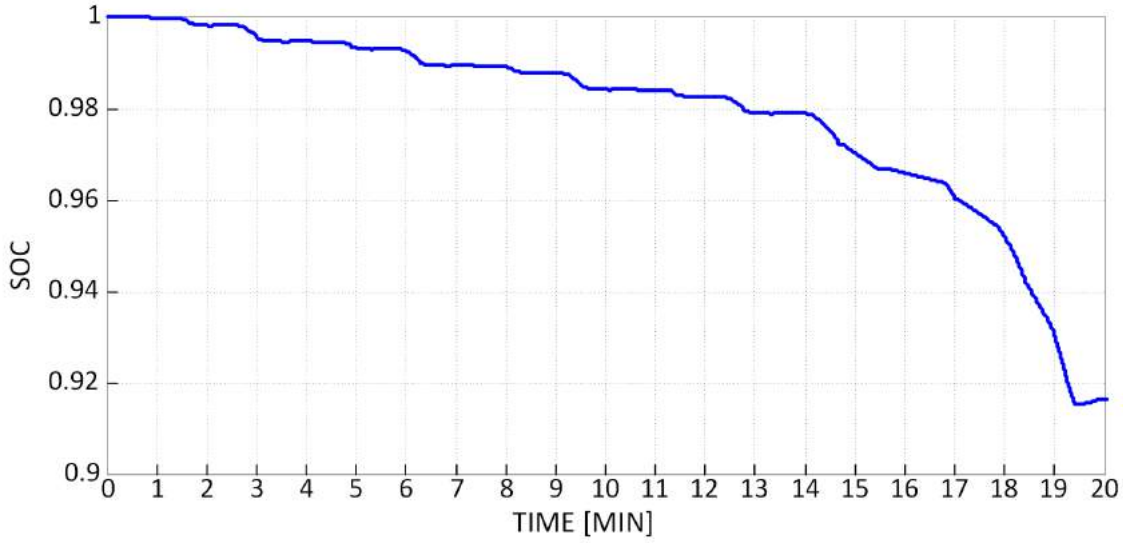

Figure 3.1.4: Time evolution of the SoC during the NECDC execution.

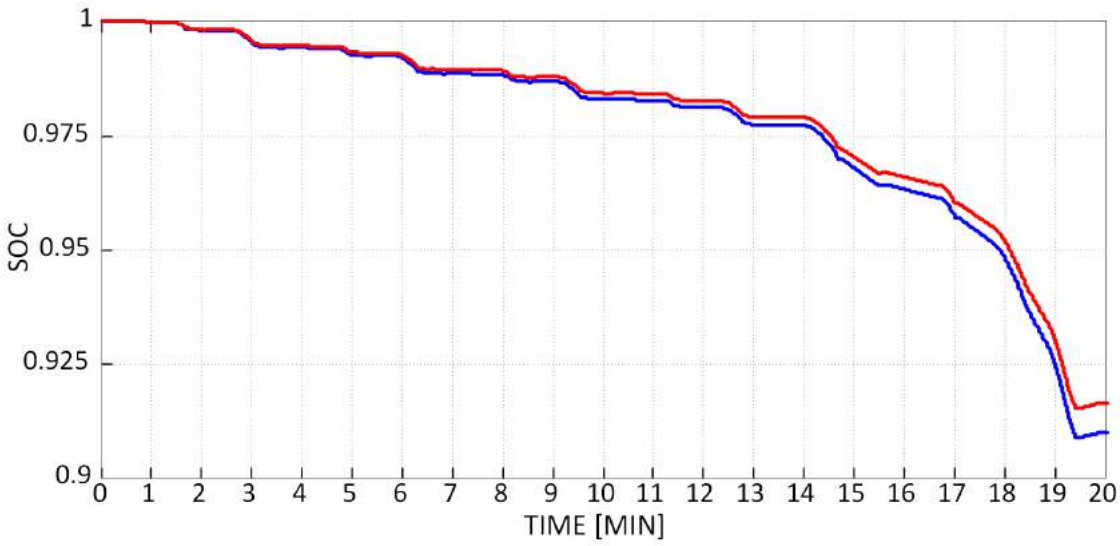

Figure 3.1.5: Comparison of battery energies required by the NEDC with (blue line) and without (red line) regenerative braking.

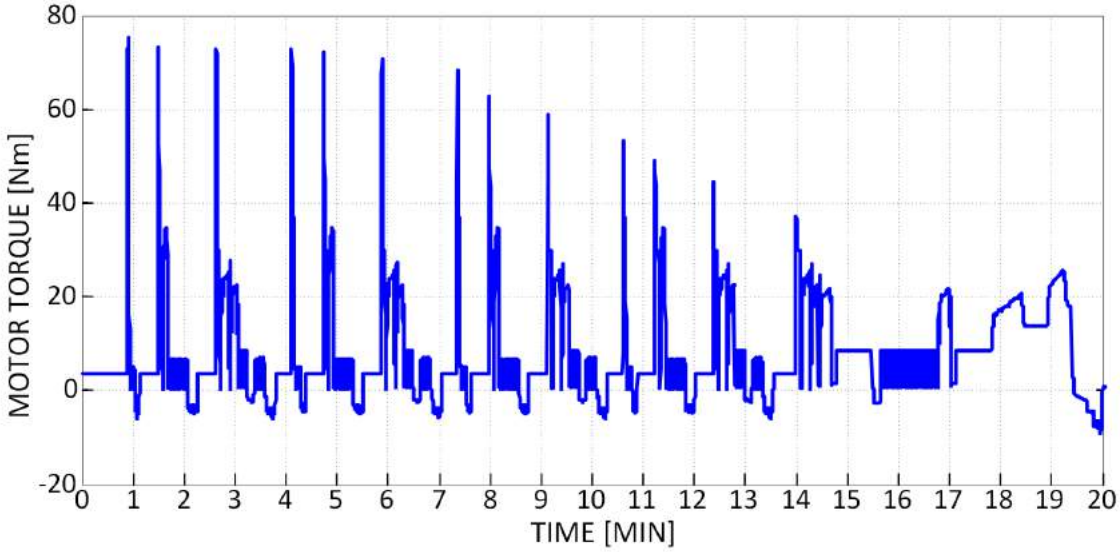

Figure 3.1.6: Motor torque required by the NEDC.

$$G_{\max} = \frac{r * m_{\text{car}} * g * (\mu_{\text{rr}} * cos(\alpha) + sin(\alpha))}{\eta_{\text{trasm}} * \eta_{\text{mnom}} * T_{\text{nom}}} \tag{3.18}$$

T_{nom} and η_{mnom} are the rated motor torque, set to 133 Nm, and the rated motor efficiency, set to 0.9. On the basis of this analysis, the maximum grade climbing at the given gear value G (previously reported as 9.3) is equal to 23°.

The energy provided from the battery during one NEDC has been evaluated and reported in Fig. 3.1.5. Thanks to the energy recovery due to the regenerative braking strategy, in the last part of the graph can be clearly observed the SOC increase associated to the regenerative charging process when the vehicle speed passes from 120 to 0 km/h. With regard to one NEDC, the estimated total energy saving, compared with the case of absence of regenerative braking, is estimated to be equal to 189 Wh. This result highlights the importance of an appropriate energy management strategy for reducing the energy losses. In fact, the regenerative braking percentage could be increased on the basis of the DC/DC converter limits. Finally, the motor torque has been evaluated (Fig. 3.1.6) and it is characterized by a maximum value of about 80 Nm.

As previously presented, the evaluation of the BEV performance has been focused in particular on the number of the gears of the transmission system. Commonly, commercial BEVs are characterized by single gear transmission system or direct driver without gear reduction. In this solution, larger motors have to be used in order to balance torque and speed needs [73]. For these reasons, more and more studies have recently focused their attention on different transmission configurations [73], [84], [85], [86], [87]. In particular, many researches have highlighted that a multi speed transmission system can reduce the battery energy consumption and improve the overall efficiency of the vehicle [88], [89], [90], [87]. Thus, a two-speed gear transmission system has been examined in order to evaluate the impact of this solution on the EV performance. The first gear has been calculated by using (3.18) at low speed, while the second one by considering the top speed [73]:

$$G_{\min} = \frac{N_{\text{m}} * r * \pi * 3.6}{30 * v_{\max}} \tag{3.19}$$

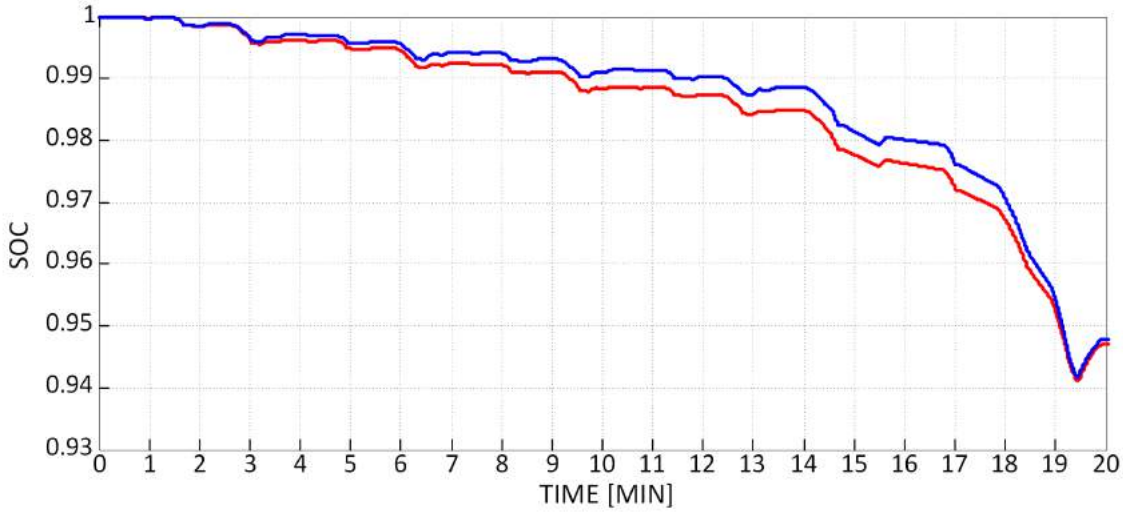

Figure 3.1.7: Comparison of battery SoC time evolution required by one NEDC with one gear (red line) and two-speed gear (blue line) transmission system by considering a shifting speed of 58 km/h.

The adoption of a higher gear can led to a better climbing performance without stress the electric motor. In (3.19) the minimum gear G_{min} is defined by imposing a top vehicle speed of 130 km/h (against 125 km/h reached in the first version) and it has a value of 8.93. As one can notice, climbing and top speed reach better results by adopting the two-speed transmission configuration. On the other hand the transmission efficiency decreases to 90% due to the friction and mechanical losses associated to additional components related to a multiple gear system.

Nevertheless, as reported in Table 3.1.4, these losses do not impair the BEV performance and in particular the battery efficiency. In fact, the choice of a two-speed gear transmission system leads the electric motor to operate on higher efficiency points. This advantage could be further improved by a specific gear shifting strategy. In this study, the vehicle speed has been considered as the reference condition to shift from one gear to another. In particular, the analysis has been conducted taking into account two different vehicle speed values: 58 and 72 km/h. As one can see in Fig. 3.1.7, the BEV battery energy consumption is quite the same of the one obtained with a single gear transmission system if a shifting speed of 58 km/h is considered. By increasing this value to 72 km/h, the SOC time evolution changes as shown in

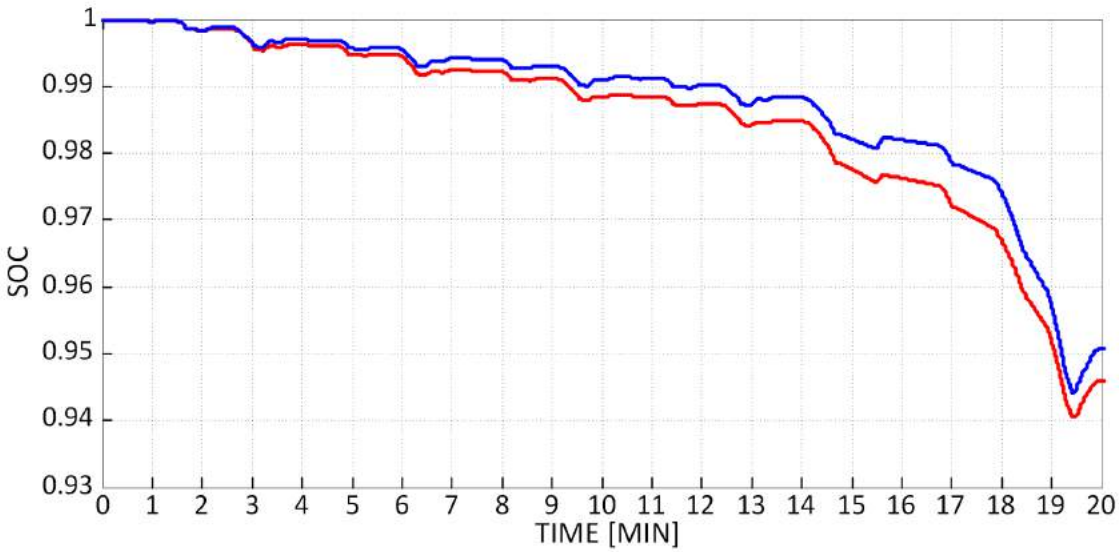

Figure 3.1.8: Comparison of battery SoC time evolution required by one NEDC with one gear (red line) and two-speed gear (blue line) transmission system by considering a shifting vehicle speed of 72 km/h.

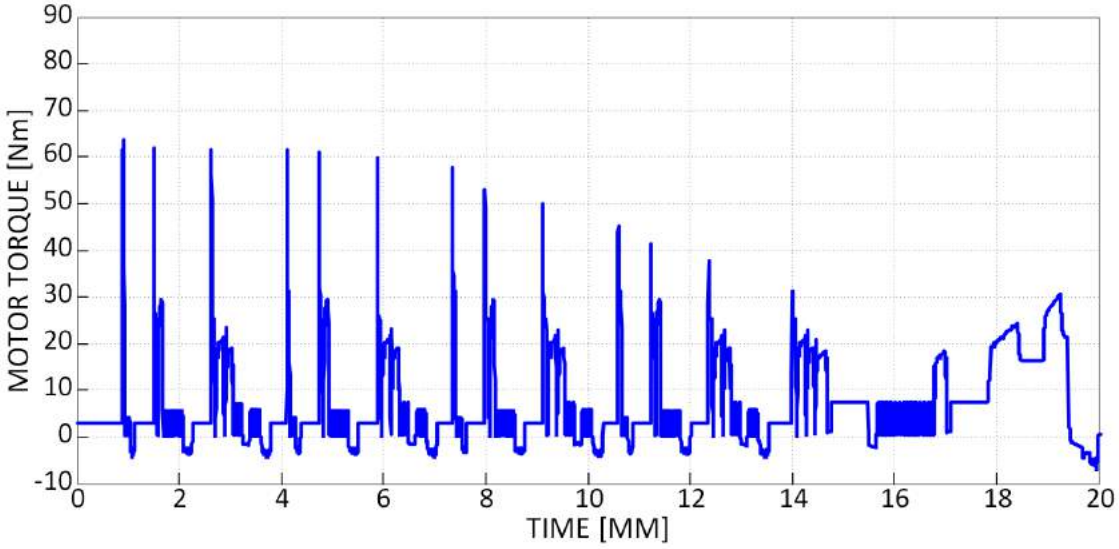

Figure 3.1.9: Motor torque required by the NEDC by considering a two-speed gear transmission system by considering a shifting vehicle speed of 72 km/h.

Table 3.1.4: Comparison between a single and a two-speed gear transmission systems

Parameter	Single Gear	Two-speed gear ($v_{\text{SHIFT}} = 58\frac{km}{h}$)	Two-speed gear ($v_{\text{SHIFT}} = 72\frac{km}{h}$)
Top speed $[\frac{km}{h}]$	125	130	130
Grade climbing $[^0]$	23	32	32
SOC (after one NEDC repeated)	0.9459	0.9456	0.9507
Driving range [km]	161	160	176

Fig. 3.1.8: the battery performance has been improved and consequently the driving range, which reaches an estimated value equal to 176 km. This shifting strategy highlights that the use of a second lower gear in correspondence of a higher vehicle speed conducts to a better BEV energy performance. Nevertheless, it is not possible to increase excessively the shifting condition without taking into account the electric motor characteristics. In this analysis, a maximum shifting speed equal to 72 km/h has been adopted in order to respect the motor speed maximum performance, set to 11000 rpm. Finally, by considering a shifting vehicle speed of 72 km/h, the time evolution of the electric drive torque (Fig. 3.1.9) referred to one NEDC execution shows a maximum value lower than in the case of a single gear transmission system (Fig. 3.1.6). It is worth noting that when a two-speed transmission system is considered, many performance parameters are improved. These results highlight that the gear transmission system represents a significant component for the energy management of an electric vehicle. Moreover, the reduction of the mechanical and friction losses could lead to an improvement of the transmission system efficiency. A better BEV performance could also be achieved. The results show that a complete and correct BEV energy strategy must take into account the battery energy consumption and the system drive limitations. Definitely, this comparison highlights that in the proposed case a two-speed gear configuration could represent a promising choice to achieve a

balance among different performance needs in BEV.

3.2 Second Model

The second model has been improved in relation to the one presented above where the BEV performance had been analyzed by considering the standard driving cycle NEDC. In this section, a different PMSM drive size and a different battery tipology have been evaluated. Regarding to the battery, the modeling process has been based on [91] and then the defined equivalent circuit has been improved step-by-step, by taking into account two RC blocks (instead the one considered in the first model) with the aim to more accurately represent the battery dynamic behavior in real driving conditions. Finally, the performance of the proposed vehicle model has been validated by considering two real driving paths, which are characterized by rapid speed changes and stop and go steps. On the basis of these data, the model has shown a good accuracy referring to the battery parameters, such as the SOC and the total battery voltage, V_{batt}.

3.2.1 The new battery model

The modeling method proposed in [91] has been taken into account. In [91] the battery behavior has been evaluated only in relation to the charging process, whereas, concerning this model, the method proposed has been implemented in the simulation algorithm in order to represent the battery performance also in real conditions, for example in correspondence to rapid vehicle speed changes.

Firstly, the experimental data at different charging rates referred to a Li-ion battery have been considered. Secondly, a normalized charging profile has been determined by following the steps in [91]. Thus, the circuit model can be defined by:

$$V_{\mathrm{t}} = \alpha_0 + \alpha_1 * t + \beta_1 * e^{\mathrm{a_1}*\mathrm{t}} + \beta_2 * e^{\mathrm{a_2}*\mathrm{t}} \tag{3.20}$$

where the voltage V_t represents the battery dynamic response in correspondence of an unit step of current at $1C$ [91]. Throughout the fitting process of the normalized charging profile, the parameters a_1, a_2, α_0, α_1, β_1 and β_2 have been obtained. Then,

the Laplace transformation has been applied to (3.20) in order to find the circuit elements [91]:

$$H_{\mathrm{s}} = \frac{\alpha_1}{s} + \frac{\beta_1 * a_1}{s + a_1} + \frac{\beta_2 * a_2}{s + a_2} \tag{3.21}$$

The above equation can be divided in three components that represent one storage and two transient elements. By considering the following equations, the equivalent circuit parameters have been identified by [91]:

$$R_1 = \frac{\beta_1}{I_{\mathrm{cell}}} \tag{3.22}$$

$$C_1 = \frac{3600 * C_{\mathrm{nom}}}{a_1 * R_1 * I_{\mathrm{cell}}} = \frac{3600 * C_{\mathrm{nom}}}{a_1 * \beta_1} \tag{3.23}$$

$$R_2 = \frac{\beta_2}{I_{\mathrm{cell}}} \tag{3.24}$$

$$C_2 = \frac{3600 * C_{\mathrm{nom}}}{a_2 * R_2 * I_{\mathrm{cell}}} = \frac{3600 * C_{\mathrm{nom}}}{a_2 * \beta_2} \tag{3.25}$$

C_{nom} and I_{cell} being the nominal capacity of the battery pack and the current of the single cell, respectively. Moreover, the identification process of the internal resistance R_0 presented in [91] has been improved by a step-by-step optimization in the simulation algorithm. Thus the R_0 value has been found equal to 1.8 and 1.25 mΩ in relation to the charging and the discharging operations. Consequently, the proposed equivalent circuit is based on a voltage generator in series with an internal resistance R_0 and two RC parallel networks thanks to which the battery dynamic behavior has been properly evaluated both in charging/discharging processes and in real driving conditions, as reported in Fig.3.2.1. Once the battery pack current I_{batt}, the number of series cells N_s and parallel string N_p have been defined, the other ones have been derived by considering the single battery cell circuit (3.26-3.28):

$$I_{\mathrm{cell}} = \frac{I_{\mathrm{cell}}}{N_{\mathrm{p}}} \tag{3.26}$$

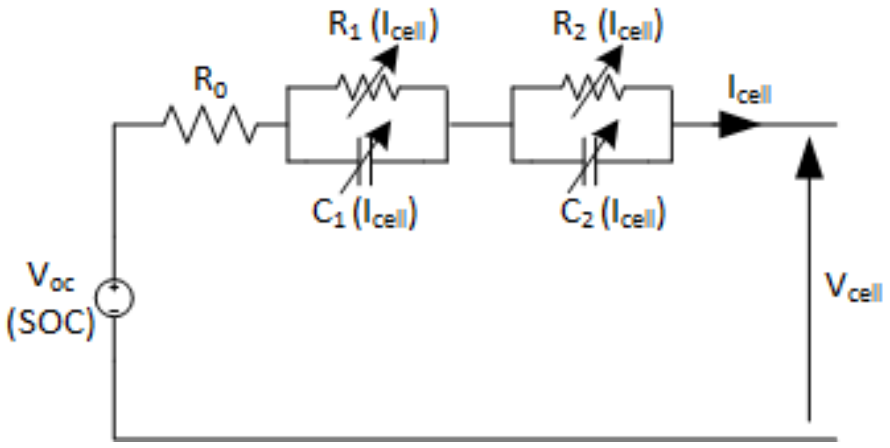

Figure 3.2.1: The adopted equivalent electrical circuit

$$V_{\text{cell}} = V_{\text{OC}} - I_{\text{cell}} * R_0 - V_{\text{C1}} - V_{\text{C2}} \tag{3.27}$$

$$V_{\text{batt}} = V_{\text{cell}} * N_{\text{s}} \tag{3.28}$$

where V_{cell} is the voltage of the single battery cell, V_{C1} and V_{C2} are the RC block voltages. While the circuit elements R_1, C_1, R_2 and C_2 depend on the current value, as shown in (3.22-3.25), the V_{OC} is strictly dependent on the SOC and consequently it has been modeled as a variable voltage generator:

$$V_{\text{OCn}} = V_{\text{OCn-1}} - \frac{I_{\text{cell}} * dT}{C_{\text{b}}} \tag{3.29}$$

where the coefficient C_b represents the storage element in (3.21) and it can be considered as a capacitor, whose value has been obtained by (3.30). In [91] this parameter is considered as a constant defined in the modeling process by:

$$C_{\text{b}} = \frac{3600 * C_{\text{nom}}}{\alpha_1} \tag{3.30}$$

Nevertheless, on the basis of the experimental data and throughout a step-by-

step optimization, C_b has been implemented in this model as a function of SOC by means the variable α_1. Thus, thanks to this improvement, the evolution of the battery voltage will be more realistic, especially in correspondence of rapid changes in the requested power by the driver needs.

3.2.2 Simulation Results and Model Validation

A Smart Fortwo Electric Drive has been considered in the simulation algorithm. The main characteristics have been presented in Tab. 3.2.2 and 3.2.4. The vehicle experimental data have been collected by installing on-board an EV performance monitoring device, provided by FleetCarma. The data logger saved the main battery parameters throughout the connection to the On-Board Diagnostics (OBD-II) port. In order to validate the battery model both regarding the charging/discharging processes and a driving path, firstly a real charging process has been taken into account by considering the Smart Electric Drive charging data. The charging current has been set equal to 7 A, i.e. 0.1C, on the basis of the charging infrastructure settings. The process started at SOC of 40% untill the complete charge of the vehicle. Then the real data has been compared with the simulation ones. As reported in Fig.s 3.2.2, 3.2.3 and in Table 3.2.1, a good accuracy is highlighted both for the SOC and the V_{batt}, with a maximum error of 0.5% and 1%, respectively. Moreover, the experimental data have been also collected during two real driving paths, in which the vehicle speed rapidly changes, as reported in Fig. 3.2.4 and 3.2.5. The experimental vehicle parameters recorded are the vehicle speed, the SOC and the battery total voltage V_{batt}. The first one has been implemented in the model as the input parameter in order to replicate the overall system performance and consequently validate the vehicle model. Although many studies consider standard driving cycles in order to demonstrate their model effectiveness, two driving path recorded under real road conditions have taken into account. Thus, the energy battery requirements are more accurately evaluated. The two real driving cycles are composed by urban and extra urban parts. The battery voltage V_{batt} and the SOC are related to the two

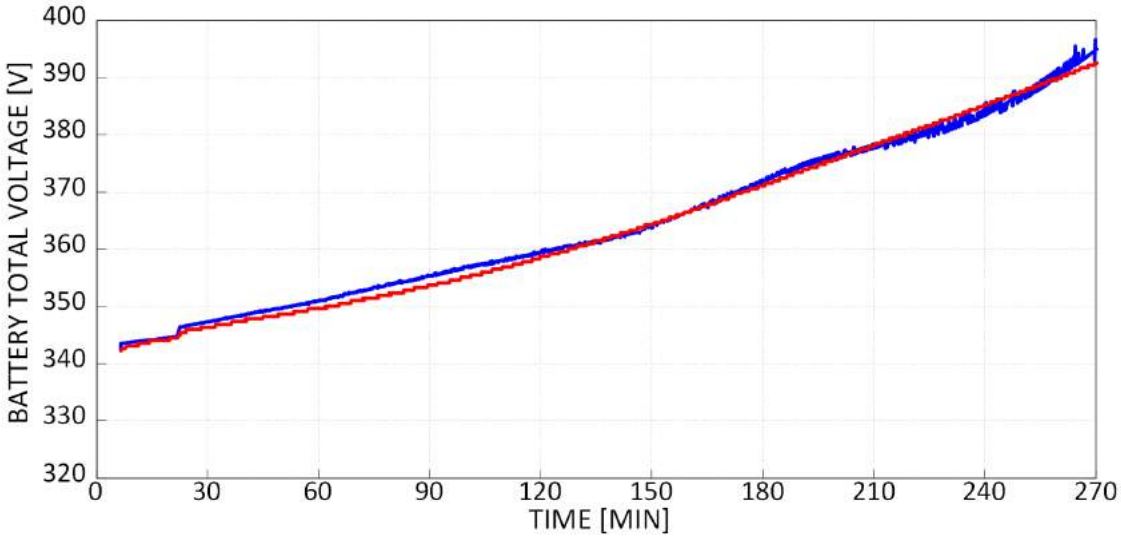

Figure 3.2.2: Voltage time evolution during the charging process in relation to the model (red line) and the experimental data (blue line).

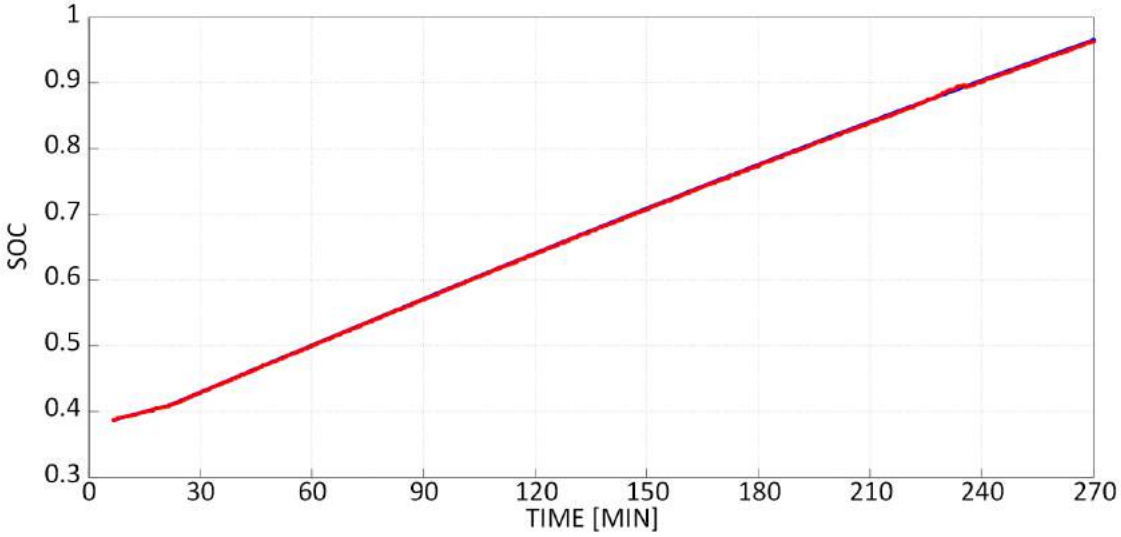

Figure 3.2.3: SOC evolution during the charging process in relation to the model (red line) and the experimental data (blue line).

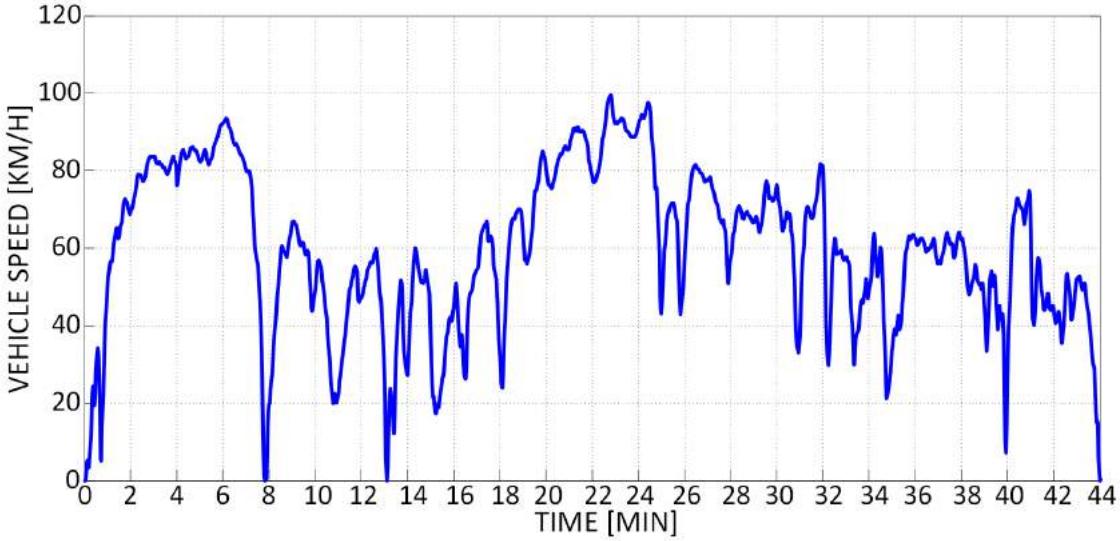

Figure 3.2.4: First driving cycle

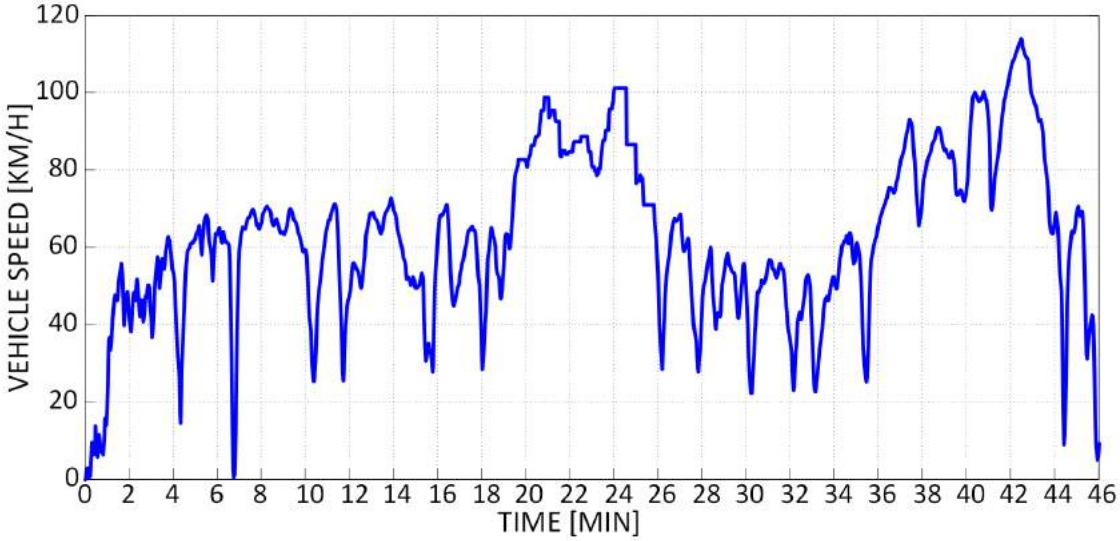

Figure 3.2.5: Second driving cycle.

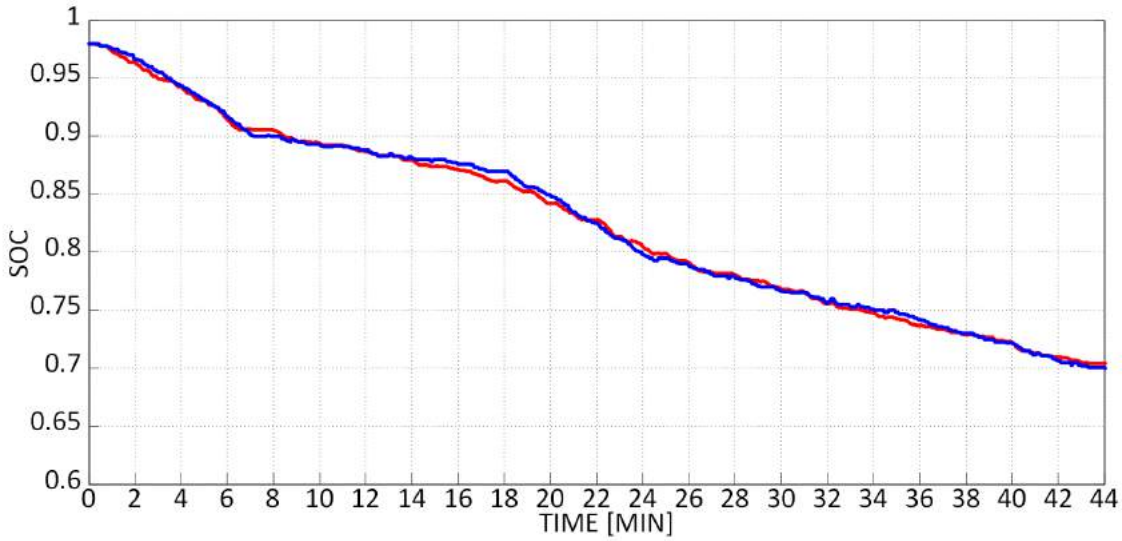

Figure 3.2.6: SOC time evolution during the first driving cycle in relation to the model (red line) and the experimental data (blue line).

presented driving cycles, as shown in Fig. 3.2.6-3.2.9. As one can observe, the simulated parameters are quite similar to the real ones. In particular, as reported in Tab. 3.2.5, the modeled SOC is characterized by a mean error equal to 0.35% and 0.54% in relation to the first and the second driving cycle. Similarly, the V_{batt} evolutions highlight a mean error equal to 0.53% and 0.46%, respectively. Thus, on the basis of the simulation results, the model can accurately reproduce the battery performance. It is worth noting that the SOC prediction is fundamental in order to develop a suitable energy strategy and it is strictly related to the V_{OC} prediction and consequently to the V_{batt} one, as reported in (3.30).

Finally, it is worth noting that the simulation process provides the SOC and the V_{batt} evolutions in a very low computational effort. This feature makes it suitable for being used by smart phone systems as feedback devices for an EV aggregator service provider and consequently to be implemented both in smart city and in a MG for the integration and management of EVs charging infrastructure. On these basis, the EV models have been implemented in the two MSs presented in the following

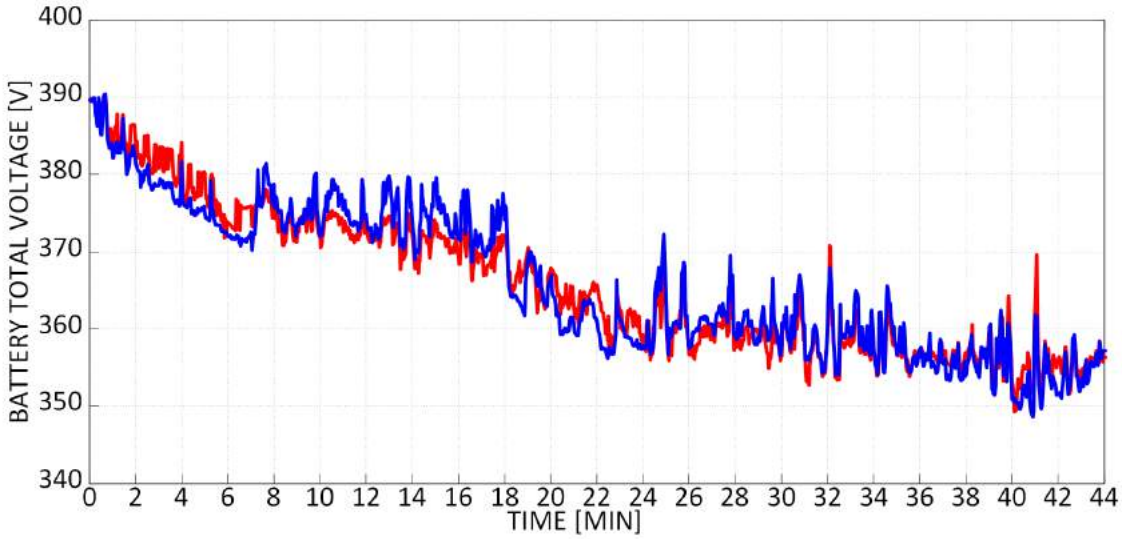

Figure 3.2.7: Battery voltage time evolution during the first driving cycle in relation to the model (red line) and the experimental data (blue line).

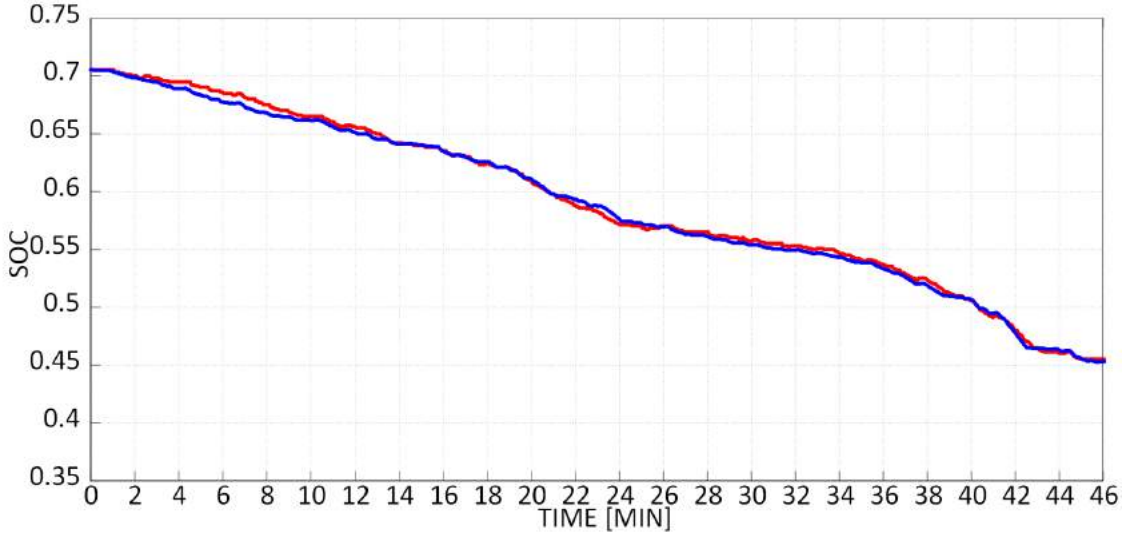

Figure 3.2.8: SOC time evolution during the second driving cycle in relation to the model (red line) and the experimental data (blue line).

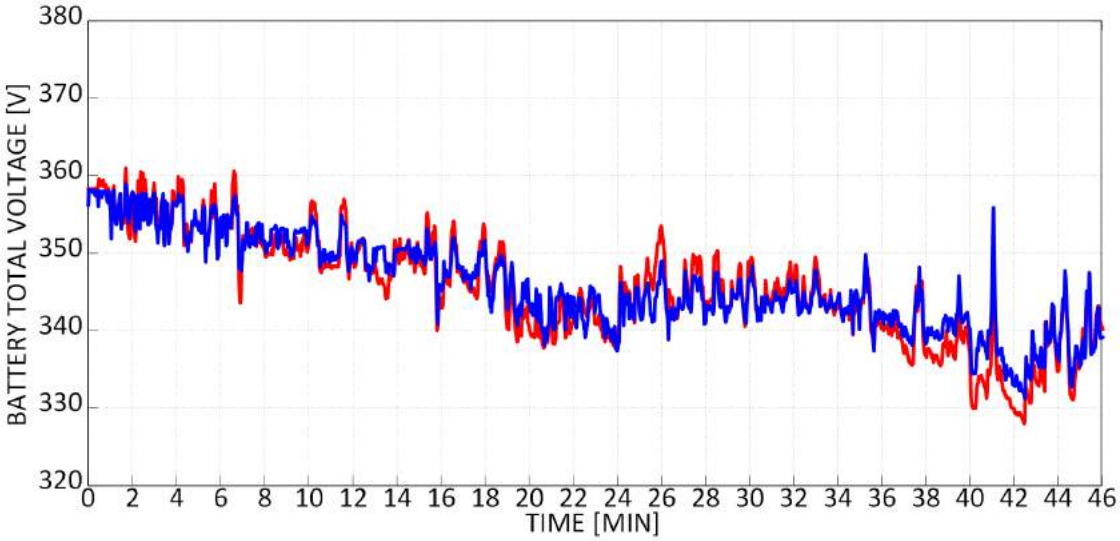

Figure 3.2.9: Battery voltage time evolution during the second driving cycle in relation to the model (red line) and the experimental data (blue line).

Table 3.2.1: Real and Simulation Data Comparison for a Charging Process

	Mean Error [%]	Max Error Unit [%]
Total Battery Voltage (V_{batt})	0.38%	1%
SOC	0.2%	0.5%

Chapter, in order to correct manage the charging/discharging processes inside a MG characterized by a large presence of RESs and of charging infrastructures.

Table 3.2.2: Parameters of Vehicle Dynamics

Parameter	Symbol	Value	Unit
Vehicle mass	M	970	Kg
Gravitational acceleration	g	9.887	$\frac{m}{s^2}$
Rolling resistance coefficient	μ_{rr}	0.013	-
Grade climbing	α	0	$\circ$
Air density	ρ_{air}	1.225	$\frac{kg}{m^3}$
Aerodynamic drag coefficient	C_D	0.35	-
Vehicle frontal area	A_f	2.1	m_2
Radius tire	r_d	0.28	m

Table 3.2.3: Parameters of PowerTrain

Parameter	Symbol	Value	Unit
Continuous motor power	P_{nom}	35	kW
Maximum motor power	P_{max}	55	kW
Maximum Torque	T_{max}	130	Nm
Maximum vehicle speed	v_{max}	125	$\frac{km}{h}$

Table 3.2.4: Parameters of Battery Pack

Parameter	Symbol	Value	Unit
Nominal capacity	C_{nom}	52	Ah
Nominal energy	E_{nom}	17.6	kWh
Battery pack nominal voltage	V_{nom}	344	V
Number of cells	N_s	93	-
Number of parallels	N_p	1	-

Table 3.2.5: Actual and Simulation Comparison

	Mean Error	Max Error Unit
SOC (first path)	0.35%	1%
V_{batt} (first path)	0.53%	1.7%
SOC (second path)	0.5%	1.5%
V_{batt} (second path)	0.46%	1.7%

Once we accept our limits, we go beyond them.

Albert Einstein

4

Management Strategies for MGs

The extensive installation of grid-connected renewable energy sources (RESs) is causing critical condition in the power system of many European countries due to the presence of overproduction phenomena. Therefore, it is essential to develop suitable management strategies that overcome this critical issue, permitting the integration of RESs in the power system, improving, at the same time, the power quality and system reliability. One of the most promising solutions is represented by the MG concept. As previously reported, a MG is a medium voltage or low voltage power grid, which can work both grid-connected or islanded and is composed of Distributed Generations (DGs), such as CPV and PV plants, Energy Storage Systems (ESSs), such as electric vehicles and stationary battery systems, loads and control devices [92]. By means the Energy Management System (EMS), it is aimed at the optimal managing of its components in order to improve the energy efficiency and guarantee the stability and security of the main grid, for example by maximising the self-consumption and by allowing the impact reduction of intermittent RES over the main grid, permitting, at the same time, their exploitation [92]. It can also satisfy

special requirements from the main grid regarding the power output of the MG, for example by providing a flat-programmable power production profile [92]. On these basis and in particular with the aim to increase the RESs exploitation, the energy storage system (ESS) plays a key role [93]. In fact, an ESS can improve the energy efficiency and optimize the power management of a MG throughout its charging/discharging process by means of which the RES energy can be exploited in different moments for MG needs. As previously reported, an ESS can be represented by a stationary battery system or by battery electric vehicles (BEV). In the first case, the ESS is devoted totally to the MG requirements, whereas, by considering a BEV, the MG purpose must be adapted at the driver needs. Thus, regarding the second case, a suitable management strategy has to take into account this two different issues and reconciliates them in order to improve the energy efficiency of the MG.

In this section, two management strategies (MSs) will be presented. In the first part a MG composed by office and laboratory loads, a CPV plant and a traditional flat-plate PV one and an BEV fleet has been taken into account. The MS proposed aims to maximize the energy self-consumption by respecting both the driver needs and the MG requirements. In particular, a Vehicle to Grid hysteresis control algorithm has been developed in order to reduce the impact of continuous charging current modulation on the electric vehicle battery [94]. In the second part, the same MG has been considered by employing a stationary storage system instead of a BEV fleet. In this case, the MS purpose is to guarantee a flat-programmable power production profile at the DC node of the MG, even in case of severe weather conditions. For this aim, the MS developed is based on a suitable combination of a one-day-ahead scheduling procedure and a real-time control algorithm [95].

4.1 V2G Strategies

Thanks to large battery capacity, BEVs can storage the off-peak energy produced by RESs. This energy can be further used either to power a vehicle motor during a driving cycle or to supply loads of the MG [96]. Moreover, EVs that are connected to the grid can be used in combination with ESSs to improve the power quality [19]. The

bidirectional usage of EV battery as a grid support is called Vehicle-to-Grid (V2G) [18]. In this approach the functions of the electric vehicle are not limited to the sustainable mobility but include also the providing of ancillary services to support the power system. However, such an usage of the EV battery leads inevitably to its more rapid degradation. As the effect, many studies have analyzed the impact of V2G on the battery life cycle [97],[98],[99]. More frequent replacements of the battery, due to the vehicle contribution to the V2G, could represent a problem for vehicle users as it implies additional costs. Another issue that inhibits the V2G diffusion is the anxiety of the driver not to be able to reach the final destination [18], [100]. In fact, the drivers principal concern is that the BEV guarantees an adequate driving autonomy and, at the same time, does not undergo significant reduction of the battery life cycle. Moreover, it has to be considered that, currently, the charging infrastructure is not compatible with V2G control strategies. To overcome this shortage either the infrastructure characteristics or control strategies need to be updated for V2G implementation. On the top of these considerations it is worth to point out that the management of the power grid should respect the BEV users needs as well as the infrastructure constraints in order to encourage the diffusion of the V2G technology. In this context the use of a hysteresis current control of a charging station can represent a suitable solution for the implementation of V2G in order to support the MG energy management system and preserve the EV battery life. In particular, two V2G strategies will be analysed in the following section. The first one, defined as *"continuous V2G"*, implies a continuous modulation of the charging current of EV battery. In the second one, defined as *"hysteresis V2G"*, the current set-point of the charging stations is defined by an hysteresis controller. The V2G strategies have been used to manage the EV batteries plugged in the migrogrid. The proposed management strategy has been tested on a case study represented by the power grid of the Technology Park of Sardinia. Finally, the comparison between the two strategies will be reported in order to point out the worth of the *"hysteresis V2G"*.

4.1.1 MG Description

The structure of the MG considered as a case study is a public administration unit. There are several offices and two laboratories inside the edifice hosting the MG. All the electrical devices which require powering are connected to a three-phase low voltage (LV) electricity distribution grid (three phase, rated voltage 400V and rated frequency 50Hz). The rated power supply is 250 kW. The electric load is constituted by devices used in offices, such as PCs, printers and faxes, as well as the laboratory equipment which are mainly electronic devices with non-linear characteristics. The presence of numerous non-linear loads causes a worsening of the grid quality by introducing harmonic distortion on the three phase current and by interfering with RES systems [101]. The MG is also supplied by a RES power plant constituted by two integrated photovoltaic systems. The first one is a flat plate photovoltaic power plant (PV), installed on the roof top of the building, characterised by a rated power of 18.7 kW_p and an overall annual estimated production of 23.7 MWh. The second one is a ground-mounted CPV system characterised by a rated power of 6.2 kW_p for DNI equal to 850 W/m^2. The electric system presents a charging station which supplies the two BEVs of the Renewable Energy Platform, used for employees' mobility. In particular, the EVs considered for the present analysis are two Mercedes Smart Electric Drive, whose dynamical model has been presented in Chapter 3. They are equipped with a 55 kW PMSM and with a 52 Ah rated capacity lithium ion battery. The batteries can be fully recharged in 7 h, 6 h or 1 h depending on the current set point value and the power availability of the charging socket. With the 22 kW battery charger if a 32 A three phase charging station is available the charging time can be reduced down to 1 h. In the V2G strategies analysis two different configurations of charging stations have been considered namely 7.4 and a 22 kW rated power. The block diagram of the MG under test is reported in Fig. 4.1.1.

4.1.2 MS Model

The intermittent characteristics of the RES energy production generally used in MGs lead to oversize the rating power of RES plants determining short-time overproduction delivered to the main grid. The increase of DGs, due to the planned exploitation

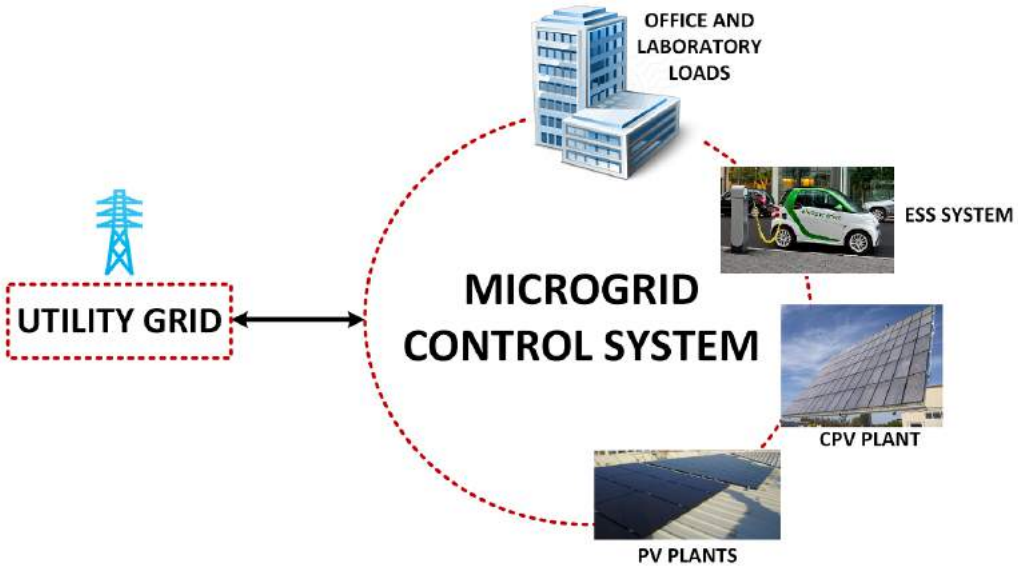

Figure 4.1.1: Block diagram of the MG under test.

of RES, cannot be supported properly by the main grid. For this reason, as to maximise the local self-consumption of RES production, some European countries are already supporting the development of ESSs. In this context the proposed management strategy has been developed. In particular, the control algorithm acts on the ESSs in order to reduce, according to their capacity C_{max} and power P_{batt}^{max} constraints, the energy delivered to the main grid. Hence, considering the instantaneous power balance condition:

$$P_{\mathrm{G}} = P_{\mathrm{L}} - P_{\mathrm{DG}} + P_{\mathrm{batt}} \tag{4.1}$$

where P_G is the power provided by the grid, P_L is the power demand of the MG, P_{DG} is the sum of the distributed generation in the MG and P_{batt} is the power drawn by the battery. Thus, the MS algorithm defines the set-poit for controlling the P_{batt} evolution such that:

$$\begin{cases} P_G = P_L - P_{DG} + P_{batt} \\ \\ \text{if } \|P_{batt}\| < P_{batt}^{max} \qquad\qquad 0 < (\int_0^t P_{\mathrm{batt}} * dt) < C_{\mathrm{max}} \end{cases} \tag{4.2}$$

It can be observed that the bidirectional operation of the battery allows the satisfaction of balance condition of MG, drown zero energy from the main grid, as long the power and capacity constraints are satisfied. Hence, the availability of power and capacity at distributed level to support the MG assumes a relevant importance. For this reason the possibility to use the EV as ESS has to be considered a suitable solution for the proposed MS. The V2G paradigm allows the implementation of the control algorithm reported in (4.2) imposing a set-point to the charging station. The charging station and the plugged vehicle have to be enabled to V2G mode in order to be able to perform the bidirectional exchange of the electricity from and to the EV battery. This implies the possibility to continuously modulate the charging/discharging current. For this reason the traditional V2G has been defined as *"continuous V2G"*. However, the continuous modulation of the battery current is not considered suitable profile for managing EV storage system because determines a reduction of its life cycle and of its performance, affecting negatively the EV reliability and autonomy. In fact, usually the charging station are characterised, in a defined range of SOC of the battery, by constant current profiles. For this purpose an alternative solution which preserves the EV battery performance imposing piecewise constant current profiles for implementing V2G, has been investigated and it is reported in the following section.

4.1.2.1 Hysteresis V2G

In order to develop the V2G strategy performed by means of a step-wise current profile suitable for the EV, charging stations characterised by the use of an hysteresis controller for the definition of the current set-point have been proposed. The V2G strategy, implementing such a kind of controller, has been defined *"hysteresis V2G"*. The MS synthesises the set-point P_{batt} according to (4.2) and consequently, basis on the number of plugged EVs N_{pc} and feedback information about SOC, defines the power set-point of each charging station P^k_{batt} as:

$$\begin{cases} P^k_{batt} = \frac{P_{\text{batt}}}{N} & \text{if } N = N_{\text{pc}} - N_{\text{sat}} > 0 \\ \\ P^k_{batt} = 0 & \text{if } N = 0 \end{cases} \tag{4.3}$$

where N_{sat} is the number of EVs plugged but completely charged. The charging station acts by means of the hysteresis controller in order to follow the set-point P^k_{batt} of MS. In particular, in order to improve the performance, a multi-level hysteresis regulator, characterised by an incremental output level of set-point ΔI_{batt}, has been used. Assuming constant the EV battery voltage V_{batt}, the current set-point is defined using as input the difference ε between the set-point P^k_{batt}, at the sampling time iT_s, and the feedback the DC output charging station power, P^k_{CS}.

$$\varepsilon[iT_{\mathrm{s}}] = {P_{\mathrm{batt}}}^{\mathrm{k}}[(i-1)T_{\mathrm{s}}] - {P_{\mathrm{CS}}}^{\mathrm{k}}[(i-1)T_{\mathrm{s}}] \tag{4.4}$$

The hysteresis controller varies the set-point current according to the following algorithm:

$$\begin{cases} \|\varepsilon\| < \|P_{\mathrm{th}}\| \Longrightarrow n[iT_{\mathrm{s}}] = n[(i-1)T_{\mathrm{s}}] \\ \\ \|\varepsilon\| > \|P_{\mathrm{th}}\| \Longrightarrow n[iT_{\mathrm{s}}] = n[(i-1)T_{\mathrm{s}}] \pm 1 \end{cases} \tag{4.5}$$

where n is the level of the multi-level hysteresis controller and can assume a maximum value n_{max}. Hence, the set-point current assume the output constant value:

$$I_{\mathrm{batt}}[iT_{\mathrm{s}}] = I_{\mathrm{batt}}[(i-1)T_{\mathrm{s}}] + n[iT_{\mathrm{s}}] * \Delta I_{\mathrm{batt}} \tag{4.6}$$

The number of hysteresis level $\mathrm{n_{max}}$ and the threshold power $\mathrm{P_{th}}$ characterised the dynamic evolution of the current set-point and consequently define the allowable time cycle variation of the battery, representing the degree of freedom in the management of *"hysteresis V2G"* for making it suitable for battery life cycle.

4.1.3 Scenarios and Assumptions

For the assessment of the MS performance with the proposed V2G strategies a simulation study has been developed. Considering the same MG electricity demand, the strategies performance depends on the management of the ESS. In the present

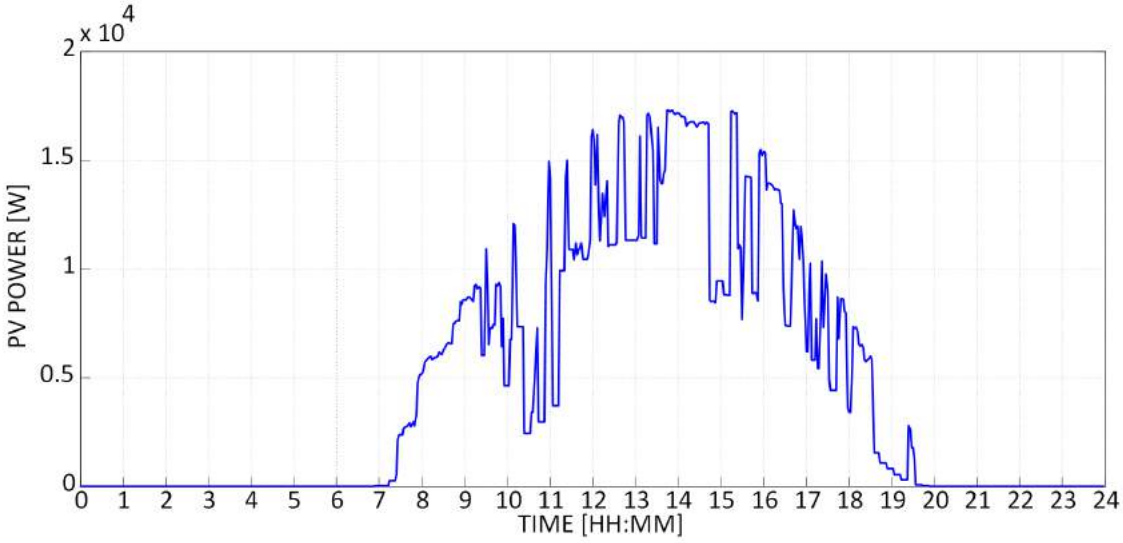

Figure 4.1.2: Total power production of the photovoltaic generators during a partially cloudy day.

case, the storage system is represented by the EV batteries and, hence, their capacity and availability are strictly connected both to the use and to the number of vehicles plugged in the MG and to the rating power of EV charging station. In the following, the details of the analysed scenarios are reported:

1. *"Continuous V2G"* strategy with one BEV plugged in the charging station at different rated power (7.4 and 22 kW);
2. *"Hysteresis V2G"* strategy with one BEV plugged in the charging station at different rated power (7.4 and 22 kW);
3. *"Hysteresis V2G"* strategy with two BEVs with the same drive path and same time scheduling at 7.4 kW rated power charging station;
4. *"Hysteresis V2G"* strategy with two BEVs with the same drive path and different time scheduling at 7.4 kW rated power charging station.

The rating power of the EV charging station has been defined referring to the commercial size available and suitable for supplying Mercedes Smart ED. As pre-

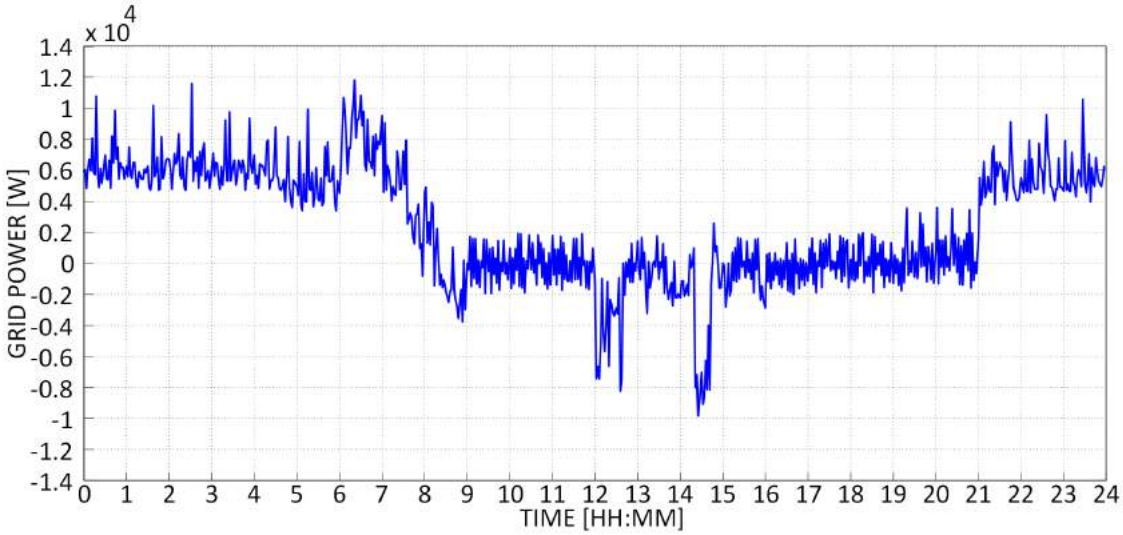

Figure 4.1.3: Residual power evolution.

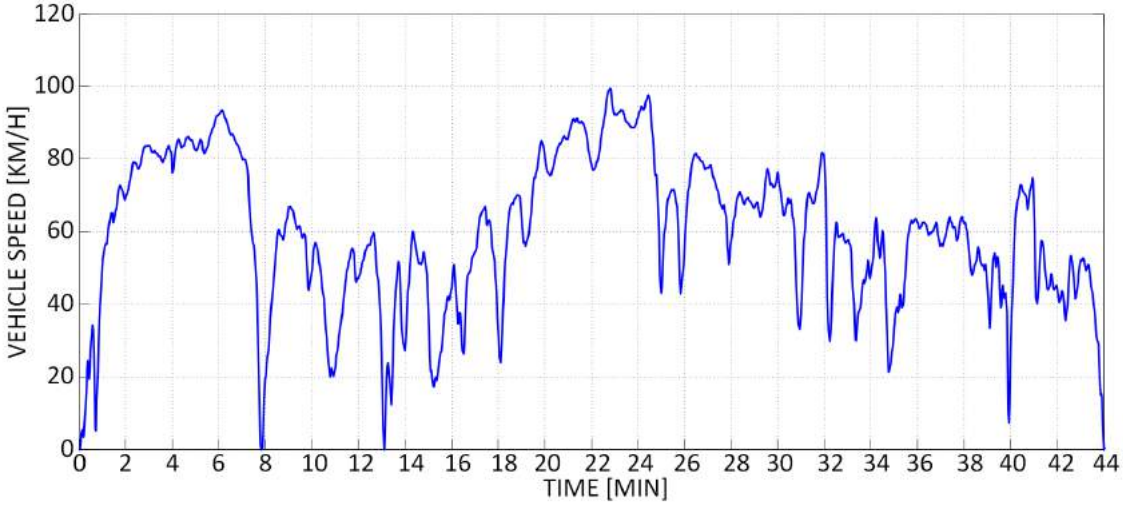

Figure 4.1.4: Typical driving cycle measured on the Mercedes Smart ED.

viously said, the MG has been modelled considering, as inputs for the simulation, the real instantaneous power production profile of PV plants reported in Fig. 4.1.2 and the respective MG demand profile in a partially cloudy day representing a sever condition for management system. The residual power evolution, obtained as difference between the production and the demand, is reported in Fig. 4.1.3. It represents the power exchanged with the main grid in order to energy balance the MG. In particular, the residual power evolution is used as input to the MS algorithm in order to perform the self-consumption maximisation by using the V2G strategies defined above. To take into account the EV mobility effects on the deployment of EV battery and to determine the initial value of the SOC at plug-in, the EV dynamic model reported in [70] has been implemented. The main parameters for the simulation of the EV are reported in Tables 3.2.2-3.2.4. The typical driving cycle measured on EV under test has been reported in Fig. 4.1.4. It is assumed that the EVs are business cars, used by the employees for the home/work paths. The charging process is enabled at 9.00 when the employees start to work. During the morning and the early afternoon, EVs are used also for service purposes, running two driving cycles which have been previously reported. In order to guarantee a defined level of autonomy for the EVs a constraint in the battery SOC has been imposed. In particular, the minimal SOC value of 40% has been imposed to the MS in order to allow the path work-home at the end of the working day.

4.1.4 Simulation Results

Firstly, the described MG has been simulated by implementing the V2G control strategies reported in scenarios 1 and 2 in the control algorithm. The power exchanged between the MG and the power system, when a charging station of 7.4 kW rating power is used, for the scenarios 1 and 2 are compared in Fig.4.1.5. It can be observed that the evolution of power in the two cases is quite similar and the differences can be ascribed to the fluctuation introduced by the hysteresis controller. It can be highlighted that the power profiles are perfectly overlapped during the EV driving cycles starting at 12.00 and 14.00 respectively. To better understand the behaviour of the MS in the resulting evolution of power exchanged with the main grid, the analysis of the SOC is necessary. In Fig. 4.1.4 is reported the comparison of

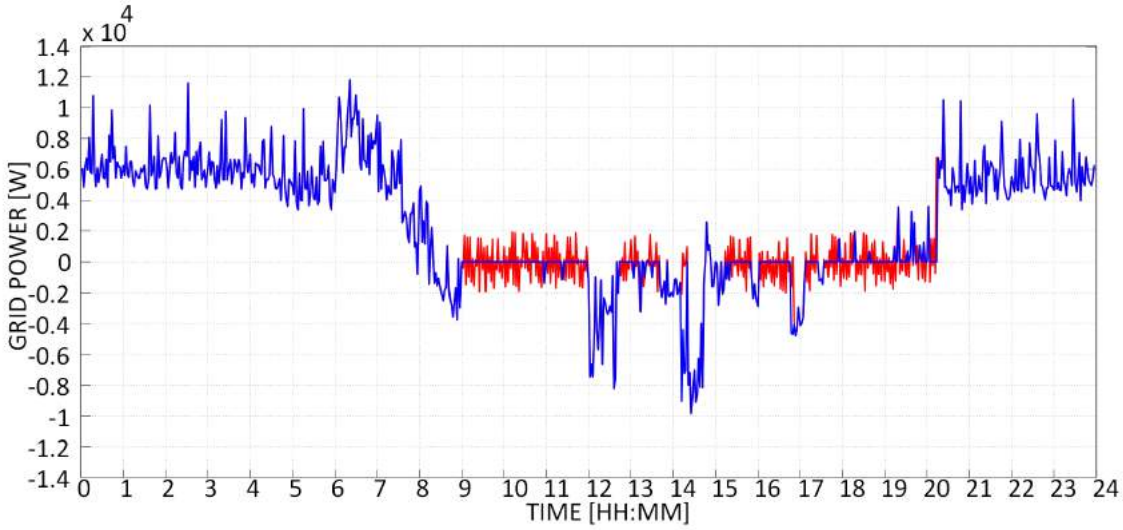

Figure 4.1.5: Comparison between the grid power evolutions in the scenario 1 "MS with continuous V2G" (blue line) and the scenario 2 "MS with Hysteresis V2G" (red line) for a 7.4 kW charging station.

SOC evolutions for the two previously cited scenarios. With regard to the scenario 1, the *"continuous V2G"* permits the reaching of a perfect balance of the production and consumption when the power managed by the V2G control algorithm is within the rated value of the charging station; otherwise, when the MG power unbalance exceeds the 7.4 kW a fluctuation in the power exchanged in the continuous V2G is observed. Moreover, when the EV battery is completely charged the MS stops the energy storage and consequently unbalance conditions occur, similar to that observed during EV driving cycles.

The same simulations have been developed considering a rated power of the charging station of 22 kW. The results are reported in Fig.s 4.1.6 and 4.1.7. The comparison between the *"continuous V2G"* and *"hysteresis V2G"* shows that it is possible to obtain the same results. However, the phenomena connected to the saturation

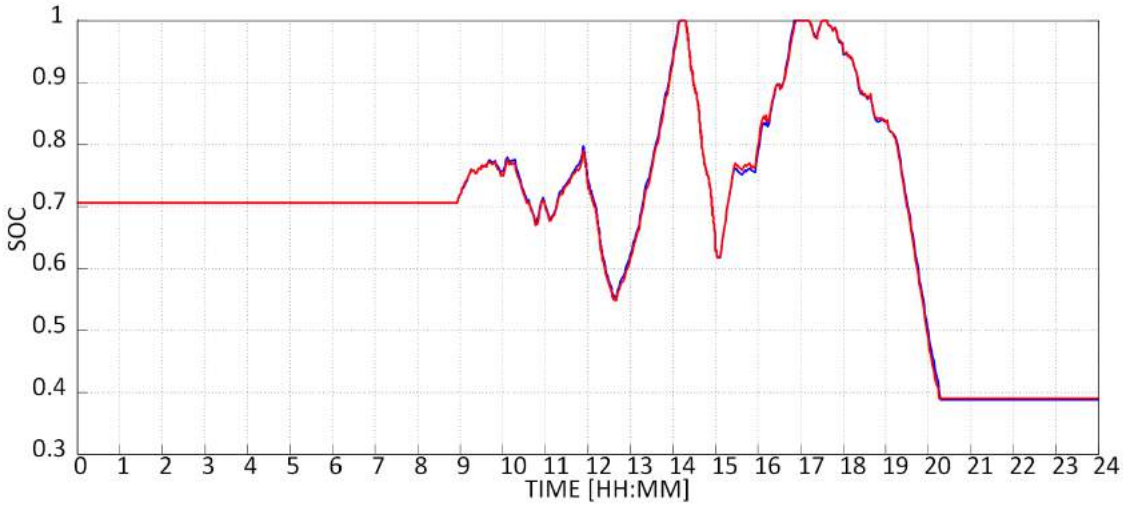

Figure 4.1.6: Comparison between the SOC profiles in the scenario 1 "MS with continuous V2G" (blue line) and the scenario 2 "MS with Hysteresis V2G" (red line) for a 7.4 kW charging station.

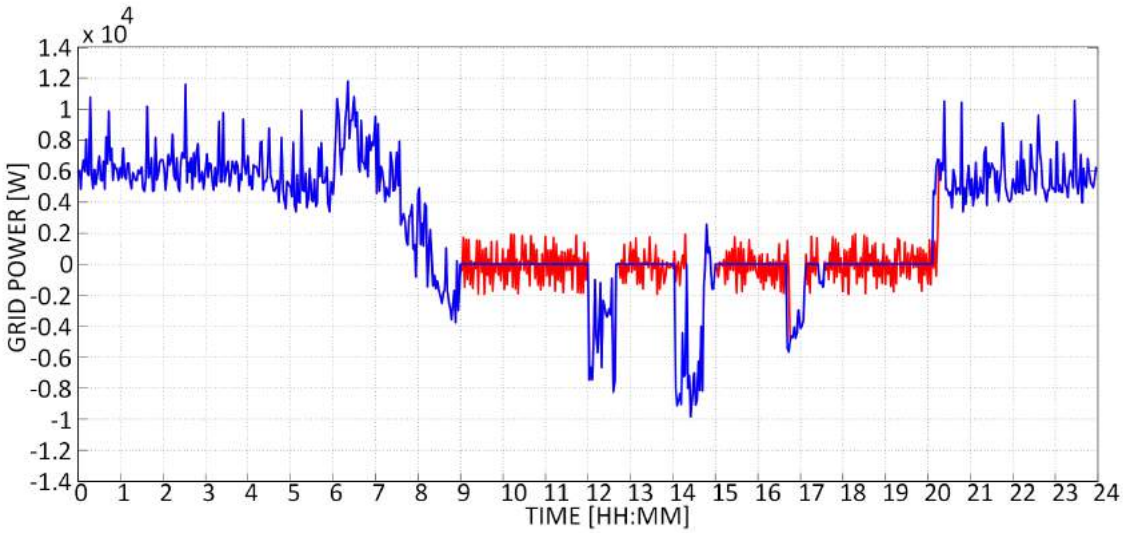

Figure 4.1.7: Comparison between the grid power evolutions in the scenario 1 "MS with continuous V2G" (blue line) and the scenario 2 "MS with Hysteresis V2G" (red line) for a 22 kW charging station.

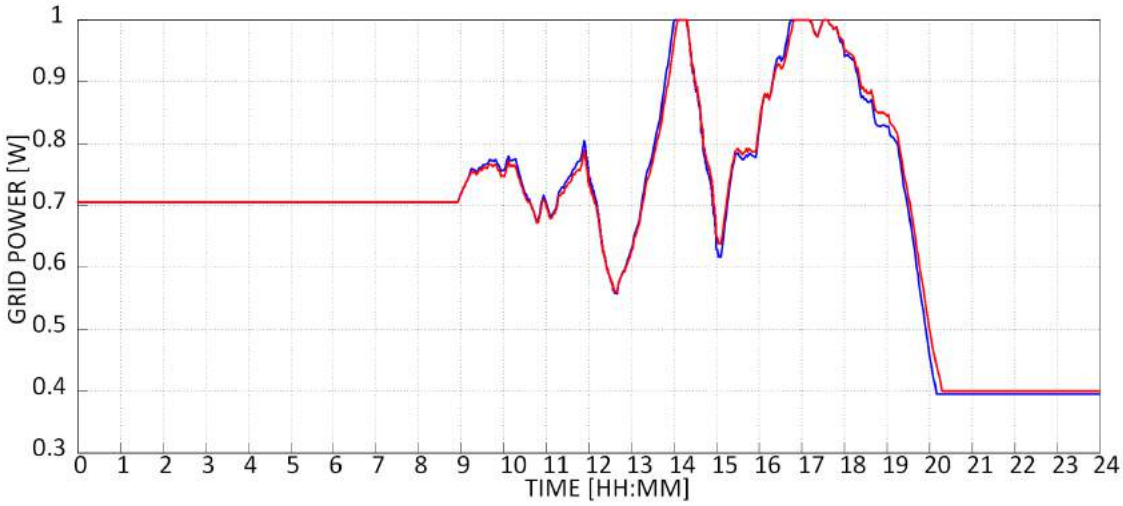

Figure 4.1.8: Comparison between the SOC profiles in the scenario 1 "MS with continuous V2G" (blue line) and the scenario 2 "MS with Hysteresis V2G" (red line) for a 22 kW charging station.

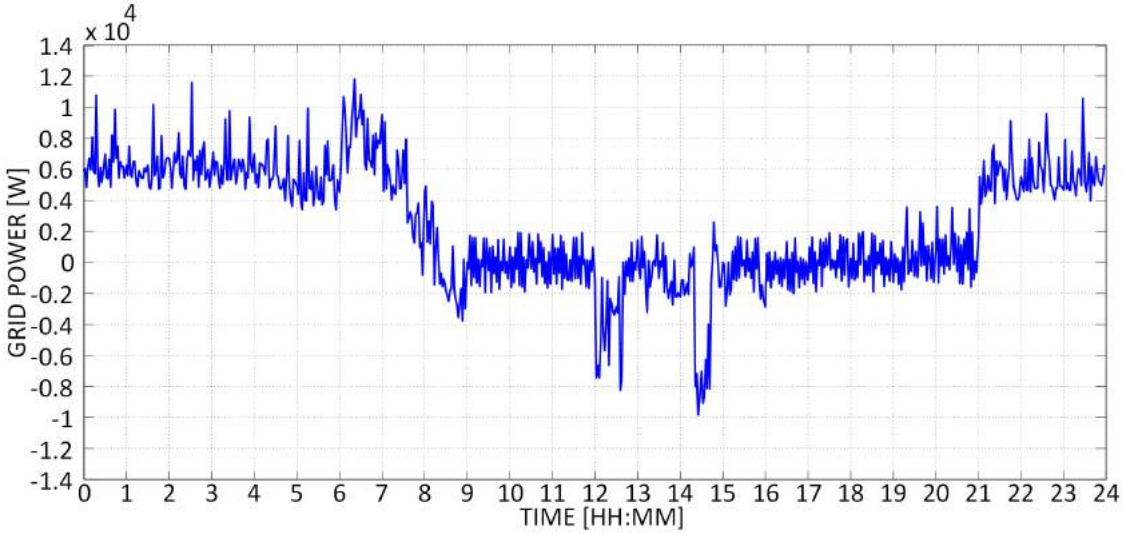

Figure 4.1.9: Grid power evolution in the scenario 3 "MS with Hysteresis V2G" considering two BEVs with the same EV mobility scheduling and a 7.4 kW charging station.

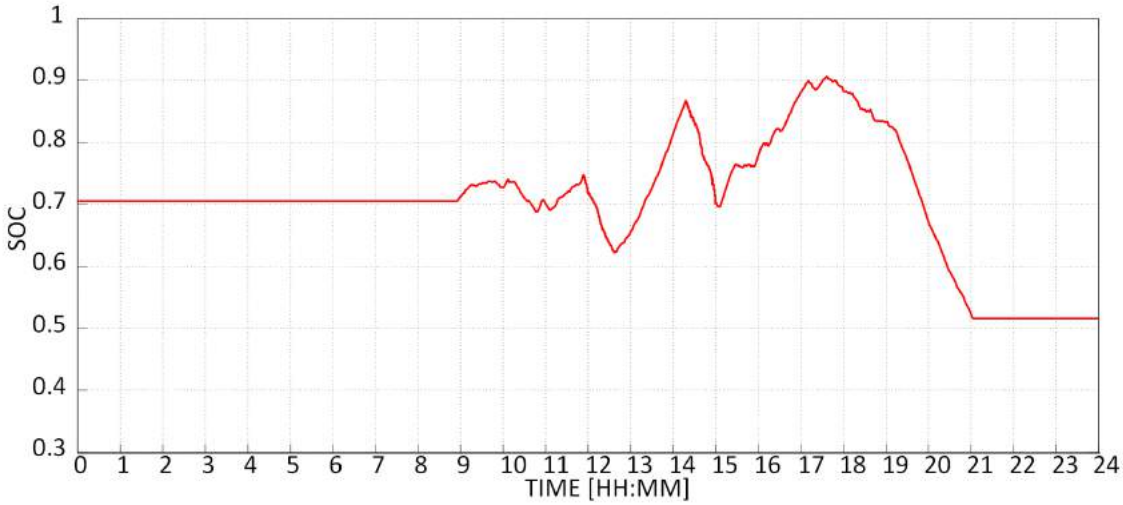

Figure 4.1.10: SOC evolution in the scenario 3 "MS with Hysteresis V2G" considering two BEVs with the same EV mobility scheduling and a 7.4 kW charging station.

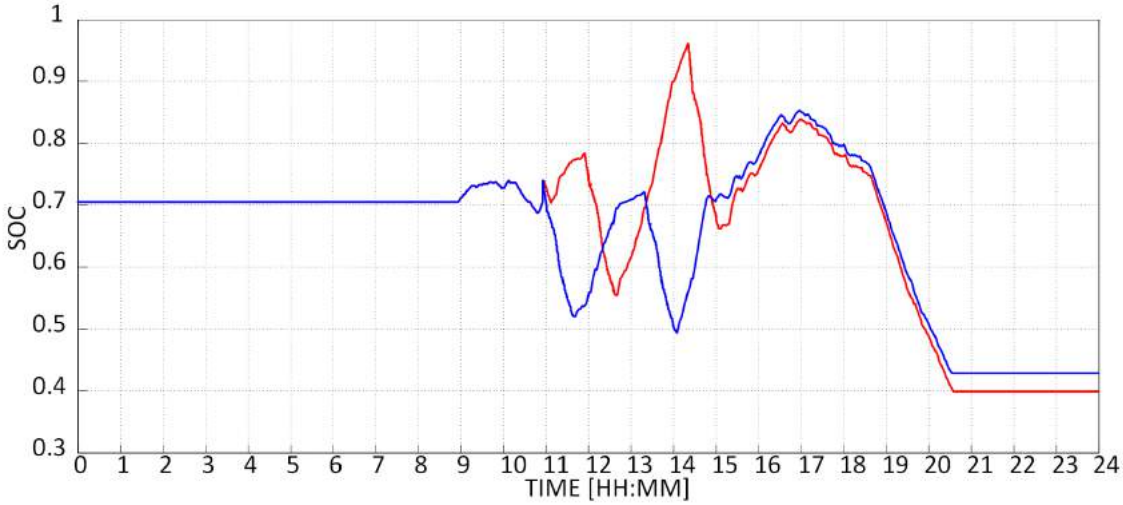

Figure 4.1.11: SOC evolution in the scenario 4 "MS with Hysteresis V2G" considering two BEVs with different time schedules and a 7.4 kW charging station.

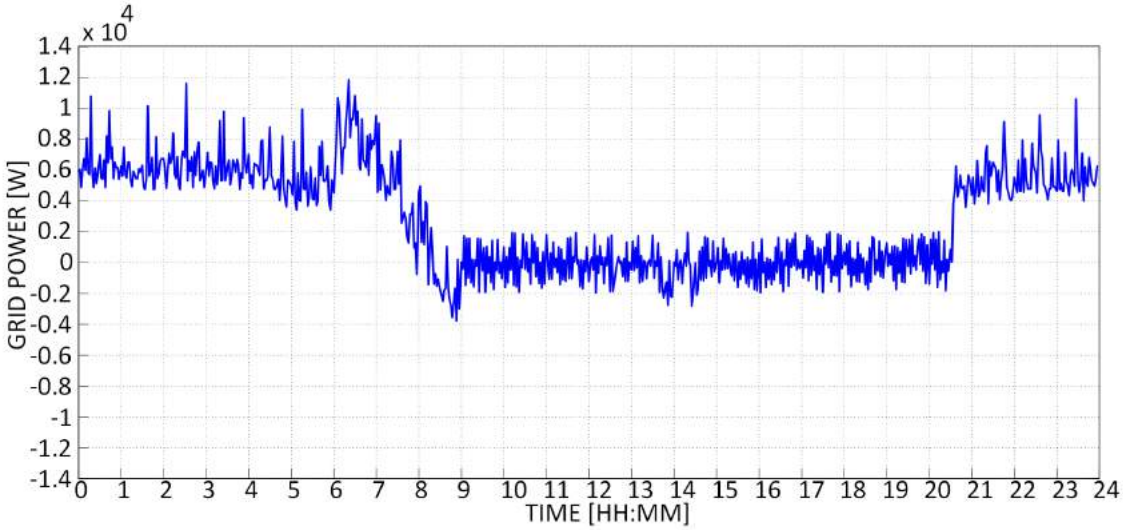

Figure 4.1.12: Grid power evolution in the scenario 4 "MS with Hysteresis V2G" (red line) considering two BEVs with different time schedules and a 7.4 kW charging station.

and the unplugging of the EVs due to the mobility service development still occur. Moreover, the comparison of the *SOC* traces associated to the scenarios 1 and 2, when 22 kW charging station is used, highlights a mismatching due to the magnification of the hysteresis effect connected to charging station power rating increase. Hence, considering that the *"hysteresis V2G"* behaves in the same manner of *"continuous V2G"*, apart the power fluctuation associated to the hysteresis controller, the analysis of scenarios 3 and 4 has been developed in order to evaluate the effects of capacity enhancement and management associated to the variation of EVs number and of EVs trip time-scheduling. The results are reported in Fig.s 4.1.8-4.1.12. In particular, Fig.s 4.1.9-4.1.10 refer to scenario 3 in which two EVs with the same time-scheduling trip has been considered. The results put in evidence that phenomena connected to the unplugging still occur. The advantage of this solution is that the *SOC* of the two vehicles does not reach the saturation condition. Thus MS can manage the MG assuring the self-consumption when the EVs are connected and as long as charging socket is enabled. The positive effect of planned time-scheduling in EV usage is pointed out in the scenario 4. In Fig.s 4.1.11- 4.1.12 are reported the power drawn from the main grid and the *SOC* of the two EVs. Fig.4.1.12 shows that the self-consumption in the MG is maintained continuously when at least one

EV is plugged and the lower SOC constraint is not reached.

In conclusion, this study highlights that a suitable MS can provide the MG requirements without impair the driver needs. Moreover, an adequate EVs time-scheduling can maximize the MG energy self-consumption, by maintaining continous the exploitation of the RES during the working day. Finally, this work demonstrates that the V2G concept, that is the employment of EVs for grid support purposes, is a real possibility inside the smart grid concept thanks to the adoption of correct MSs that allow the EVs exploitation both for mobility and for V2G operations.

4.2 Energy Stationary Systems

As previously reported, the integration of ESSs in RES power plants is considered a key topic in order to guarantee the harmonious development of Distributed Generation in the actual power system. On the other hand, in some European countries, such as Germany and Italy, the development of RES has been particularly significant in terms of installed power. Hence, the criticality and the cost connected to the power quality standards satisfaction has made Distributed Storage System (DSS) a viable solution. The planned actions to stimulate the diffusion of DSSs are different in Germany and Italy. In Germany, the government subsidizes the installation of battery systems to store electrical energy from PV power, whereas in Italy the Energy Authority has introduced novel electricity market rules oriented to involve the RES power plant in ancillary services. In particular, referring to the one-day-ahead scheduled node production, the energy cost of balancing service (if energy is not delivered) is defined considering the market zone level of unbalancing. This means that the correct matching between actual and scheduled production has an economic value [102]. In this last case, the additional cost connected to the energy forecasting error could be compensated by means of a DSS oriented to make the electricity production of intermittent power plants programmable with minimum mean errors [93]. In these novel scenarios, an ESS able to upgrade installed PV power plant represents a suitable solution to make the current solar energy production dispatchable and programmable. In addition, the high variability and intermittency power production can represent an obstacle to the development of novel solar technology,

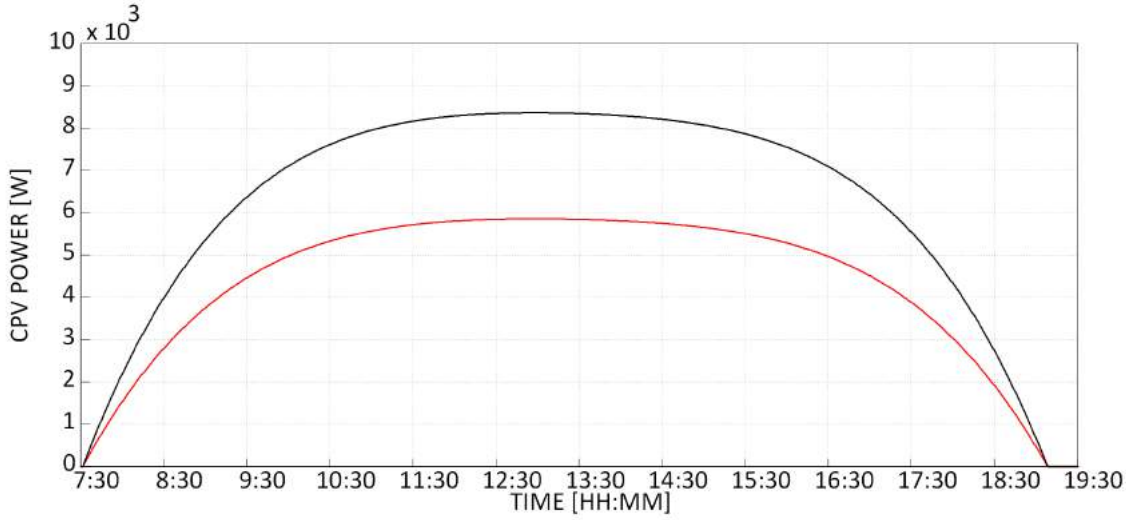

Figure 4.2.1: The DNI (black) and the corresponding power profile (red) of the CPV power plant on June 21.

such as CPV systems. In fact, as widely reported in Chapter 2, although the CPV technology is characterized by the highest efficiency among solar energy conversion systems, it has an intrinsic variability connected both to the conversion of the DNI and to the requirement of correcting and continuously aligning the photoactive area with the sunrays. In this case, the use of ESS represents, for CPV power plant, a mandatory choice to overcome the future constraints associated to the power quality.

4.2.1 MG Description

The considered MG is the same reported in Section 4.1.1. Moreover, a CPV power plant and an ESS are installed. The proposed CPV-ESS configuration is schematically depicted in Fig. 4.2.2. Particularly, the ESS consists of Lithium-ion batteries, whose charging/discharging process has to be power-managed in accordance with the voltage and current constraints and the reference power profile provided by the MS. This is accomplished by means of a bidirectional DC-DC buck-boost converter (BDC), which has to properly interface the ESS with the DC node. This last is linked to the CPV power plant through a DC-DC converter, which is employed for

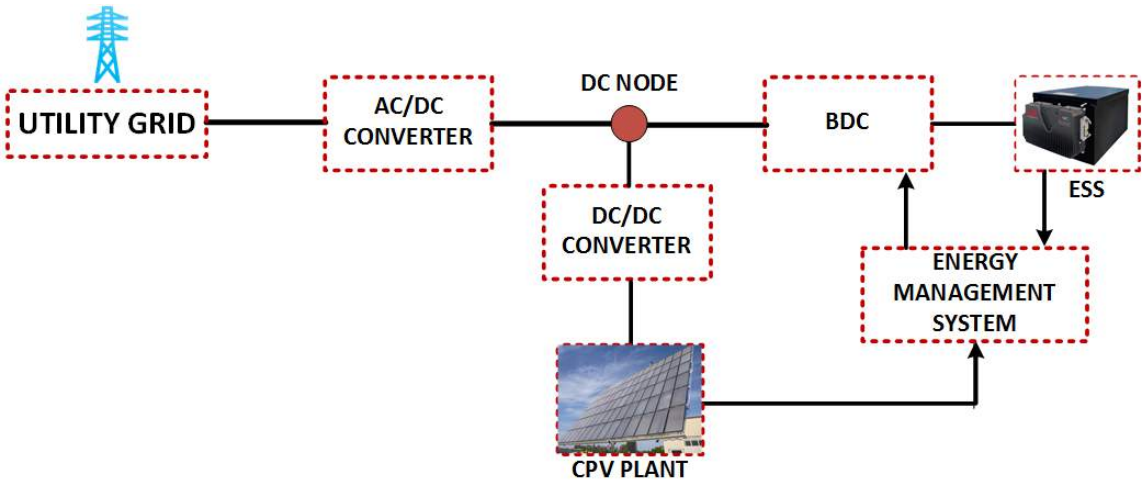

Figure 4.2.2: Schematic layout of the proposed CPV-ESS configuration.

guaranteeing Maximum Power Point Tracking (MPPT). Finally, the DC node exchange energy with the main grid by means of a DC/AC converter, as shown in Fig. 4.2.2.

4.2.2 Battery Sizing

In order to be able to develop the CPV-ESS management strategy, the definition of the ESS capacity is a key topic. Considering the high cost of electrochemical energy storage systems, the battery design for the proposed configuration has been developed in order to determine the minimum capacity that guarantees the tracking of the scheduled output power profile. This last has been defined in accordance with the CPV power production profile, particularly its shape has been chosen considering both the needs of battery size minimization and flat-programmable output power profiles. Thus, the worst situation in terms of battery capacity demand, i.e. the clear sky condition, in correspondence of which the daily CPV energy production assumes its maximum values, has been taken into account. Consequently, the corresponding flat-programmable output power profile is considered (P_{NODE}), as shown in Fig. 4.2.3. Particularly, P_{NODE} leads to a sequence of battery charging and discharging time intervals, which are bounded by the switching instants highlighted in Fig. 4.2.3.

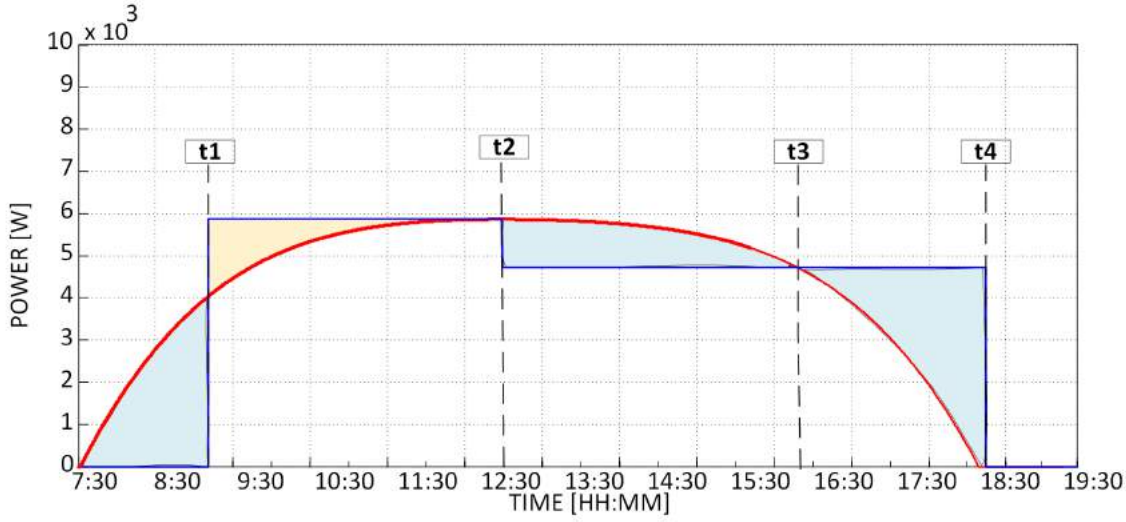

Figure 4.2.3: The ESS charging (blue) and discharging (orange) areas related to the CPV power production (red) and the corresponding flat-programmable output power profile (blue).

Over each time interval, the battery provides or draws the power P_{batt}, in accordance with the time evolution of the CPV power production (P_{CPV}) and to the scheduled output power profile (P_{NODE}). Particularly, P_{batt} can be modeled by means of (4.7), where η_{conv} is the DC/DC buck-boost converter efficiency:

$$P_{\text{batt}} = \begin{cases} \frac{P_{\text{NODE}} - P_{\text{CPV}}}{\eta_{\text{conv}}} & \text{if } (P_{\text{NODE}} - P_{\text{CPV}}) > 0 \\ \eta_{\text{conv}} * (P_{\text{NODE}} - P_{\text{CPV}}) & \text{if } (P_{\text{NODE}} - P_{\text{CPV}}) < 0 \end{cases} \tag{4.7}$$

Hence, the corresponding energy provided/drawn by the battery (E_{batt}) can be evaluated by (4.8):

$$E_{\text{batt}} = \int_t P_{\text{batt}} dt \tag{4.8}$$

The energy model of the CPV-ESS allows the sizing of the battery capacity by considering the SOC constraints reported in (4.9)-(4.11), when the maximum CPV electricity production occurs:

$$SOC_{\text{t=0}} = SOC_{\text{t=t}_4} = 0.2 \tag{4.9}$$

$$SOC_{t=t_2} = 0.5 \tag{4.10}$$

$$SOC_{t=t_3} = 1 \tag{4.11}$$

The above considerations has led to the definition of the ESS capacity, which has been set equal to 6.6 kWh. In addition, the battery chemistry has been selected considering different needs, such as safety, lifecycle time, power and energy densities and the final cost [75]. As a consequence, a Lithium Iron Phosphate (LFE) battery has been chosen. The battery rated voltage has been set to 360 V based on the DC link voltage range of the CPV. Finally, in order to correctly represent the ESS behavior in particular when unexpected changes of P_{batt} occur, the dynamic electric battery model reported in 3.1.3 has been considered.

4.2.3 MS Description

The choice of the battery capacity design for the proposed CPV-ESS power system required the definition of a shape of the daily scheduled output power. The following step is the development of the MS that allows the automatic definition of the most suitable battery power profile in order to preserve the daily energy balance. Furthermore, the MS has to be able to compensate for the unpredictable power fluctuations that occur in CPV power plants. To reach this goal, an MS based on a one-day-ahead power scheduling and real-time control algorithm has been developed.

Firstly referring to the scheduling procedure, the base CPV power profile is determined one-day-ahead based on the geographical position of the CPV power plant, as well as on the date and characterization studies [103]. As a result, assuming a clear sky condition, the astronomic evaluation of daily DNI evolution can be achieved, based on which the reference profile is easily determined. This allows both the scheduling of the output power profile and the evaluation of the corresponding SOC time evolution, by satisfying all the battery constraints expressed in (4.9)-(4.11), as shown in Fig. 4.2.4. Furthermore, starting from the base CPV power production profile and referring to the sky octa definition, additional CPV profiles are introduced in order to take into account forecasting uncertainties. In particular, two

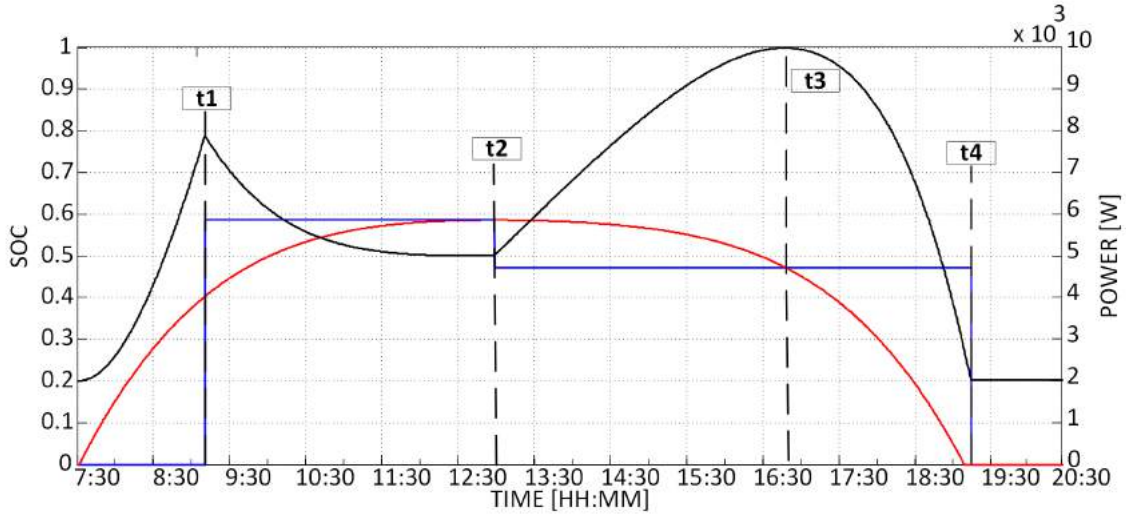

Figure 4.2.4: The SoC time evolution (black line) by considering the CPV power production on a clear sky (red curve) and the corresponding flat-programmable power profile (blue line).

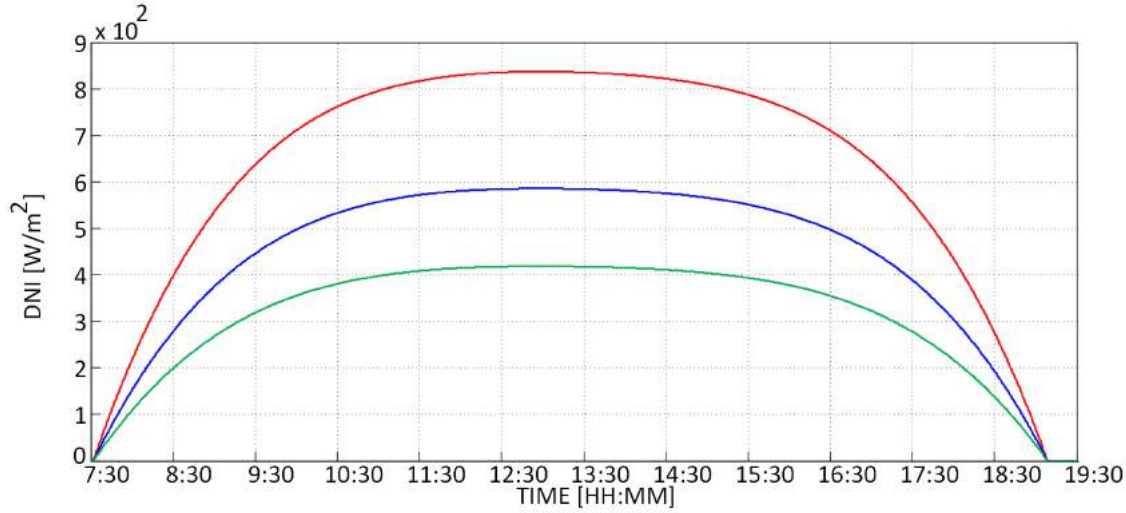

Figure 4.2.5: Base and addtional CPV power profiles scheduled one-day-ahead: clear sky condition (red), 70% (blue) and 50% (green).

other CPV power profiles have been considered [103], whose magnitudes correspond to 70% and 50% of the reference one, as shown in Fig. 4.2.5. Consequently, the corresponding scheduled output power profiles and SOC evolutions can be evaluated, refering to different scenarios. Regarding to the real-time control algorithm, this is developed with the aim of assuring the most suitable output power profile in accordance with those synthesized one-day-ahead. Particularly, referring to Fig. 4.2.4, the output power profile is set to zero at first, thus the CPV power production is used for charging the ESS. As soon as t_1 is reached, the actual SOC value is compared with all those estimated one-day-ahead in the same time instant. Consequently, the scheduled SOC value nearest to the actual one can be identified, thus the corresponding scheduled output power profile is chosen as the reference one. As a result, the scheduling procedure allows the switching among different scheduled output power profiles depending on the feedback information of the actual SOC. Once the reference output power profile has been set, the ESS controller supervises the SOC evolution continuously in order to take into account unpredictable severe weather conditions. In fact, in such cases, switching between the different scheduled output power profiles may be required in accordance with SOC evolutions. In this context, it is worth noting that the ESS controller also compares the actual CPV power production profile with the reference one in order to account for future SOC trend, thus avoiding unsuitable switching phenomena.

4.2.4 Simulation and Results

The proposed MS is tested referring to two cases study, which are based on the CPV power plant described in [103]. Regarding the first case, a DNI profile corresponding to cloudy weather conditions has been considered and shown in Fig. 4.2.6. As a consequence, the CPV electricity generation is characterized by significant fluctuations because CPV power plants are more sensitive to weather conditions than the other photovoltaic technologies, revealing the need of being combined with ESS. The proposed MS has been modelled in Matlab, as well as the proposed CPV-ESS configuration. Particularly, the MS has to ensure a flat-programmable output

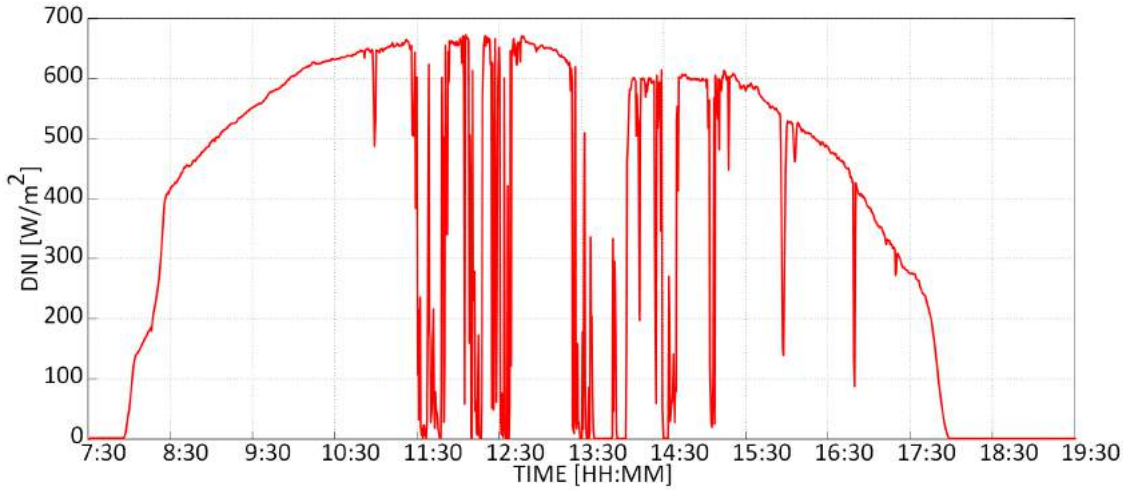

Figure 4.2.6: DNI evolution considered for the case study.

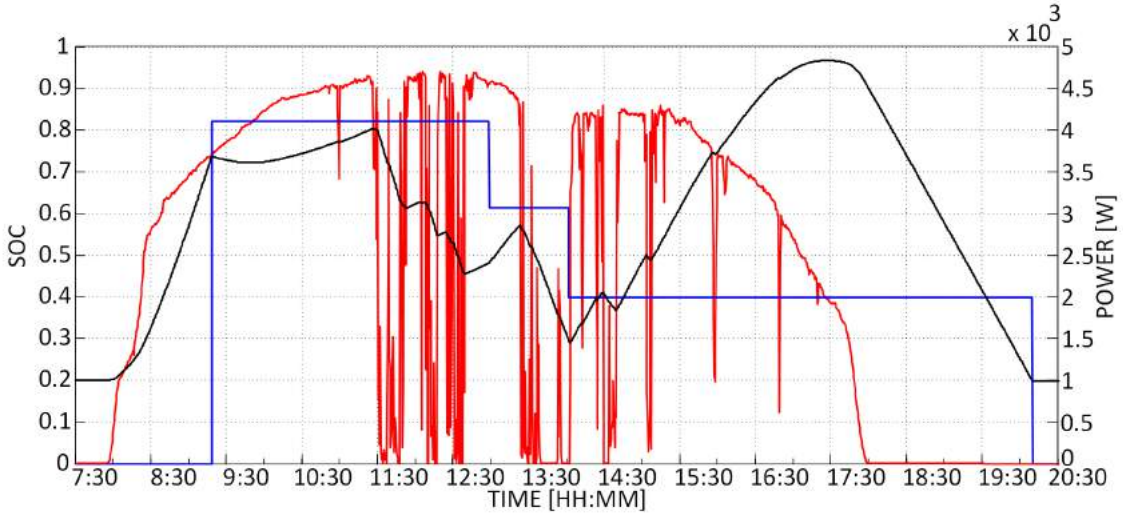

Figure 4.2.7: Simulation results: CPV power (red), output power (blue) and SoC (black) evolutions.

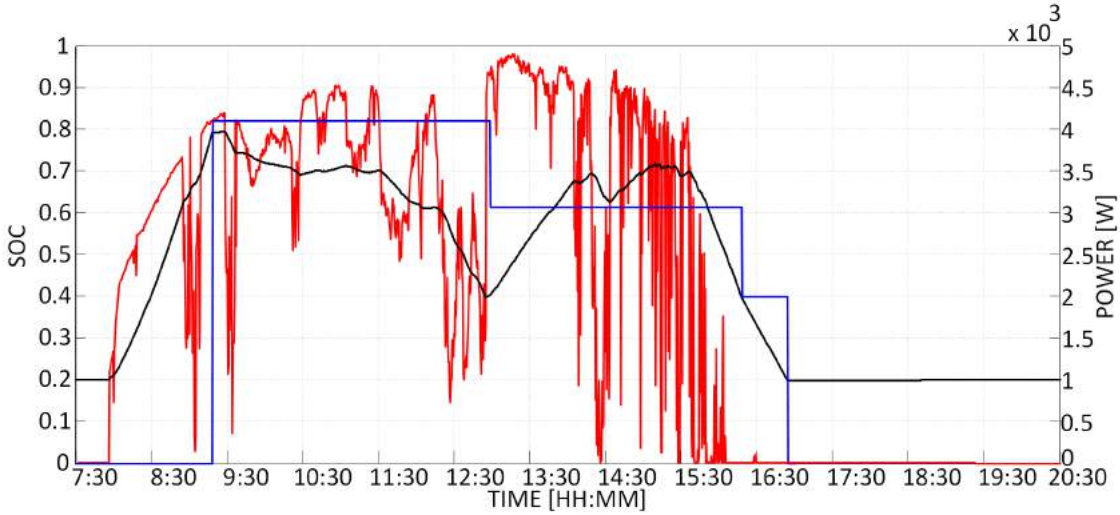

Figure 4.2.8: Simulation results (second case): CPV power (red), output power (blue) and SoC (black) evolutions.

power profile, by compensating for CPV power production variation due to severe weather conditions at the same time. The MS successfully guarantees an output flat-programmable power profile during the overall day, in spite of the high fluctuations of the DNI related to the cloudy weather condition, as depicted in Fig. 4.2.7. In order to highlight the effectiveness of the proposed solution, a second case, reported in Fig. 4.2.8, has been considered. It is characterized by weather conditions worse than the previous one. As one can observe, in correspondence of both cases, the designed ESS is able to provide all the reference power at the interconnection node, even when the CPV production drops dramatically. In conclusion, it can be stated that simulation results confirm the feasibility of the proposed CPV-ESS configuration, as well as that of the proposed MS.

In conclusion, the two developed MSs highlight the importance of an accurate planning in the management of a MG in order to better exploit the RESs installed, such as CPV plants characterized by a strong unpredictability of the power production. In the first case, the MS has allowed to maximize the energy self-consumption of the MG, by correctly planning the time scheduling of a BEV fleet without impair the driver needs. Regarding the second case, the MS has provided a flat-programmable power profile to the main grid thanks to an adequate sizing of a stationary storage

system that compensates the uncertainty power production of the CPV plant.

Conclusions

The PhD dissertation has introduced two new management strategies in a microgrid composed by office and laboratory loads, a concentrating photovoltaic (CPV) plant and a traditional flat-plate PV by considering a BEV fleet and a stationary energy storage system, respectively. With the aim to correctly define the MSs, the most important components of the MGs have been analyzed, that are photovoltaic and energy storage systems (ESSs) and electric vehicles (EVs). In particular, the CPV technology have been taken into account due to the fact that represents the most promising new technology for improving the efficiency of PV systems as well as the most complex. CPV system complexity is precisely related to several parameters, such as environmental factors, tracking errors and optical misalignment. Thus, an accurate characterization is mandatory in order to point out the operating critical aspects of the considered system. In particular, a deeper knowledge of the real behavior of a CPV module and of the influence of weather parameters is fundamental to develop a suitable management strategy, in order to guarantee the reliability and the controllability of the MG. In fact, the RESs and particularly CPV plants represent a challenge for the management of a MG because of their poor predictablity. Regarding this lack, CPV plants are combined inside the MG with ESSs that allow to store the CPV surplus energy during sunny days and to supply the MG when the CPV production is poor due to adverse environmental conditions. Moreover, nowadays, the introduction of the V2G paradigm has represented a fundamental innovation for the power grid, because EVs can be considered as *distributed energy storage* whose employment leads to stabilize the fluctuations introduced by RESs and to improve their exploitation. Thus, an accurate model that reproduces the battery behavior under real dynamic driving conditions is mandatory, not only to validate

it but also because the EV modelling allows to make the EV feedback information reliable for managing correctly and profitably an EV fleet inside a MG. Consequently, in relation to the above consideratios, the MS inside a MG with RESs (CPV and PV plants) and EVs or ESSs is fundamental to guarantee the stability and the reliability of the MG. In the last part of the dissertation two MSs are presented. The former operates in a MG composed by office and laboratory loads, a CPV plant and a traditional flat-plate PV one and a BEV fleet. The second MS manages the same MG by employing a stationary storage system instead of a BEV fleet. The two developed strategies highlight the importance of an accurate planning in the management of a MG in order to better exploit the RESs installed, such as CPV plants characterized by a strong unpredictability of the power production. In the first case, the study has highlighted that a suitable MS can provide the MG requirements without impair the driver needs. Moreover, an adequate EVs time-scheduling can maximize the MG energy self-consumption, by maintaining continous the exploitation of the RES during the working day. Finally, it demonstrates that the V2G concept, that is the employment of EVs for grid support purposes, is a real possibility inside the smart grid concept thanks to the adoption of correct strategies that allow the EVs exploitation both for mobility and for V2G operations. Regarding the second case, simulation results confirm the feasibility of the proposed CPV-ESS configuration, as well as that the EMS successfully guarantees an output flat-programmable power profile during the overall day, in spite of the high fluctuations of the irradiation related to the cloudy weather condition.

In conclusion, the PhD dissertation shows that a suitable management strategy inside a MG allows to accomplish several benefits and, consequently, promotes the advancement of the future smart grid concept. Moreover, the developed BEV model is suitable for being used by smart phone systems as feedback devices for an EV aggregator service provider and consequently to be implemented both in smart city and in a MG for the integration and management of EVs charging infrastructure into the main grid.

Bibliography

[1] Gao, D. (2015) *Energy storage for sustanable microgrid*, Elsevier.

[2] Department of energy office of electricity delivery and energy reliability (2012) "Summary report: 2012 DOE Microgrid workshop," .

[3] Schwaegerl, C. and L. Tao (2014) *Microgrids: architectures and control*, Wiley&Sons.

[4] Bacha, S., D. Picault, B. Burger, Etxeberria-Otadui, and J. Martins (2015) "Photovoltaics in Microgrids," *The Industrial Electronics*, pp. 33–46.

[5] Riffonneau, Y., S. Bacha, F. Barruel, and S. Ploix (2011) "Optimal Power Flow Management for Grid Connected PV Systems With Batteries," *Sustainable Energy*, pp. 309–320.

[6] Riffonneau, Y., S. Bacha, F. Barruel, Y. Baghzouz, and E. Zamaï (2012) "Optimal reactive supervision of grid connected PV systems with batteries in real conditions," *International Review of Electrical Engineering*, pp. 4607–4615.

[7] Salameh, Z. (2014) *Renewable Energy System Design*, Elsevier.

[8] Kalogirou, S. A. (2009) *Solar Energy Engineering*, Elsevier.

[9] Fraunhofer Institute for Solar Energy Systems ISE (2015) *Photovoltaics Report*.

[10] Blazev, A. S. (2011) *Photovoltaics for Commercial and Utilities Power Generation*, Fairmont Press.

[11] NREL, http://www.nrel.gov/ncpv/.

[12] Philipps, S., A. W.Bett, K. Horowitz, and S. Kurtz (2015) *Current Status of Concentrator Photovoltaic (CPV) Technology*, Fraunhofer ISE/NREL.

[13] Ahuja, S. (2015) *Food, Energy, and Water*, Elsevier.

[14] Boicea, V. (2014) "Energy Storage Technologies: The Past and the Present," *Proceedings of the IEEE*, **102**, pp. 1777–1794.

[15] Yonga, J. Y., V. K. Ramachandaramurthya, K. M. Tana, and N. Mithulananthanb (2015) "A review on the state-of-the-art technologies of electric vehicle, its impacts and prospects," *Renewable and Sustainable Energy Reviews*, **49**, pp. 365–385.

[16] Manzetti, S. and F. Mariasiuc (2015) "Electric vehicle battery technologies: From present state to future systems," *Renewable and Sustainable Energy Reviews*, **51**, pp. 1004–1012.

[17] Barreras, F., M. Maza, and A. e. a. Lozano (2012) "Design and development of a multipurpose utility AWD electric vehicle with a hybrid powertrain based on PEM fuel cells and batteries," *International Journal of Hydrogen Energy*, pp. 15367–15379.

[18] Damiano, A., G. Gatto, I. Marongiu, M. Porru, and A. Serpi (2014) "Vehicle-to-grid technology: State-of-the-art and future scenarios," *Journal of Energy and Power Engineering*, pp. 152–165.

[19] Musio, M. and A. Damiano (2014) "Analysis of vehicle to grid and energy storage integration in a virtual power plant," in *Conference of the Industrial Electronics Society (IECON)*, pp. 3094–3100.

[20] Mureddu, M., M. Musio, A. Scala, A. Chessa, G. Caldarelli, and A. Damiano (2014) "An agent based approach for the development of ev fleet charging strategies in smart cites," in *International Electric Vehicle Conference (IEVC)*, pp. 1–8.

[21] Damiano, A., I. Marongiu, M. Porru, and A. Serpi (2012) "Electric Vehicle energy storage management for Renewable Energy Sources exploitation," in *IEEE International Electric Vehicle Conference (IEVC)*, pp. 1–8.

[22] Musio, M., P. Lombardi, and A. Damiano (2010) "Vehicles to grid (V2G) concept applied to a Virtual Power Plant structure," in *The XIX International Conference on Electrical Machines (ICEM)*, pp. 1–6.

[23] Zhan, W., B. Zoghi, and M. Hasan (2009) "Requirement development for electrical vehicles using simulation tools," *World Congress on Engineering and Computer Science*, pp. 932–937.

[24] Martinez, M., O. De la Rubia, F. Rubio, and P. Banda (2012) *Comprehensive Renewable Energy*, Elsevier.

[25] Sala, G. (2012) *Handbook of Photovoltaics*, Elsevier.

[26] Kinsey, G., W. S. Bagienski, A. Nayak, M. Liu, R. Gordon, and V. Garboushian (2013) "Advancing efficiency and scale in CPV arrays," *Journal of Photovoltaics*, pp. 873–878.

[27] Green, M. A., K. Emery, Y. Hishikawa, W. Warta, and E. D. Dunlop (2013) "Solar cell efficiency tables (version 42)," *Prog. Photovolt: Res. Appl.*, pp. 827–837.

[28] Damiano, A., I. Marongiu, C. Musio, and M. Musio (2013) "Outdoor Characterization of a Cassegrain-type Concentrator Photovoltaic Receiver," in *39th Annual Conference of the IEEE Industrial Electronics Society (IECON)*, pp. 8110–8115.

[29] Domínguez, C., S. Askins, I. Antón, and G. Sala (2009) "Characterization of five CPV module technologies with the Helios 3198 solar simulator," in *Photovoltaic Specialists Conference (PVSC)*, pp. 1004–1008.

[30] Muller, M. (2009) "Development of an Outdoor Concentrating Photovoltaic Module Testbed, Module Handling and Testing Procedures, and Initial Energy Production Results," *Technical Report NREL*, pp. 1–23.

[31] CEI "CEI 82-25; V1 - Guide for design and installation of photovoltaic (PV) systems connected to MV and LV networks," .

[32] Jaus, J. and G. e. a. Peharz (2009) "Development of Flatcon® modules using secondary optics," in *34th IEEE Photovoltaic Specialists Conference (PVSC)*, pp. 1931–1936.

[33] Musio, M., C. Musio, C. Sanna, M. Gawronska, and A. Damiano (2014) "Characterization of a CPV module prototype for design and performance improvement," in *International Energy Conference (ENERGYCON)*, pp. 929–936.

[34] Musio, M., T. Pisanu, C. Musio, and A. Damiano (2012) "A Concentrator Photovoltaic Prototype: Realization and Characterization," in *27th European Photovoltaic Solar Energy Conference and Exhibition (PVSEC)*, pp. 218–223.

[35] IEC "IEC 62670-1: Photovoltaic concentrators (CPV) – Performance testing - Part 1: Standard conditions," .

[36] Garcia, I. and P. e. a. Espinet (2011) "Analysis of chromatic aberration effects in triple-junction solar cells using advanced distributed models," in *37th IEEE Photovoltaic Specialists Conference (PVSC)*.

[37] IEC "IEC 62108: Concentrator photovoltaic (CPV) modules and assemblies - Design qualification and type approval," .

[38] Stafford, B., M. Davis, J. Chambers, M. Martinez, and Sànchez (2009) "Tracker accuracy: field experience analysis, and correlation with me-

tereological conditions," in *Photovoltaic Specialists Conference (PVSC)*, pp. 2256–2259.

[39] Fernandez, E. F., P. P. Higueras, A. J. Garcia Loureiro, and P. G. Vidal (2012) "Outdoor evaluation of concentrator photovoltaic systems modules from different manufacturers: first results and steps," *Progress in Photovoltaics: Research and Applications*, pp. 693–701.

[40] Cotal, H. and C. e. a. Fetzer (2009) "III-IV multijunction solar cells for concentrating photovoltaics," *Energy Environment Science*, pp. 174–192.

[41] Segev, G., A. Mittelman, and A. Kribus (2012) "Equivalent circuit models for triple-junction concentrator solar cells," *Solar Energy Materials and Solar Cells*, pp. 57–65.

[42] Bouzidi, K. and M. Chegaar (2007) "Solar cells parameters evaluation considering the series and shunt resistance," *Solar Energy Materials and Solar Cells*, pp. 1647–1650.

[43] Herrero, R., M. Victoria, C. Domìnguez, S. Askins, I. Antòn, and G. Sala (2011) "Concentration photovoltaic optical system irradiance distribution measurement and its effect on multi-junction solar cells," *Progress in Photovoltaics: Research and Applications*, pp. 423–430.

[44] Algora, C., M. Baudrit, I. Rey-Stolle, D. Martìn, R. Pena, B. Galiana, and J. Gonzàlez (2005) "Pending issues in the modeling of concentrator solar cells," *The Simulation Standard Journal*, pp. 1–5.

[45] Garcia, I., C. Algora, I. Rey-Stolle, and B. Galiana (2008) "Study of non-uniform light profiles on high concentration IIIV solar cells using quasi-3D distributed models," in *33rd IEEE Photovoltaic Specialists Conference*, pp. 1–6.

[46] Pisanu, T., A. Damiano, P. Buttu, M. Musio, C. Pernechele, and G. Gatto (2011) "An optical concentrator system to perform a light-soaking indoor test on photovoltaic receivers," in *26th European Photovoltaic Solar Energy Conference and Exibition (PVSEC)*, pp. 681–685.

[47] Chemisana, D., A. Vossier, L. Pujol, A. Perona, and A. Dollet (2011) "Characterization of Fresnel lens optical performances using an opal diffuser," *Energy Conversion and Management Journal*, pp. 658–663.

[48] Victoria, M., R. Herrero, C. Domìnguez, I. Antòn, S. Askins, and G. Sala (2011) "Characterization of the spatial distribution of irradiance and spectrum in concentrating photovoltaic systems and their effect on multi-junction solar cells," *Progress in Photovoltaics: Research and Applications*, pp. 308–318.

[49] Leuts, R., A. Suzuki, A. Akisawa, and T. Kashiwagi (2001) "Flux uniformity and spectral reproduction in solar concentrators using secondary optics," in *ISES Solar World Congress*, pp. 775–784.

[50] Almonacid, F., P. Perez-Higueras, E. F. Fernandez, and P. Rodrigo (2012) "Relation between the cell temperature of a HCPV module and atmospheric parameters," *Solar Energy Materials & Solar Cells*, pp. 322–327.

[51] Kumar, N. and et al. (2012) "Experimental validation of a heat transfer model for concentrating photovoltaic system," *Applied Thermal Engineering*, pp. 175–182.

[52] Damiano, A., I. Marongiu, C. Musio, and M. Musio (2013) "Outdoor Characterization of a Cassegrain-type Concentrator Photovoltaic Receiver," in *Conference of the Industrial Electronics Society (IECON)*, pp. 8110–8115.

[53] Pozzetti, L., M. Musio, D. Vincenzi, C. Musio, and S. Baricordi (2012) "A novel cassegrain-type concentrator photovoltaic module: design, ptototyping and characterization," in *27th European Photovoltaic Solar Energy Conference and Exibition (PVSEC)*, pp. 239–243.

[54] IEC "IEC 60904-9: Solar simulator performance requirements," .

[55] Nishi, D., T. Ueda, and Y. Hishikawa (2011) "Development of indoor characterization technologies for CPV devices at AIST," in *37rd IEEE Photovoltaic Specialists Conference*, pp. 530–533.

[56] Akkutrack, https://akkutrack.com.

[57] Baig, H., K. Heasman, and T. Mallik (2012) "Non-uniform illumination in concentrating solar cells," *Renewable and Sustainable Energy Reviews*, pp. 5890–5909.

[58] Gualdi, F., D. Vincenzi, S. Baricordi, M. Pasquini, F. Pozzetti, and V. Guidi (2011) "Finite element model for thermal analysis of a high-concentration modular CPV system," in *26th European Photovoltaic Solar Energy Conference and Exhibition (PVSEC)*, pp. 690–693.

[59] IEC "IEC 60891/2009: Photovoltaic devices – Procedures for temperature and irradiance corrections to measured I-V characteristics," .

[60] Musio, M., T. Pisanu, C. Musio, and A. Damiano (2012) "A concentrator photovoltaic panel prototype: realization and characterization," in *27th European Photovoltaic Solar Energy Conference and Exibition (PVSEC)*, pp. 218–223.

[61] ASTM "ASTM E 2527/2009 Standard Test Method for Electrical Performance of Concentrator Terrestrial Photovoltaic Modules and Systems under Natural Sunlight," .

[62] Platt, G., A. Berry, and D. Cornforth (2012) *What role for microgrids?*, Academic Press.

[63] Damiano, A., G. Gatto, A. Lai, I. Marongiu, C. Musio, A. Perfetto, and A. Serpi (2015) "A DC Side Energy Storage Management for One-Day-Ahead Power Profile Control of Concentrator Photovoltaic Power Plants," in *5th International Conference on Clean Electrical Power*.

[64] Borghetti, A., M. Bosetti, S. Grillo, S. Massucco, C. Nucci, M. Paolone, and F. Silvestro (2010) "Short-term Scheduling and Control of Active Distribution Systems with High Penetration of Renewable Resources," *Systems Journal*, pp. 313–322.

[65] Trovao, J., P. Pereirinha, and H. Jorge (2009) "Simulation model and road tests comparative results of a small urban electric vehicle," in *35th Annual Conference of the IEEE Industrial Electronics Society (IECON)*, pp. 836–841.

[66] Mebarki, B., B. Draoui, B. Allaou, L. Rahmani, and E. Benachour (2013) "Impact of the Air-Conditioning System on the Power Consumption of an Electric Vehicle Powered by Lithium-Ion Battery," *Modelling and Simulation in Engineering*, pp. 1–6.

[67] Sehab, M. and B. Barbedette (2011) "Electric vehicle drivetrain: sizing and validation using general and particular mission profiles," in *International Conference on Mechatronics (ICM)*, pp. 77–83.

[68] Hayes, K. D. J. G. (2014) "Simplified electric vehicle powertrain model for range and energy consumption based on epa coast-down parameters and test validation by argonne national lab data on the nissan leaf," in *Transportation Electrification Conference*, pp. 1–6.

[69] Musio, C. and A. Damiano (2015) "Analysis of the effects of gear transmission structure on the electric vehicle performances," in *International Conference on Electrical Systems for Aircraft, Railway, Ship Propulsion and Road Vehicles (ESARS)*, pp. 1–6.

[70] Damiano, A., C. Musio, and I. Marongiu (2015) "Experimental Validation of a Dynamic Energy Model of a Battery Electric Vehicle," in *International Conference on Renewable Energy Research and Applications (ICRERA)*, pp. 1–6.

[71] Eshani, M., Y. Gao, and A. Emadi (2010) *Modern electric, hybrid electric and fuel cell vehicles*, CRC Press.

[72] Parka, G., S. Leeb, S. Jinb, and S. Kwak (2014) "Integrated modeling and analysis of dynamics for electric vehicle powertrains," *Expert Systems with Applications*, p. 2595–2607.

[73] Walker, P., S. Rahman, B. Zou, and N. Zhang (2013) "Modelling, Simulations, and Optimisation of Electric Vehicles for Analysis of Transmission Ratio Selection," *Advances in Mechanical Engineering*.

[74] Rabiei, A., T. Thiringer, and J. Lindberg (2010) "Maximizing the energy efficiency of a PMSM for vehicular applications using an iron loss accounting optimization based on nonlinear programming," in *International Conference on Electrical Machines (ICEM)*, pp. 1001–1007.

[75] Lu, L., X. Han, J. Li, J. Hua, and M. Ouyang (2013) "A review on the key issues for lithium-ion battery management in electric vehicles," *Journal of power sources*, pp. 272–288.

[76] Kroeze, R. and P. Krein (2008) "Electrical battery model for use in dynamic electric vehicle simulations," in *Power Electronics Specialists Conference*, pp. 1336–1342.

[77] Einhorn, M., F. Conte, C. Kral, and J. Fleig (2012) "Comparison, Selection, and Parameterization of Electrical Battery Models for Automotive Applications," *IEEE Transactions on Power Electronics*, pp. 1429–1437.

[78] Chen, M. and G. Rincon-Mora (2006) "Accurate electrical battery model capable of predicting runtime and I-V performance," *IEEE Transactions on Energy Conversion*, pp. 504–511.

[79] Liaw, B., G. Nagasubramanian, R. Jungst, and D. Doughty (2004) "Modeling of lithium ion cells- A simple equivalent-circuit model approach," *Solid State Ionics*, pp. 835–839.

[80] Dees, D., V. Battaglia, and A. Belanger (2002) "Electrochemical modeling of lithium polymer batteries," *Journal of Power Sources*, pp. 310–320.

[81] Zhang, C., K. Li, S. Mcloone, and Z. Yang (2014) "Battery modelling methods for electric vehicles - A review," in *European Control Conference (ECC)*, pp. 2673–2678.

[82] Hu, Y., S. Yurkovich, Y. Guezennec, and B. Yurkovich (2009) "A technique for dynamic battery model identification in automotive applications using linear parameter varying structures," *Control Engineering Practice*, p. 1190–1201.

[83] Perez, H. E., J. B. Siegel, X. Lin, A. G. Stefanopoulou, Y. Ding, and M. P. Castanier (2012) "Parameterization and validation of an integrated electro-thermal cylindrical LFP battery model," in *Annual Dynamic Systems and Control Conference*, pp. 41–50.

[84] Mishra, P., S. Saha, and H. Ikkurti (2013) "Selection of propulsion motor and suitable gear ratio for driving electric vehicle on Indian city roads," in *International Conference on Energy Efficient Technologies for Sustainability (ICEETS)*, pp. 692–698.

[85] Tehrani, M., J. Kelkka, J. Sopanen, A. Mikkola, and K. Kerkkanen (2014) "Transmission configuration effect on total efficiency of Electric Vehicle powertrain," in *16th European Conference on Power Electronics and Applications (EPE'14-ECCE Europe)*, pp. 1–9.

[86] Hofman, T. and C. Dai (2010) "Energy efficiency analysis and comparison of transmission technologies for an electric vehicle," in *Vehicle Power and Propulsion Conference (VPPC)*, pp. 1–6.

[87] Ren, Q., D. Crolla, and A. Morris (2009) "Effect of transmission design on Electric Vehicle (EV) performance," in *Vehicle Power and Propulsion Conference (VPPC)*, pp. 1260–1265.

[88] Morozov, A., K. Humphries, T. Zou, S. Martins, and J. Angeles (2014) "Design and Optimization of a Drivetrain with Two-speed Transmission for Electric Delivery Step Van," in *IEEE International Electric Vehicle Conference (IEVC)*, pp. 1–8.

[89] Hanlon, M. (2009), "New multi-speed electric vehicle transmission improves EV performance and range," https://www.gizmag.

com/new-multi-speed-electric-vehicletransmission-improves-ev/-performance-and-range/11670.

[90] Sorniotti, A., T. Holdstock, G. Pilone, F. Viotto, S. Bertolotto, M. Everitt, R. Barnes, B. Stubbs, and M. Westby (2012) "Analysis and simulation of the gearshift methodology for a novel two-speed transmission system for electric powertrains with central motor," *Proceedings of the Institution of Mechanical Engineers*, pp. 915–929.

[91] Tsang, K., L. Sun, and W. Chan (2010) "Identification and modelling of lithium ion battery," *Energy Conversion and Management*, pp. 2857–2862.

[92] Li, F., R. Li, and F. Zhou (2016) *Microgrid technology and engineering application*, Elsevier.

[93] Damiano, A., G. Gatto, I. Marongiu, M. Porru, and A. Serpi (2014) "Real-time control strategy of energy storage systems for renewable energy sources exploitation," *Transactions on Sustainable Energy*, pp. 567–576.

[94] Damiano, A., C. Musio, C. Sanna, and M. Gawronska (2015) "A Microgrid Energy Management System Supported by a Hysteresis Vehicle to Grid Controller," in *International Conference on Renewable Energy Research and Applications (ICRERA)*, pp. 1–6.

[95] Damiano, A., G. Gatto, A. Lai, I. Marongiu, C. Musio, A. Perfetto, and A. Serpi (2015) "A DC Side Energy Storage Management for One-Day-Ahead Power Profile Control of Concentrator Photovoltaic Power Plants," in *International Conference on Clean Electrical Power (ICCEP)*, pp. 339–345.

[96] Whitefoot, J. (2012) "Optimal co-design of microgrids and electric vehicles: synergies, simplifications and the effects of uncertainty," .

[97] Peterson, S., J. Apta, and J. Whitacre (2010) "Lithium-ion battery cell degradation resulting from realistic vehicle and vehicle-to-grid utilization," *Journal of Power Sources*, pp. 2385–2392.

[98] Bishop, J., C. Axonb, D. Bonillac, M. Trana, D. Banisterc, and M. McCulloch (2013) "Evaluating the impact of V2G services on the degradation of batteries in PHEV and EV," *Applied Energy*, pp. 206–218.

[99] Guenthera, C., B. Schotta, W. Henningsb, P. Waldowskic, and M. Danzer (2013) "Model-based investigation of electric vehicle battery aging by means of vehicle-to-grid scenario simulations," *Journal of Power Sources*, pp. 604–610.

[100] Igualada, L., C. Corchero, M. Cruz-Zambrano, and F. Heredia (2014) "Optimal energy management for a residential microgrid including a vehicle-to-grid system," *Smart Grid*, pp. 2163–2172.

[101] Sanna, C., M. Gawronska, M. Musio, and A. Damiano (2014) "Performance analysis of non-linear load effects on a micro-grid supplied by photovoltaic power plants," in *European Photovoltaic Solar Energy Conference and Exhibition (PVSEC)*, pp. 3011–3015.

[102] Autorità per l'Energia Elettrica e il Gas (2012) "Revisione Del Servizio Di Dispacciamento Dell'energia Elettrica Per Le Unità Di Produzione Di Energia Elettrica Alimentate Da Fonti Rinnovabili Non Programmabili," .

[103] Gawronska, M., C. Sanna, M. Musio, and A. Damiano (2014) "Preliminary Evaluation of HCPV System In-field Energy Production in the Mediterranean Area," in *European Photovoltaic Solar Energy Conference and Exhibition (PVSEC)*, pp. 2128–2133.

Publications

1. A. Damiano, **C. Musio**, C. Sanna, M. Gawronska, *A microgrid energy management system supported by a hysteresis vehicle to grid controller*, International Conference on Renewable Energy Research and Applications (ICRERA), Palermo, 2015;

2. A. Damiano, **C. Musio**, I. Marongiu, *Experimental validation of a dynamic energy model of a battery electric vehicle*, International Conference on Renewable Energy Research and Applications (ICRERA), Palermo, 2015;

3. M. Musio, A. Serpi, **C. Musio**, A. Damiano, *Optimal management strategy of energy storage systems for RES-based microgrids*, Annual Conference of the IEEE Industrial Electronics Society (IECON), Yokohama, 2015;

4. A. Damiano, G. Gatto, A. Lai, I. Marongiu, **C. Musio**, A. Perfetto, A. Serpi, *A DC side energy storage management for one-day-ahead power profile control of concentrator photovoltaic power plants*, International Conference on Clean Electrical Power (ICCEP), Taormina, 2015;

5. **C. Musio**, A. Damiano, *Analysis of the effects of gear transmission structure on the electric vehicle performances*, International Conference on Electrical Systems for Aircraft, Railway, Ship Propulsion and Road Vehicles (ESARS), Aachen, 2015;

6. M. Musio, **C. Musio**, C. Sanna, M. Gawronska, A. Damiano, *Characterization of a CPV module prototype for design and performance improvement*, International Energy Conference (ENERGYCON), Dubrovnik, 2014;

7. A. Damiano, I. Marongiu, **C. Musio**, M. Musio, *Concentrator photovoltaic standards: experimental analyses of technical requirements*, Annual Conference of the IEEE Industrial Electronics Society (IECON), Wien, 2013;

8. A. Damiano, I. Marongiu, **C. Musio**, M. Musio, *Outdoor characterization of a cassegrain-type concentrator photovoltaic receiver*, Annual Conference of the IEEE Industrial Electronics Society (IECON), Wien, 2013;

9. C. Sanna, T. Pisanu, **C. Musio**, M. Musio, A. Damiano, *Cost effective HCPV fresnel lenses module prototype: design, performance, results, in-field testing and economic analysis*, M. Gawronska, European Photovoltaic Solar Energy Conference and Exhibition (PVSEC), Paris, 2013.

List of Figures

List of Tables